Cranfield University

Yves Soufflet

Improvement of runback water film calculation and its impact on ice prediction

School of Engineering

PhD Thesis

Cranfield University
School of Engineering
Applied Mathematics and Computing Group

PhD Thesis

Academic Year 2008 - 2009

Yves Soufflet

Improvement of runback water film calculation and its impact on ice prediction

Supervisor: Prof C.P. Thompson

December 2008

This thesis is submitted in partial fulfilment of the requirements for the Degree of Doctor of Philosophy

Abstract

Over the past few decades, aircraft icing has been the subject of numerous studies. Ice accretion on an aircraft can damage its aerodynamic performance. It can also have a devastating affect on structures such as high voltage pylons. The simulation of ice accretion represents an important technological breakthrough in the understanding of ice behaviour as well as an alternative to expensive experiments. Although numerical models will probably never replace wind tunnel experiments, they continuously progress and benefit from the latest advances in computing techniques. ICECREMO2 is a new generation model and uses an unstructured grid approach. Unstructured meshes offer real advantages in the generation of complex grid structures but also provide support for grid adaptivity. Adaptivity consists in improving the resolution only in some aspects of the solution. It offers the benefits of the high resolution without the computational overhead of classical structured methods. Adaptive methods are usually more difficult to implement and the application to the equation coupling water film and ice growth has never been investigated before this work.

The mathematical model used in ICECREMO describes both the water film flow and the ice growth. This allows us to better predict glaze ice accretion when a runback water film is present. The equation describing the thin film water flow is a complex non-linear fourth-order degenerate partial differential equation. To resolve complex features such as a moving front, high resolution numerical methods are necessary. Such a numerical scheme has been developed for this equation in a previous study on structured grid, and has proven to be reliable. In this work Sweby's scheme has been reformulated in a finite volume framework, an error estimator has been defined for our adaptive mesh refinement method and a grid refinement strategy has been implemented which follows the water film front and keeps it under high resolution.

Finally, the impact of the improved resolution of the water film on the glaze ice growth is investigated. Results obtained with first-order and high resolution methods have been compared on different model problems under various conditions. At the end an extension of the refinement strategy is proposed by defining error estimators with respect to the ice layer and by combining it with a multi-step procedure.

ACKNOWLEDGEMENTS

A lot of different people have been supporting me, one way or another, over the course of my studies in Cranfield and I hope I do not forget anyone here.
The first person I have to thank is my supervisor. Prof. Chris Thompson has been supporting me since my MSc in AMAC and has given me the opportunity to pursue a PhD. The long discussions have always been entertaining and his sens of humour a precious help in the difficult times. Chris has been very supportive during the long process of the writing-up and understood very well the 'personal difficulties' a student can face. Many thanks to him.
I probably would not have thought of coming to Cranfield University if it wasn't for Dr. Mohammed Louaked of the 'Université de Caen'. He introduced me to numerical analysis and used his connection with AMAC to introduce us to Prof. Chris Thompson. I use the word 'us' on purpose here as two of my friends, Pauline and Jérôme, also from Caen, joined me in the adventure. Their friendship has been valuable throughout the years. Unfortunately Jérôme passed away two years ago. His memory will stay with me. Patrick Verdin joined this close group of friends almost immediately and remains a friend since then. Many thanks to him for: working with me on an 'adaptive multi-stepping', spending time on proof-reading this thesis, introducing me to 'la Choulette' (better known as chibouliboulette) and many other things.
Aaron also has to be thanked for correcting part of this thesis and for keeping me fit physically and mentally with squash and chess games (and guitar sessions). For all the persons who worked with me in the e-science lab, particularly: Du, Bo, Hans, thank you! Thanks also to all the staff of the AMAC department specially Rachael. Dr. Jean Charpin and Dr. Ouahid Harrireche also provided valuable help at the beginning of this PhD. All the university staff have generally been very helpful, from Les Oswald in the computer centre to Kate Rolley of the housing office, their professionalism has made life easier and deserves to be recognised.
Andy Press and his group from BAe systems provided valuable help during the code development of this work. Many thanks to them.
My current colleagues have also been very supportive during my writing-up. I wish to thank : Chris Pain and the Applied Mathematics and Computing Group from the Imperial College for their patience and support as well as David Smeed and Adrian New from the National Oceanography Centre. A special thought to Prof. Peter Killworth who never doubted I would finish this PhD and who unfortunately won't be here to see this achievement.

More importantly I would like to thank my entire family without who I would not have achieved this work. Starting with my father who gave me 'le goût des maths' and nourished my interest in mathematics in general. He also supported me financially during my undergraduate studies. My mother, Coco, my brother and sisters always made sure that my trips in France were worthwhile sometimes trying to make me catch up in days with all the french gastronomy I was supposedly missing out in the UK. Patrice and Domy, my parents in law, and Micheline have to be thanked as well for all their help in removal, baby sittings and belote games.

Finally all my thoughts goes to Mylène, the love of my life, and our two loving children Julia and Thomas. They are the happiness of my life and I dedicate this thesis to them.

Yves Soufflet.

Contents

List of Figures

Nomenclature

b	Ice height		m
(g_x, g_y, g_z)	Gravity components	9.8	$\mathrm{m{\cdot}s^{-2}}$
h	Water height		m
t	Time		s
x, y, z	Cartesian coordinates		m
(A_x, A_y)	Shear stress components		$\mathrm{kg{\cdot}m^{-1}{\cdot}s^{-2}}$
G	Liquid water content	0.001	$\mathrm{kg{\cdot}m^{-3}}$
(Q_x, Q_y)	Water fluxes		$\mathrm{m^2{\cdot}s^{-1}}$
W	Free stream velocity		$\mathrm{m{\cdot}s^{-1}}$
β	Collection efficiency	$0-1$	
μ	Dynamic viscosity	0.001	$\mathrm{kg{\cdot}m^{-1}{\cdot}s^{-1}}$
ρ_i	Ice density (glaze)	898	$\mathrm{kg{\cdot}m^{-3}}$
ρ_w	Water density	1000	$\mathrm{kg{\cdot}m^{-3}}$
p	Water pressure		
T_f	Freezing temperature		
T_i	Temperature at the bottom of the airframe surface.		
ρ_A	Droplet content of the air.		
θ	Temperature in the water layer		
q_i	Flux through edge		
n_i	Vector normal to edge		
E_i	Length of edge		
S	Stephan number		
c_{1g}, c_{2g}	constants for the glaze ice accretion term		

Chapter 1

Introduction

The unique goal of this chapter is to set the scene of this thesis. First we show the interest in the current research by giving a brief overview of the problems caused by ice accretion in the last twenty years. Then the different devices created to overcome these problems will be presented. Icing occurs only in certain conditions and depending on these conditions different kinds of ice may appear. This implies different mathematical models. In Chapter 2 we will present a literature review on the mathematical aspect of this thesis. The main work of this thesis is then presented in Chapters 3, 4 and 5.

1.1 Damage of Ice Accretion

Icing is one of the most serious hazards for aircrafts. In 1995 the AOPA [8] recorded 285 accidents in 9 years (according to the Air Safety Foundation database) in which icing was supposed to be a factor. These included almost 300 fatalities. Over a more recent period, from 1990 to 2000, 388 accidents due to icing have been registered [9]; this is 12% of all accidents. Despite the increase in research in this field and the efforts to make pilots aware of the danger of airframe ice accretion, there are still a lot of accidents including fatalities due to icing. This suggests that either the amplitude of the danger is not fully taken into account or that our understanding of the icing process is still not good enough

to prevent accidents.

Ice accretion is not only a problem for aircraft industry. In 1998, a catastrophic ice storm hit the Canada and the northeast part of the United States. In Quebec about 900,000 households stayed without power, 100,000 in Ontario. After three weeks more than 700,000 were still without electricity in Canada. During this storm the freezing precipitation was twice bigger than the annual average [5]. The main impact of these storms (or at least the most notified) is on power industry [14]. In 1998, hundreds of kilometers of power lines were down. High voltage towers in south Montreal collapsed under the weight of accumulated ice. This illustrates the terrible power of the ice on solid structure.

On an airplane, ice may appear both in flight and on the ground under appropriate weather conditions. However the problem is much more important and dangerous during flight, since ground crews can de-ice before take-off. A review over the airframe icing accident in the U.S. from 1982 to 2000 [10] shows that the majority of accident is from the"general aviation" flights, which consist of small aircrafts usually personal or of recreational nature. Almost half of the fatal accidents happened during cruise phase. However, for most large jet aircraft, icing does not occur during cruise flight since the airplane is above the cloud layer. Accidents during the take-off and the approach phase represent 25% of the fatal accidents. These are both times when greater lift and control are required [18] [17]. Ice can distort the flow of air over the wing, diminishing the wing's maximum lift, reducing the angle of attack for maximum lift, adding weight and increasing drag [16] adversely affecting airplane handling qualities which can jeopardize flight safety. More details on the icing effects on aircraft stability can be found in [17]. One example is given in [1]: a 0.4mm ice layer can reduce the lift up to 25% and reduce the stall angle of attacks by 6 degrees. It can also destroy instruments on the surface of the plane or damage the engine in the case of ice shedding.

In an icing scenario, a pilot must react quickly and adequately to the type of icing encountered. The strategy to escape depends for example where the ice is present on the airframe. If an ICTS (Ice Contaminating Tailplane Stall) is encountered, the pilot must reduce the speed to re-establish the balance of the plane. If ice appears on the wing, the speed has to be increased to avoid the stall. Although wing stall is a much more common threat, for pilots the ICTS represents a greater danger as they cannot see the tail of the plane thus appreciate the extent of the problem. Inexperienced pilot realize sometimes too late that their facing an ICTS. It is although very important to distinguish between the two since"the required actions are roughly opposite" [9].

The best strategy being to avoid icing front, progress in weather forecast has played a major role in the prevention of accidents due to ice accretion. Knowing where the front is, where it is moving, where the top and base of the clouds are, provide valuable information to plan alternate routes.

Although in this study we are only interested by structural icing, ice accretion on the surface of the plane, induction icing is responsible for half of the accidents under icing conditions. Induction system icing includes carburetor icing and air intake blockage. When ice builds up in the carburetor compartment, it reduces the supply of air to the engine, which can result in a power loss and ultimately to the engine failure. Relative humidity is responsible for this and carburetor icing can happen outside atmospheric icing conditions. However when conditions are favorable to airframe icing, engines can fail if the air intakes are blocked by ice. All small engines should have alternate doors which can be open to allow air to flow through them.

Finally, an aircraft passes through rigorous safety tests to obtain an icing approval. Beyond many things, the approval is concerned for example by the windshield: for the pilot vision and by the control surfaces which must be spaced enough to allow their movement even under severe icing conditions and finally by the installation of ice protection systems.

1.2 Current Ice Protection

Several ice protection techniques are used to improve flight safety and can be classified as anti or de-icing methods:

- Anti-icing systems consist in protecting the surfaces from ice formation by keeping the surface at a temperature higher than the freezing temperature.
- De-icing systems are periodically removing the accreted ice. Ice is removed before the ice layer affects the aircraft performances.

Mechanical devices are used as de-icing systems, and utilize surface deformation techniques. Pneumatic boot systems have first been widely used. The boot surface removes ice accumulation mechanically by alternatively inflating and deflating tubes within a boot that covers the surface [23]. The ice bond is broken off and the ice is removed by aerodynamics forces. A pneumatic impulse device sends an air shock wave that break and remove the ice from the wing. The shock is generated by a pulse of high pressured air into a flexible pipe located underneath the surface. The Electromagnetic Impulse De-Icing system (EIDI) locally deforms the metallic surface with electromagnetic impulses [23] [21]. The impulse is repeated within few milli-seconds and successively breaks the ice bond.

Chemical devices act as anti-freeze reducing the freezing point of water. It consists in applying an anti-freeze such as ethylene glycol to the lifting and control surfaces during flight. The chemicals work by dissolving slowly on contact to create a brine, with the heat of solvation for some chemicals helping to melt the ice or snow [19]. Also called 'weeping wing' device [9], the de-icing system pumps fluid from a reservoir through a mesh screen embedded in the leading edge of the wings and tail. It works also as an anti-icing: mixed with water the freezing temperature of the fluid is below the ambient air temperature, and so no ice will form. An important drawback is the toxicity of these products and

the concern for the safety of the ground crews. The ethylene glycol highly toxic is being replaced by the propylene glycol 'essentially nontoxic' [19].

Thermal devices provide protection by melting the ice or keeping the surface temperature above the ice formation temperature. Electrical pad as well as bleed air are used to warm the surface of a wing . The thermal energy destroys the adhesion force in the ice surface interface and the aerodynamics forces remove it. Both systems require enormous power consumption and 'hot wings' systems are only found on jets. Ice protection systems however can fail or be inefficient depending on the type of ice that may form. This will now be discussed.

1.3 Different types of ice

In flight icing occurs mainly when aircrafts fly through clouds made of supercooled droplets. Supercooled droplet are water droplets whose temperature can be far below freezing and still be in a liquid state. The growth rate of ice will be directly linked with the size of these droplets and the liquid water content (LWC) of the cloud, i.e.: the mass of water in a given volume. All clouds are not alike, icing can happen in stratus or cumulus. They are also referred as dry and wet clouds respectively in the pilot jargon. Dry cloud have by definition a low LWC and have relatively little moisture whereas wet clouds have a larger LWC and can potentially lead to severe icing conditions. Depending on the atmospheric conditions different type of ice may appear.

- If the supercooled droplets freeze entirely when they hit the surface, rime ice forms. Rime ice occurs in clouds of low liquid water content and has an opaque and milky color white color due to the presence of air bubbles trapped during the rapid freezing process. Because of these bubbles, rime ice is less dense. The corresponding

density depends greatly of the size of the trapped air pockets [1]. In aircraft icing simulation, a typical value for the density is $880kg.m^{-3}$. Rime is usually generated in air temperatures $-15°C$ and below. The resulting shape is generally rounded with relatively large surface roughness.

- When the droplets remain partially liquid glaze or clear ice forms. It develops in milder conditions at temperature closer to freezing and this type of ice usually is associated with larger droplet. The droplets freeze slowly and partially leading to a clear and transparent material usually with a smooth surface but a very irregular surface profile. The part of the droplets that remains liquid is known as runback water. The density of glaze is close to the standard value $917kg.m^{-3}$. The resulting shape is more complex and typically characterized by the presence of horns [20, 1]. It disrupts more the airflow around the airfoil, and glaze ice may be harder to break than rime ice.

Rime and glaze are the most common type of ice. They can also appear at the same time to form mixed ice, or glaze can form on top of rime ice. The importance of making the difference between the different types of ice is for the pilot to be able to assess the potential risk as glaze ice is considered more hazardous; and for the modelers to develop adequate physical models to describe ice growth. In the case of glaze ice for example, the water flowing on the wing surface has to be taken into account. In this thesis we concentrate on the solution of the thin film flow and show how it affects the final ice shape, so only glaze ice is considered in this work.

1.4 The modelisation

A number of codes have been developed to simulate ice accretion. To cite but a few, LEWICE from the NASA Glenn Research Centre [6], TRAJICE from DERA (now Qine-

tiQ) in UK and the French code from ONERA [24] have probably been the most widely used. They also have been part of a collaborative study between the different agency in order to compare and test the features of each code [27]. The Canadian code CANICE has also led to a significant number of publications [43, 42]. All these codes evolve around the Messinger model which consist in solving an energy balance at each control volume between the different heat fluxes. These fluxes include source or loss of energy like evaporation, convection, kinetic energy, latent and radiative heat. The difference between the models in the standard Messinger-based codes is in the terms considered in the energy balance, see [20] for details.

One of the limitations of the Messinger-based model is in the simulation of the runback water. The dynamic of the water film is not taken into account and as such the conduction in the water layer is not considered. The presence of this water film at mild condition is very important for glaze ice formation. The behaviour of the film will affect the final ice shape. Rothmayer's team from the IOWA State University studied the interaction between water and ice dynamics (see [22, 32, 33] for example). In [32], Matheis shows that surface waves can increase the mass flux by 50% thus affect the resulting ice shape. The droplet impacts can also generate waves and instabilities of the water film [33] influencing its breaking into rivulets.

In the author's knowledge, FENSAP-ICE [25, 26, 7] and ICECREMO are the only ice accretion code which solve an equation for the water film. The Applied Mathematic And Computing (AMAC) department of Cranfield University has been involved with ICECREMO since the beginning of the project. Myers [4] first developed the physical model which was later improved [1, 2]. This model is presented in the following section.

1.4.1 The physical model

The mathematical model used in ICECREMO [15] has originally been developed by Myers [4]. The same set of equations is derived for a general surface in [1, 2, 3]. The problem consists in a fluid flow model for the water layer and a thermal problem to determine the freezing rate $\frac{\partial b}{\partial t}$, where, as described in Figure 1.1, b represents the ice height and h the water height.

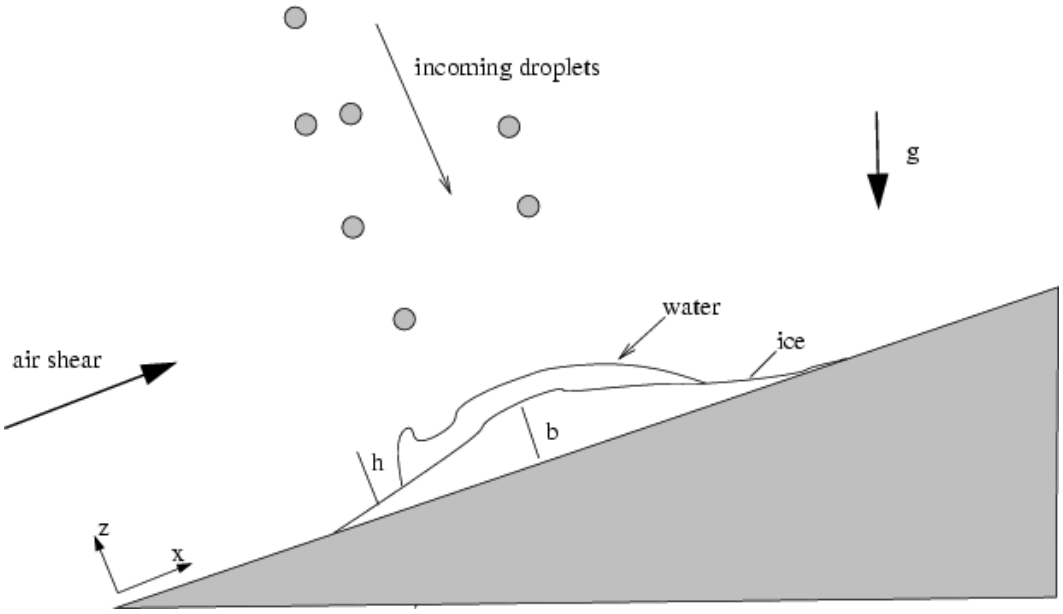

Figure 1.1: Problem configuration

For the fluid flow model, the Navier-Stokes equations are combined with a continuity equation to solve for the velocities and the pressure in the fluid. Two assumptions are then required [2]:

- The effect of temperature on the viscosity μ, and density ρ_w of the fluid is relatively small until the sudden change as solidification occurs, therefore, for the flow calculation μ and ρ_w are taken as constant.

- The aspect ratio of the flow ϵ (depth scale / length scale), and reduced Reynolds

number, $\epsilon^2 Re$, are both sufficiently small that lubrication theory may be applied.

Details of the derivation of the governing equation can be found in [1, 2, 3, 4], basically, by applying the boundary conditions at the interface between ice, substrate and water film and integrating the continuity equation across the film, we obtain the final form governing equation:

$$\frac{\partial h}{\partial t} + \nabla . Q = \frac{\beta W G}{\rho_w} - \frac{\rho_i}{\rho_w}\frac{\partial b}{\partial t} \tag{1.1}$$

where the fluid flux is:

$$Q = \left(-\frac{h^3}{3\mu}\left(\frac{\partial p}{\partial x} + G_1\right) + \frac{A_1 h^2}{2\mu}, -\frac{h^3}{3\mu}\left(\frac{\partial p}{\partial y} + G_2\right) + \frac{A_2 h^2}{2\mu}\right) \tag{1.2}$$

with $(G_1, G_2, G_3) = \rho_w g(\overrightarrow{g}.\overrightarrow{x}, \overrightarrow{g}.\overrightarrow{y}, \overrightarrow{g}.\overrightarrow{z})$.

The thermal problem to determine the freezing rate considers rime and glaze ice. For rime ice, there is no liquid water present, the problem is reduced to:

$$b = \frac{\rho_A}{\rho_i}\beta W t \tag{1.3}$$

The transient ice growth is directly proportional to the free-stream velocity (speed of the droplets) and the catch or collection efficiency.

The temperature profile satisfying:

$$T = T_s + \frac{q_{0r} + q_{1r} T_s}{1 - q_{1r} b} z \tag{1.4}$$

For glaze ice, the temperature profiles are in the ice layer:

$$T = T_s + (T_f - T_s)\frac{z}{b} \tag{1.5}$$

and,

$$\theta = T_f + \frac{q_0 + q_1 T_f}{1 - q_1 h}(z - h) \tag{1.6}$$

in the water layer.

The ice thickness is derived from the energy balance at the freezing interface and can be written in its final form:

$$S\frac{\partial b}{\partial t} = \frac{1}{b} + \frac{c_{2g}}{1 + c_{1g}h} \tag{1.7}$$

S is the Stephan number and the c_{1g} and c_{2g} terms describe different terms in the energy balance such as evaporation aerodynamic heating, droplet kinetic energy, convection, etc (see details in [1, 4]).

As already mentioned, this model is the base of the ICECREMO code. The new version of the code called ICECREMO2 has been used to generate the results presented in this thesis. This code will now be described briefly.

1.4.2 ICECREMO2 code structure

Due to the complexity of the phenomena to describe , icing codes are divided into several modules. ICECREMO2 consists in three modules:**CORNETTO**,**RIPPLE** and **MAGNUM**. The **CORNETTO** module extracts a surface mesh and data for the water film and ice accretion module from a flowfield data which can come from a variety of CFD

sources, and perform a droplet trajectory calculation. The collection efficiency results from this module and determines the incoming water mass entering the domain.

The **RIPPLE** module ensures that shear stress and convective heat transfer coefficients are available to enable a water film and ice growth calculation to be performed by the **MAGNUM** module. It is inside this **MAGNUM** module that the work of this thesis is implemented.

One fundamental novelty in ICECREMO2 is the use of unstructured mesh. The icing surface is discretized with faces which can potentially be of any polyhedral shape [31]. The surface discretization will be defined in terms of an edge-based system used within the BAE SYSTEMS SOLAR. Re-arranging Equation (1.1) gives:

$$\frac{\partial h}{\partial t} = -\nabla.Q + \frac{\beta W G}{\rho_w} - \frac{\rho_i}{\rho_w}\frac{\partial b}{\partial t} \tag{1.8}$$

To determine the water transport over a cell, we loop over its edges, compute the contribution of the neighbouring cell via the numerical scheme. Below is an estimate of $\nabla.Q$ using this edge based formulation:

$$\nabla.Q \approx \frac{1}{A}\sum_{i=1}^{N} \overrightarrow{q_i}.\overrightarrow{n_i}.E_i \tag{1.9}$$

where A is the area of the face. E_i, $\overrightarrow{n_i}$ and $\overrightarrow{q_i}$ denote the length, the normal and the flux through the edge i, respectively.

This is calculated in the function *CalcRHS()* using the appropriate numerical scheme. The freezing ratio is also calculated face by face using Equation (1.7). The local water height can then be updated (in the function *Update()*) by the addition of the right hand side of Equation (1.8) multiplied by the time step. This is carried on until the appropriate time period has elapsed. A diagram of the entire process can be seen in Appendix A.

1.5 Contributions and structure of this thesis

Recent progress in technology will certainly improve a lot the aircraft safety as well as our understanding of the icing process. Features such as mini sensors situated on the wings of an aircraft can provide live and 'exact' informations to a pilot about the growing rate and the amount of ice on his plane. Such advancement in remote sensing and computational power make that live icing simulation is not a science fiction scenario any more. Computational models combined with data assimilation techniques could provide useful tools for pilots who encounter icing conditions and are in need to find an escape route for example. At the moment models have been validated for a large range of applications and are part of the design and qualification processes. However the use of three dimensional icing codes is relatively recent and with the additional resources required for such calculations come new computational techniques using unstructured approach. Unstructured grids permit the description and discretization of complex surface as well as the use of adaptivity. Adaptivity consists in increasing the resolution of the grid (i.e.: the number of points or elements) in certain regions where more accuracy is needed whilst the other parts of the grid remain at coarse resolution. This technique allow one to accurately model complex flow without increasing too much the computational power. In this thesis we assess the effect of the accuracy of the water film solution on the final ice shape under glaze ice conditions. However the development of such complex methods requires to divide the study in several steps, these are reflected in the structure of this thesis.

Chapter 2 is devoted to the literature review. This is done in twofold. First the thin film flow dynamic is very complex and contains many features which are relevant for different applications. A selection of study is presented with relevant interest for ice modelling. The partial differential equation governing the spreading of a liquid in thin layer is very

difficult to solve. In the second part of this chapter, we review the different numerical methods available and focus on the special category of the high resolution methods. The numerical scheme used throughout this work belongs to this category of shock capturing scheme.

In **Chapter 3**, Equation (1.1) is studied and the numerical scheme to solve it is presented. Emphasis is put on the definition of the flux limiter and the finite volume formulation of Sweby's scheme. Two dimensional test cases are presented highlighting the effects of the different forces involved and the corresponding flux terms. Results are in good agreement with previous studies. More complex scenario are then considered in three dimensions including a rotating case.

Chapter 4 is the error control methodology. A qualitative study is performed showing the necessity of higher resolution at the front of the water flow. Then an error estimator is derived using double discretization. The dual property of the numerical scheme is directly used so no additional calculation is required for the computation of this error indicator. The refinement technique is explained. The interpolation from grid to grid after refinement or de-refinement are mass conservative. Criteria such as the number of edges to be refined are chosen so that the all process can be fully automatic. The result is an adaptive technique capable of automatically refining and de-refining the mesh so that the water front is constantly under fine resolution. The gain in performance is also assessed.

Finally in **Chapter 5**, the adaptive numerical method developed in the previous chapters is employed in the context of icing. First an anti-icing calculation is performed to establish the importance of the front flow in such scenario. Then glaze ice simulations are executed. The front flow is shown to affect sensibly the amount of ice but only for a short

period. Due to the disparity of the time scale between water flow and ice accretion another criteria for refinement is derived taking into account the ice. The adaptive method is then combined with a multi-stepping approach.

Conclusions are drawn in the last chapter with some proposals for further studies and improvements.

Chapter 2

Literature Review

2.1 Introduction

The equation governing the ice accretion and water flow derived for the ICECREMO model has been presented in the introduction. In absence of ice accretion, Equation 1.1 is a typical thin film flow equation governing the spreading of a liquid in thin layer over a surface. This equation is notoriously difficult to solve and presents many challenges. First in terms of the complexity of the dynamics involved in these physical phenomena but also in term of the numerical methods one has to employ to resolve it accurately. In this chapter we review the different domains of application and pinpoint the studies relevant to this work. In the second part of this chapter we go over some of the finite difference and finite volume techniques developed for conservation law equations. We present the mathematical problems arising with such equation and survey the high resolution methods. The numerical scheme retained for the rest of this work belongs to this category and is presented at the end of this chapter.

2.2 Thin film flows

Thin film flows appear in a multitude of applications other than aircraft or atmospheric icing. In [65] Myers reviews those where surface tension is a dominant force. The most common application is certainly the coating of a surface with a thin liquid. This problem arises in industrial manufacturing such as microchip production where ultra thin layer of precious metal have to be applied; or more naturally when rain is running down a window. Other applications involve film condensation for cooling devices, paint drying where an evenly covered surface is required or the motion of a contact lens over the eyeball. Such films show complex dynamics such as wave propagation or wave steepening, they can rupture into fingers, creating holes or dry region. If in certain cases a solution can be found analytically [66], in general such complex equations are solved numerically.
Thin film flows are usually approached within the lubrication theory which reduces Navier-Stokes equations to a single fourth-order non-linear partial differential equation describing the evolution of the free surface $h(t, x, y)$ (the height of the liquid over the domain). An extensive review [74] uses an asymptotic theory, the long wave theory for the evolution of liquid film. In this review a lot of configurations are considered combining shear stress, surface tension, gravity, evaporation, van der Waals forces, Marangoni effect. Films on cylinder and on a rotating disc are also mentioned. A third review by Eggers [70] considers the nonlinear dynamics and breaking of free surface flow into droplets but also study the droplet-droplet interaction and the breaking of jets.

Coating film studies are deeply relevant to icing when the runback water film is considered. The coating process develops mainly as a balance of viscous and surface tension forces. Centrifugal or thermocapillary forces may also drive the flow. Although a lot of research and progress has been made in this area, the dynamics are still not fully under-

stood especially near the front. The main difficulty in solving such flow comes from the presence of the contact line, the boundary between the film and the uncoated/dry surface [73, 68].When the contact line is moving a singularity appears leading to an infinite stress at the front. This has been named commonly 'the contact line paradox' [83]. Two alternatives are possible and are discussed in [1] and [65] for example. One can relax the no-slip boundary condition at the solid liquid interface [71]. A common boundary condition is:

$$u|_{z=0} = \alpha \frac{\partial u}{\partial z} \tag{2.1}$$

This will add a term of order $O(h^2)$ proportional to α in the surface tension term of equation (1.1). β is chosen to be small enough to only affect the flow when the film thickness is significantly small.

The second solution is to use a precursor model [73] and [81, 83, 85]. This model assumes that the surface is pre-wetted by an ultra thin layer of liquid. This approach is equivalent to the slip models but have proven to be more efficient computationally [85, 82]. The ICECREMO model use a precursor film [3, 1, 2], and naturally this approach has been kept in the present work. We discuss the numerical effect of the precursor film in Chapter4.

One major challenge with coating films is to adequately represent their ability to break, disrupt into rivulets leaving some dry area. These instabilities have been subject to many studies, [77] is a main reference on this topic. Linear [71] and nonlinear [72] stability analysis have been performed on this type of equation. Numerical results are available for a multitude of different applications. In [76] the formation of rivulets for a thin film under centrifugal force is studied to simulate spin coating process. Instabilities induced by surfactant are explored in [75]. Evaporation effect is taken into account in [86]. Flow spreading down an inclined heated plate are considered in [87] and [79] where

the Marangoni effect has an important role.

The behaviour of the liquid near the front is related to the contact angle, the angle that the liquid form with the substrate. Numerically this angle is usually considered through 'Tanner's law' [65, 1]:

$$tan\theta \sim U^{\frac{1}{3}}$$

where θ is the contact angle and U the fluid velocity.

Experimental studies of the effect of the contact angle on the film rupture and the growing of instabilities have been performed in [69] and [67]. The main results of the studies is that at high contact angle, rivulets can form and leave some dry region. The contact angle also affects the shape and width of the rivulets.

The effect of body forces such as gravity can also produce different pattern at the contact line. With a flow spreading down a slope in [81], it is shown that with a high angle of inclination of a plate, so more important gravity effects, fingers or rivulets appear against sawtooth at lower angle.

Finally as a thin film spreads on a surface, the surface tension dominating at the front, a Lax-shock [1] will form (see also next Chapter). Under different conditions, different shocks can appear leading to different shape of the front. The different shock structures are studied in [78] in the case of rimming flow (rotating). For an inclined plate, Bertozzi et al. [84] look at undercompressive shocks arising when gravity and surface tension forces compete. The notion of shocks is re-assessed in the next section and a study of the evolution of the front shape with the angle of inclination is performed in the next chapter.

2.3 Numerical solution of conservation laws

The purpose of this section is not to present an exhaustive review of the numerical method developed for conservation laws but rather to pinpoint the theoretical difficulties encountered during this research together with the adequate literature. Most of the references presented in this section are well-known articles or books in the finite difference community and are, in the author's point of view, necessary for a good understanding of the numerical method employed in this thesis.

The equation governing the water film and ice accretion employed in this model is a scalar conservation law. At high temperature, when only the water film is considered, the equation describes the spreading of a thin liquid film over a dry surface. This phenomenon is particularly complex to model and both mathematical and numerical difficulties arise when trying to solve this type of equation. Although the different terms present in the flux make that the equation cannot be classified in a particular type, in most of the aeronautical cases presented in this thesis, the shear stress (wind force) plays a much greater role than the other forces. That said, if the pressure and surface tension terms are neglected, the equation is of Burger's type and is strictly hyperbolic. The solution of this type can present some singularities and be discontinuous. It then clearly does not satisfy the partial differential equation in the classical sense, at each point, since the derivatives are not defined at discontinuities. The 'weak' formulation is introduced, involving the integral form of the equation. Discontinuity is allowed, and function continuous almost everywhere are considered.

The second mathematical difficulty is the uniqueness of the solution. Conservation law with same initial data can have more than one weak solution. Of course only one is physically relevant. For this reason, a condition can be imposed directly on the weak solution.

This condition is called entropy condition by analogy with gas dynamics [48].

The numerical difficulties faced when trying to solve the partial differential equation numerically come again from the presence of discontinuities where the equation does not hold. Standard numerical methods are based on the assumption of smooth solutions and give very poor results near discontinuities. First-order accurate methods generate results that are very smeared in region near discontinuities. Leveque explains it by the large amount of numerical viscosity that these methods have which smoothes the solution. When trying to use a classical second-order accurate method, the numerical viscosity is eliminated but some dispersive effects are introduced and lead to numerical oscillations which can in turn lead to instability. To prevent this from happening a number of numerical methods called high resolution methods have been developed.

2.3.1 Shocks

Shock waves are discontinuous solutions of hyperbolic conservation laws. The term shock is generic and is employed in the literature independently of the field or application. It can describe a shock (or bore), a contact discontinuity, a shear wave or, in our case, a wet/dry or sharp front. From a numerical point of view the requirements of these flow features are identical and a good method for computing shocks will, in principle, deal successfully with other discontinuous waves.

Toro [35] distinguishes two approaches for computing solutions with discontinuities: the shock-fitting and the shock capturing methods. In the first one, discontinuities are tracked explicitly (the method is also called front tracking see [90] and [91]) and treated as internal boundaries across which the appropriate jump condition is applied.

For its simplicity and because it is applicable to a much wider set of problems, the shock capturing method is most commonly used. In this approach a single numerical scheme is employed on the entire domain. The discontinuity is part of the solution but spreads over

a number of mesh points. The term shock capturing is also become generic and refers to numerical methods which deal with the flow features automatically. The high resolution methods have this particularity, they will be detailed in the following section.

2.3.2 High resolution methods

Two classes of shock capturing scheme exist, the ENO (Essentially Non oscillatory) family and the TVD (Total Variation Diminishing) schemes. The main distinction being that ENO can retain the same order of accuracy in space near extremum whereas TVD reduces to first order. The scheme selected and used for this study has been constructed to be TVD, therefore only this class of schemes will be discussed in the following.
Before we go further in detail it is important to note that the TVD property is only valid for homogeneous scalar hyperbolic laws. We will see later how to deal with the source term in order to treat the nonhomogeneous equation.
The name high resolution methods has been given after the work of Harten [55] to qualify the schemes which satisfy the following three properties [36]:

- The schemes are second-order accurate or more in smooth part of the solution.
- The numerical solution is free from spurious oscillations
- The schemes produce high resolution of discontinuities, meaning that the number of mesh points in the zone containing the wave is narrow compared with that of first-order monotone methods.

In his most complete review, Yee [88] distinguishes four techniques to construct High resolution TVD schemes. They are:

- Hybrid schemes such as the Flux Corrected Transport of Boris and Book [58], Harten [52] and Van Leer [56];

- Second-order extension of Godunov's type schemes by Van Leer [57] or Colella and Woodward with their Piecewise Parabolic Method (PPM)[59];
- The modified flux approach of Harten [51];
- And the numerical fluctuation approach of Roe [61] and Sweby [37].

Apart from the second approach, the extension of Godunov's schemes to higher order, all techniques utilize one basic idea: the combination of a higher order and a first-order scheme using limiters to satisfy the TVD sufficient condition. These limiters or flux limiters impose some constraints on the gradient of the dependent variable and/or the flux function.

Flux Limited Methods

Intuitively flux limited methods are linear combinations of two first-generation methods. Practically, for scalar conservation laws, they are defined as follow:

$$u_i^{n+1} = u_i^n - \lambda(\hat{f}_{i+1/2}^n - \hat{f}_{i-1/2}^n) \tag{2.2}$$

Where:

$$\hat{f}_{i+1/2}^n = \hat{f}_{i+1/2}^1 + \phi_{i+1/2}^n(\hat{f}_{i+1/2}^2 - \hat{f}_{i+1/2}^1) \tag{2.3}$$

The flux limiter is the parameter $\phi_{i+1/2}^n$ controlling the linear combination where $\hat{f}_{i+1/2}^1$ and $\hat{f}_{i+1/2}^2$ are the conservative numerical flux of two different numerical schemes with complementary properties. A possible and usual approach is to choose one method suitable for smooth regions and a second near shocks. The flux limiter is then applied as a 'switch' between the two methods, raising the question of how to distinguish shocks from smooth

regions.

For this purpose a ratio r of solution difference is defined:

$$r = \frac{u_i^n - u_{i-1}^n}{u_{i+1}^n - u_i^n} \tag{2.4}$$

Often in the literature, see for example [13] for a detailed description, a specific notation is adopted for $r^+ = r$ and $r^- = \frac{1}{r}$.

Large increases (or decreases) in the solution difference are indicated by large or small ratios. However this method is not completely reliable to indicate shocks. Shocks will be reflected by very large or very small value of r but the inverse is not always true. In [13] (Chapter 20), Laney takes as example the case where $u_{i+1}^n - u_i^n = 0$ with $u_i^n - u_{i-1}^n \neq 0$ which gives an infinite value of r whether a shock is present or not. Consequently Laney states that flux limited methods 'do not even attempt to identify shocks but rather try to regulate minima and maxima' using non-linear stability conditions by restricting $\phi(r)$.

Another alternative is to use flux differences:

$$r = \frac{\hat{f}_{i-1/2}^2 - \hat{f}_{i-1/2}^1}{\hat{f}_{i+1/2}^2 - \hat{f}_{i+1/2}^1} \tag{2.5}$$

The same problems occurs as with the ratios of solution differences, large/small ratios are 'often, but not always', caused by shocks. By reformulating the numerical fluxes in term of artificial viscosity, we can see the relation between flux differences and solution differences ratios:

$$\hat{f}_{i+1/2}^1 = \frac{1}{2}(f(u_{i+1}^n) + f(u_i^n)) - \frac{1}{2}\epsilon_{i+1/2}^1(u_{i+1}^n - u_i^n) \tag{2.6}$$

And

$$\hat{f}^2_{i+1/2} = \frac{1}{2}(f(u^n_{i+1}) + f(u^n_i)) - \frac{1}{2}\epsilon^2_{i+1/2}(u^n_{i+1} - u^n_i) \tag{2.7}$$

The ratios of flux differences can be re-written as:

$$r = \frac{(\epsilon^2_{i-1/2} - \epsilon^1_{i-1/2})(u^n_i - u^n_{i-1})}{(\epsilon^2_{i+1/2} - \epsilon^1_{i+1/2})(u^n_{i+1} - u^n_i)} \tag{2.8}$$

It is this method which will be used in the next chapter to define the ratio for the flux limiter employed in this thesis.

The **Van Leer's flux-limited method** combines a Lax-Wendroff scheme with a Beam-Warming scheme:

$$\hat{f}^n_{i+1/2} = \frac{1}{2}(\hat{f}^{LW}_{i+1/2} + \hat{f}^{BW}_{i+1/2}) + \phi^n_{i+1/2}(\hat{f}^{LW}_{i+1/2} - \hat{f}^{BW}_{i+1/2}) \tag{2.9}$$

With

$$\phi^n(r) = \frac{|r| - 1}{|r| + 1} \tag{2.10}$$

Van Leer proposed this approach for the linear advection equation in 1974 in the second of a five papers series entitled 'Towards the ultimate conservative difference scheme' [56]. The **Sweby's flux-limited method** combines a Lax-Wendroff second-order scheme with a first-order upwind. In Equation 2.2, in the non-linear case considering $a(u) > 0$, $\hat{f}^n_{i+1/2}$ would take the form:

$$\hat{f}^n_{i+1/2} = (1 - \phi^n(r_{i+1/2}))\hat{f}^{UP}_{i+1/2} + \phi^n(r_{i+1/2})\hat{f}^{LW}_{i+1/2} \tag{2.11}$$

With:

$$a_{i+1/2} = \begin{cases} (f_{i+1}^k - f_i^k)/(u_{i+1}^k - u_i^k) & \text{if } u_{i+1}^k - u_i^k \neq 0 \ , \\ \partial f^k/\partial u\big|_{i+1/2} & \text{if } u_{i+1}^k - u_i^k = 0 \ , \end{cases}$$

The ratio r is written:

$$(r_i^+) = \frac{\left(a_{i-\frac{1}{2}} - \lambda a_{i-\frac{1}{2}}^2\right)(u_{i+1} - u_i)}{(a_{i+\frac{1}{2}} - \lambda a_{i+\frac{1}{2}}^2)(u_{i+1} - u_i)} \tag{2.12}$$

Or equivalently:

$$(r_i^+) = \frac{\hat{f}_{i+1/2}^{LW} - \hat{f}_{i+1/2}^{UP}}{\hat{f}_{i-1/2}^{LW} - \hat{f}_{i-1/2}^{UP}} \tag{2.13}$$

An equivalent formula can be obtained for the case of a negative wave speed $a(u) < 0$. A general formulation including the sign of the wave speed is used in the next chapter as Sweby's flux limited method is retained for the solution on the water film equation in this work.

As mentioned before the limiter function ϕ is constrained by a non-linear stability condition. For the scheme to remain in the TVD region, with $0 \leq \lambda a \leq 1$, a sufficient condition is :

$$0 \leq \phi_i^n + K \leq 2 \tag{2.14}$$

$$0 \leq \frac{\phi_i^n}{r_i^+} + K \leq 2 \tag{2.15}$$

Roe suggested this more general condition in 1989 [62] as his original paper [37] only considered the case $K = 0$.

This condition is satisfied using the flux limiter. We will describe different limiters and

their properties next after showing a variant of Sweby's method proposed by Davis and Roe.

The **Davis-Roe Flux Limited Method**. From Roe's 'TVD Lax-Wendroff' [94] , Davis proposed in [63] the following method:

$$\hat{f}^n_{i+1/2} = \hat{f}^{LW}_{i+1/2} + \frac{1}{2}|a^n_{i+\frac{1}{2}}|(1-\lambda|a^n_{i+\frac{1}{2}}|)[\phi(r^+_i)+\phi(r^-_{i+1})-2](u^n_{i+1}-u^n_i) \tag{2.16}$$

Where

$$r^+_i = \frac{u^n_i - u^n_{i-1}}{u^n_{i+1} - u^n_i} \tag{2.17}$$

$$r^+_i = \frac{u^n_{i+1} - u^n_i}{u^n_i - u^n_{i-1}} \tag{2.18}$$

This definition of the ratio r makes it a bit simpler compared to Sweby's method, although Davis dropped the idea of recovering methods such as Beam-Warming or Fromm for particular value of ϕ.

Davis originally used the minmod limiter to satisfy the non-linear stability condition although other limiters can certainly be used.

Of course flux limited methods other than the three methods presented here exist. For example, Chakravarthy-Osher [40] developed a series of semi-discrete flux-limited methods coupled with different time discretization. Also Yee [88] proposed a modified version of the Davis-Roe flux-limited method by, in particular, using a central scheme instead of the Lax-Wendroff scheme. But an exhaustive review of the flux limiting methods would be beyond the scope of this section.

Next we present the most used flux limiters in high resolution methods.

Flux Limiters

Flux limiters are used in the second stage of the high resolution methods to bound (or limit) the ''switch' ϕ , in order for the scheme to satisfy the non-linearity stability condition. In other words the function ϕ is restricted for the scheme to remain TVD.
Let consider Condition (2.15) with the constant $K = 0$ as in Sweby's paper. Under the CFL condition (Courant-Friedrich-Lewy [95, 96]), the scheme will remain non-linearly stable as long as Condition (2.15) is satisfied. Sweby's representation of the TVD region is a function of the ratio r and the limiter $\phi(r)$. Two regions are then automatically distinct: the region where the scheme is first-order and the region of higher order. While all the limiters will keep the condition (2.15) satisfied, they will use a different formulation to maintain the scheme in the higher order region.
The **minmod limiter**:

$$\phi(r) = minmod(1, br) = \begin{cases} 1 & br \geq 1 \ , \\ br & 0 \leq br < 1 \ , \\ 0 & br < 0 \ . \end{cases} \tag{2.19}$$

The minimum modulus returns the argument closest to zero if both arguments are of same sign and zero otherwise. It is written in its general form here where b is a constant such as $1 \leq b \leq 2$. We should assume $b = 1$ in which case it represents the lower boundary of Sweby's TVD region. In other words the minmod limiter brings the flux-limited method as close as possible of the first-order method while remaining second-order accurate.The

superbee limiter:

$$\phi(r) = max(0, min(2r, 1), min(r, 2)) = \begin{cases} 0 & r \geq 0 \ , \\ 2r & 0 \leq r < \frac{1}{2} \ , \\ 1 & \frac{1}{2} \leq r \leq 1 \ , \\ r & 1 \leq r \leq 2 \ , \\ 2 & r \geq 2 \ . \end{cases} \tag{2.20}$$

Apparently the name superbee would come from Roe's original paper where he used the notation B instead of ϕ for the flux limiter (see [13]). Then 'super-B' reflect the facts that it represents the upper-boundary of Sweby's TVD region. In other words, the superbee limiters brings the method as close as possible of the Lax-Wendroff method. It is said to be the most compressive method as it keeps the discontinuity very sharp. On the other hand it tends to steepen smooth transition near inflection point. (See for example Leveque, Chapter 6 of [50], which compares different limiters on an advection equation.)

The **Van Leer limiter**:

$$\phi(r) = \begin{cases} \frac{2r}{1+r} & r \geq 0 \ , \\ 0 & r < 0 \ , \end{cases} \tag{2.21}$$

Note that in order to have second-order of accuracy the limiter must respect $\phi(1) = 1$. The Van Leer limiter is very smooth near $r = 1$ whereas the two other limiters are not. This is due to the fact that around $r = 1$, the minmod and superbee limiters switch in the choice of discretization. This switch is usually referred as clipping error and represents the fact that the order of accuracy of the numerical method is reduced to a value near one. For a full second-order method a smooth limiter is required near $r = 1$.

The approach taken in this thesis follows Sweby's flux limited method. A first-order upwind and the second-order Lax-Wendroff schemes are combined with the superbee limiter. There are several reasons for this choice, the first being that this particular scheme has been extensively used in the literature and has proven to be generally very robust and accurate for many applications (see for example [47]). The second is that this thesis is in the following line of the research in ice modelling made in the AMAC department of Cranfield University. This high order scheme has already been tested and applied to ice accretion [1, 2, 3] when the department was involved in the development of ICECREMO [15]. The scheme has proven to be very reliable on structured grid so it was a first candidate and a natural choice for the unstructured code ICECREMO2.

2.4 Conclusion

Considering the runback water film in the ice model increases its complexity. The dynamics of thin film flows are very complex and so are the numerical methods to solve the equations. We have highlighted in this chapter the difficulties arising with such equations together with adequate literature. The studies for coating film flow are pertinent to aircraft icing. Spin coating and thin film flow under centrifugal force is relevant to model icing on rotating components of an aircraft or helicopter. Evolution of thin film on heated surface, in the presence of surfactant or considering evaporation offers many income for anti-icing or de-icing model. The presence of rivulets will affect the area on which ice may appear. The shape of the front may affect the amount of ice which will form. This review is far from exhaustive but instead offers a selection of the studies and general results relevant to this work.

The second part of this chapter considers the numerical methods to solve this equation. Due to the presence of shocks or sharp gradients in the solution, the classical methods are

either inaccurate or unstable. We have shown the relevance of high resolution methods for such equation. The concept of flux limiter has been explained, and the numerical method retained for this work has been presented.

In the next chapter we will continue the study further. The equation and the numerical scheme will be closely examined. A new version of this scheme for unstructured grid will be formulated. Results will be presented in two and three dimension under different physical conditions.

Chapter 3

Solving The Water Flow Equation

In this chapter a numerical method is proposed to solve the Equation 1.8 governing the ice growth presented in the previous chapter. This equation, in absence of ice formation, is typical of free surface thin film flows. Such equations are notoriously difficult to solve. For this reason the work presented in following sections deals with the water flow only. First, the different physical terms of the water flow equation will be presented, then the numerical schemes developed in the ICECREMO2 solver module MAGNUM. A finite volume formulation is presented to implement a higher resolution method on unstructured grids. The behaviour of this scheme under a typical thin film flow simulation will be shown. Results will be presented first in two-dimension with a simulation a liquid flowing down an inclined plate under different conditions, in order to illustrate the different forces involved in the equation. The extension to three dimension is done in the last section of this chapter together with more complex dynamics.

3.1 The flux terms:

The flux in Equation 1.8 may be divided into four terms, $Q = Q_1 + Q_2 + Q_3 + Q_4$:

1. Q_1 describes the influence of the shear stress. This is the dominant term over most

of the domain.

$$Q_1 = \frac{Ah^2}{2\mu} . \tag{3.1}$$

2. Q_2 is the gravity term. This term is likely to become dominant when the substrate is inclined significantly and the shear stress value is close to 0.

$$Q_2 = \frac{\rho_w g_x h^3}{3\mu} . \tag{3.2}$$

3. Q_3 is a pressure term. This term may only be dominant when the water height varies rapidly, *i.e.* near the moving front

$$Q_3 = \frac{\rho_w g_z h^3}{3\mu} \frac{\partial h}{\partial x}. \tag{3.3}$$

4. Q_4 is the surface tension term. This is another non-linear term with a third-order derivative:

$$Q_4 = C \frac{h^3}{3} \frac{\partial^3 h}{\partial x^3} . \tag{3.4}$$

where C is the inverse capillary number, the ratio of surface tension and viscosity.

If gravity, pressure and surface tension are neglected, the flux is reduced to Q1 and the water film equation is the well-known inviscid Burgers' equation.

In order to understand the physics of the thin film flow, and how they are modeled, a simple flat plate case is presented in Figure 3.1 in two dimensions. This case is used as a base to compare different methods and see the effect of different forces on the water film. The mass flux representing the incoming water is applied in the centre of the plate in a gaussian shape. The shear stress is acting constantly in uniform direction (here from left

to right), and the plate is considered horizontal first so gravity is acting in the vertical direction only.

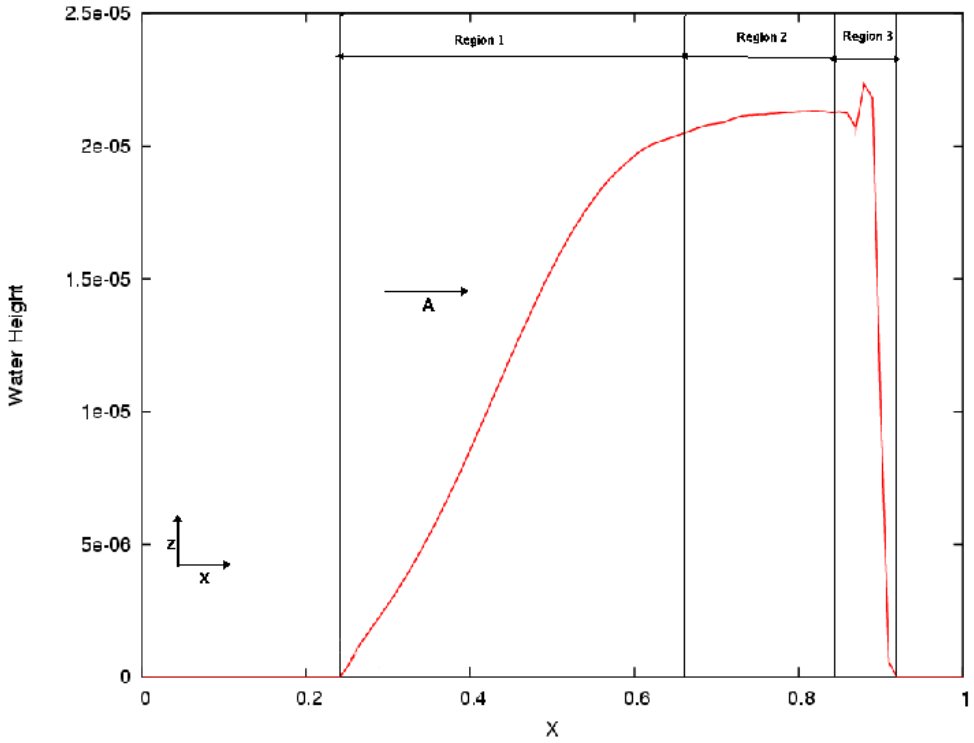

Figure 3.1: Typical water film shape.

The water is pushed toward the right by the shear force $\overrightarrow{A}$. After a certain amount of time, 0.2 sec in this case, a Lax-shock starts to form (Region 3) and spreads as the water advances on the plate. Region 1 is the flow development region where the water flux from impinging droplets enters the domain (impinging droplets). Region 2 represents the pseudo-steady state reached by the water film. The height of the water film in this region will stay constant. Only the length, here in the x direction, will change with time as the front advances on the domain. The numerical modelling of this type of flow requires advanced techniques such as shock capturing methods.

3.2 The numerical schemes

The linear theory use the Lax-Ritchmeier theorem to insure the convergence of a numerical scheme. In this case, consistency and stability offer a sufficient and necessary condition for the scheme to converge. The Von Neumann analysis is the most used technique to obtain a stability condition for linear schemes. The concept of necessary and sufficient condition for convergence is expanded in [45]. For non-linear conservation laws the theory is more complex. As shown previously in Chapter 2, such equation can have several solutions due to the presence of discontinuity. An entropy condition is necessary for the scheme to converge to the weak solution. For an arbitrary flux function $f(u)$, such condition is the Rankine-Hugoniot jump condition [48]. In the scalar case, this gives:

$$s = \frac{f(u_l) - f(u_r)}{u_l - u_r} \tag{3.5}$$

where s is the speed at the discontinuity, u_l and u_r the value on the left and right of the propagating shock.

Secondly, the scheme must be written in its conservative form. Some examples have also been cited in the previous chapter where a non-conservative scheme failed to solve correctly Burger's equation. More generally, a numerical scheme written in conservative form ensures that, in absence of sources, the physically conserved quantities according to the partial differential equation are numerically conserved by the finite difference equation. The schemes in this section are written in their structured form as found in the literature. The data are indexed with the subscript i and denote a face centered value. Index $i + 1/2$ represents a value computed at the edge, interface between two faces. The unstructured edge-based formulation is presented and explained in the next section. For the reason of clarity, the numerical schemes presented in this section are written in 2D. Extension to 3D structured grid can be easily obtained using $Q = Q_x + Q_y$.

Equation 1.8 is solved numerically with an explicit scheme which can be written in the following conservative form:

$$h_i^{k+1} = h_i^k - \frac{\Delta t}{\Delta x}\left(Q_{i+1/2}^k - Q_{i-1/2}^k\right) \ , \tag{3.6}$$

where the superscript ^{k} and the subscript $_i$ denotes values at $t = k\Delta t$ and $x = i\Delta x$ respectively.

3.2.1 Original implementation

The original implementation of the numerical scheme in ICECREMO2 used a flux splitting technique. The shear stress component of the flux Q_1 of 3.1 is implemented using an upwind scheme:

$$Q_{i+\frac{1}{2}} = \begin{cases} Q_i & \text{if } \ a_{i+\frac{1}{2}} > 0 \ , \\ Q_{i+1} & \text{if } \ a_{i+\frac{1}{2}} < 0 \ , \end{cases} \tag{3.7}$$

$$a_{i+\frac{1}{2}} = \frac{(\frac{\partial Q}{\partial h})_i + (\frac{\partial Q}{\partial h})_{i+1}}{2} \tag{3.8}$$

$$\frac{\partial Q}{\partial h} = \frac{Ah}{\mu} \ . \tag{3.9}$$

When the gravity and pressure terms (3.2) and (3.3) are discretised using a central scheme:

$$Q_{i+\frac{1}{2}} = \frac{Q_i + Q_{i+1}}{2} \tag{3.10}$$

Although this implementation is adequate for most of the aeronautical test cases, it suffers from two major problems. In most of the test cases in aeronautic, the shear stress would be highly dominant over the gravity and pressure terms. However, for practical reasons,

the simulation on rotative component is done using centripetal acceleration (see rotating case), and in this particular case, the gravity forces becomes dominant over the shear forces. The flux (3.2) is then the main term. The central scheme being unstable this numerical implementation is then unable to solve the equation for rotating components.

The second drawback is the behavior of this scheme around the stagnation line or sonic point. This issue will be assessed in more detail later but here is a brief description of the phenomena. By definition, the upwind scheme is dependent of the direction of the flux represented by the sign of the wave speed. Around the stagnation line, the value of the wave speed is close to zero. It has been noticed that on a particular cell situated on this stagnation line, the wave speed could take alternatively positive or negative values. These oscillations over time prevent the upwind scheme to converge on this region, changing at every time step the direction of the discretization.
In the next section a scheme is proposed which will yield to a better approximation and overcomes these problems.

3.2.2 Higher order scheme

In this section the entire flux Q is considered, no splitting formulation is performed. The Lax-Wendroff scheme is implemented using the following formula:

$$Q^{LW}_{i+1/2} = \frac{1}{2}(Q_{i+1} + Q_i) - \frac{\Delta t}{2\Delta x} A^2_{i+1/2}(h_{i+1} - h_i) \tag{3.11}$$

Where the wave speed is:

$$A_{i+1/2} = \begin{cases} (Q^k_{i+1} - Q^k_i)/(h^k_{i+1} - h^k_i) & \text{if } \; h^k_{i+1} - h^k_i \neq 0 \ , \\ \partial Q^k/\partial h\Big|_{i+1/2} & \text{if } \; h^k_{i+1} - h^k_i = 0 \ , \end{cases} \tag{3.12}$$

The scheme is second-order in space, it is conditionally stable providing that the CFL

condition is satisfied. It is both diffusive and dispersive, so in presence of singularities like shocks some oscillations are present due to the dispersion, see Figure 3.2.

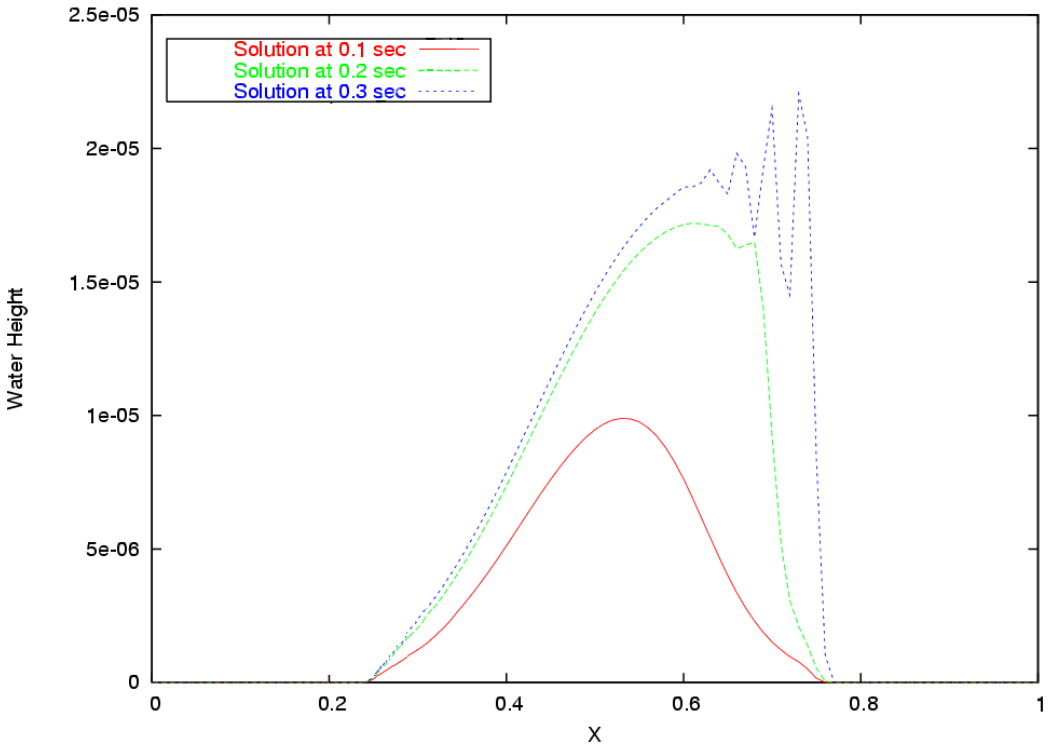

Figure 3.2: Water film computed with a Lax-Wendroff scheme. When the front sharpens, spurious oscillations appear and spread with the liquid.

When the solution is smooth and until a Lax-shock is formed at $t = 0.2s$, the Lax-Wendroff scheme shows good results. When shocks form and propagate, spurious oscillations appear and can lead to non-physical instabilities. These results correspond with those obtained by [47] when applying this scheme to the inviscid Burgers' equation.

3.2.3 High resolution method

The numerical scheme developed by Sweby and Roe combines a second-order accurate Lax-Wendroff scheme with the first-order Upwind scheme to provide a smooth solution. This scheme has been used for this same equation and has proven to be efficient and more

accurate in continuous and near shocks (see:[2]). See [47] to see it applied to the inviscid Burger's equation.

The conservative form (3.6) is kept, the flux is discretised in the following manner:

$$Q^k_{i+1/2} = (1 - \phi(r))Q^{UP}_{i+1/2} + \phi(r)Q^{LW}_{i+1/2} \tag{3.13}$$

Where $\phi(r)$ is the Superbee limiter [37].

The upwind scheme is defined as:

$$Q^{UP}_{i+1/2} = \frac{1}{2}(Q_{i+1} + Q_i) - \frac{1}{2}sign(A_{i+1/2})(Q_{i+1} - Q_i) \tag{3.14}$$

And the Lax-Wendroff as:

$$Q^{LW}_{i+1/2} = \frac{1}{2}(Q_{i+1} + Q_i) - \frac{\Delta t}{2\Delta x}A^2_{i+1/2}(h_{i+1} - h_i) \tag{3.15}$$

Where the wave speed is:

$$A_{i+1/2} = \begin{cases} (Q^k_{i+1} - Q^k_i)/(h^k_{i+1} - h^k_i) & \text{if } \; h^k_{i+1} - h^k_i \neq 0 \ , \\ \partial Q^k/\partial h\Big|_{i+1/2} & \text{if } \; h^k_{i+1} - h^k_i = 0 \ , \end{cases}$$

The limiter is implemented with the following formula:

$$\phi(r) = max\left(0, min(2r, 1), min(r, 2)\right) \tag{3.16}$$

$$r = \frac{\left(|a_{i+\frac{1}{2}-s}| - \lambda a^2_{i+\frac{1}{2}-s}\right)(h_{i+1-s} - h_{i-s})}{(|a_{i+\frac{1}{2}}| - \lambda a^2_{i+\frac{1}{2}})(h_{i+1} - h_i)} \tag{3.17}$$

$$s = sign(a_{i+\frac{1}{2}}) \tag{3.18}$$

The linear combination of upwind and Lax-Wendroff form a shock capturing scheme. The diffusive property of the upwind scheme has the advantage of damping the spurious oscillations produced by the Lax-Wendroff scheme near the shock, see Figure 3.3. Hence the scheme will be of second-order everywhere but in the vicinity of the front where it will be only first-order accurate in space.

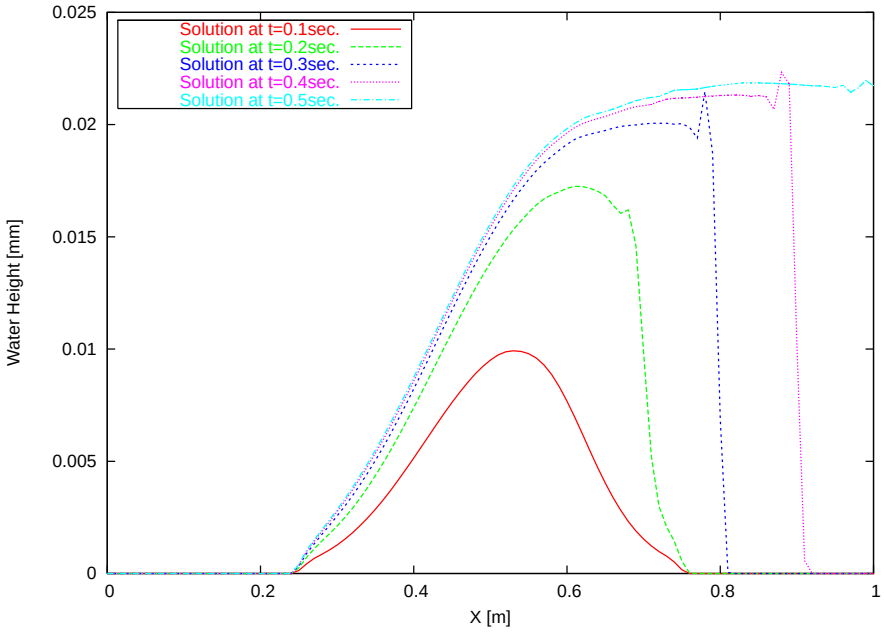

Figure 3.3: Evolution of the water film on a flat plate with time. The high resolution method removes the spurious oscilations previously visible.

3.3 Finite Volume formulation

3.3.1 The edge-based formulation

The numerical schemes in ICECREMO2 were implemented in the function defined as *CalcRHS()* in order to compute $\nabla.Q$ on each cells. On each face, $\nabla.Q$ is estimated with edge based values using Gauss's theorem:

$$\nabla.Q \approx \frac{1}{F}\sum_{i=1}^{N} \overrightarrow{q_i}.\overrightarrow{n_i}.E_i \tag{3.19}$$

where F is the area of the face.

It will be shown in this section how $\overrightarrow{Q_e}$, the flux on each edge, is computed using the Superbee limiter.

The upwind and Lax-Wendroff part are computed in the following manner:

$$Q_e^{UP} = \begin{cases} Q_{Left} & \text{if } \ sign\,(A_e) = 1\ , \\ Q_{Right} & \text{if } \ sign\,(A_e) = -1 \end{cases}$$

$$Q_e^{LW} = \frac{1}{2}(Q_{Right} + Q_{Left}) - \frac{\Delta t}{2\Delta x} A_e^2 (h_{Right} - h_{Left}) \tag{3.20}$$

where the superscripts UP and LW stand for the upwind and Lax-Wendroff respectively. A_e is the wave speed defined as:

$$\overrightarrow{A_e} = \begin{cases} \frac{Q_{Right} - Q_{Left}}{h_{Right} - h_{Left}} & \text{if } \ h_{Right} - h_{Left} \neq 0\ , \\ \\ \frac{\frac{\partial Q}{\partial h}\big|_{Right} + \frac{\partial Q}{\partial h}\big|_{Left}}{2} & \text{if } \ h_{Right} - h_{Left} = 0 \end{cases} \tag{3.21}$$

And its sign is the sign of : $< \overrightarrow{A_e}, \overrightarrow{N_e} >$ where $\overrightarrow{N_e}$ is the normal of the edge computed using the diagram presented in Figure 3.4 where N_l and N_r represent respectively the normal to the left and right face.

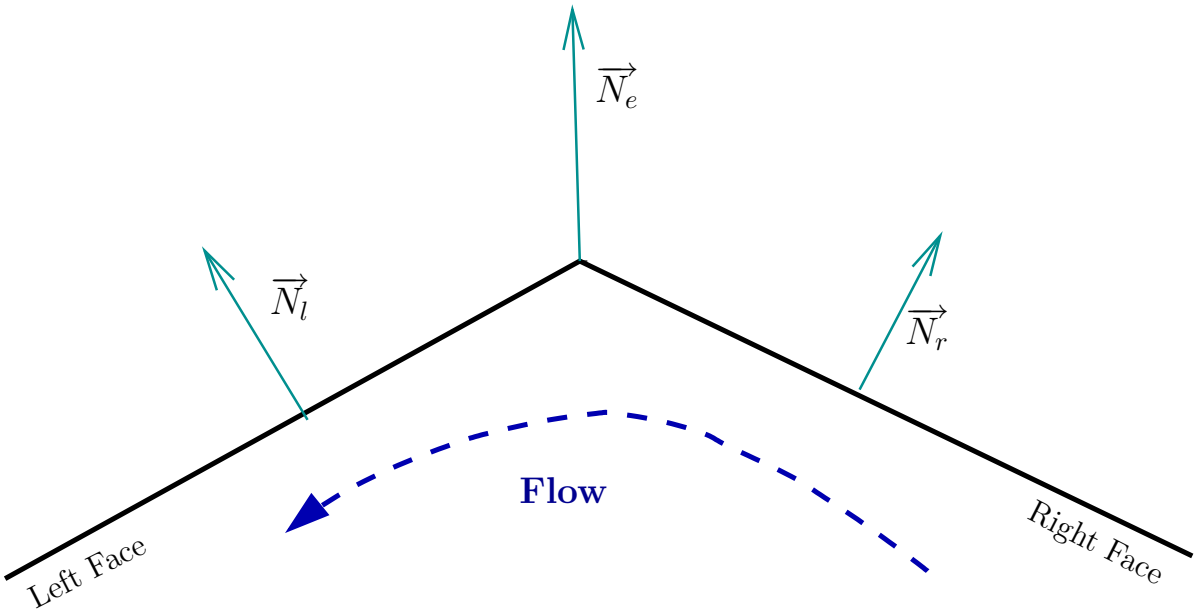

Figure 3.4: Definition of the vector normal to the edge as sum of the normal to the neighbouring cells

3.3.2 The virtual cell

The main difficulty to implement the full scheme on unstructured grid is the flux limiter itself. It can be seen in Equation 3.17, that the computation of r, in the worse case, requires the access to the value of the water height h and to the wave speed on a range of three neighboring cells. Due to the edge-based structure of the SOLAR library, this is very difficult to obtain.

Basically, when looping over an edge, only the access to any value X_{left} or X_{right} centered in the two neighboring cells is available. See Figure 3.5: to construct the flux $\overrightarrow{q}$ on the edge on need the values on the remaining two edges of the right cell (represented as square). If a larger stencil is required, one could try to track the next cell in the direction of the flow. However, this would be very expensive in terms of computation, as one would have to loop over all cells. This would also be very unreliable for complex mesh structures as it would require special treatment near the boundaries.

A more practical idea to overcome this problem is to reconstruct a value on a fictious cell using the gradient of this value on the neighboring cells. If the access to these values is needed on more than two space level, a fictious value X_f is created in the same direction, see Figure 3.5 (blue square). For example, $X_f = X_{right} + < \overrightarrow{LR}, \overrightarrow{\nabla . X_{right}} >$.

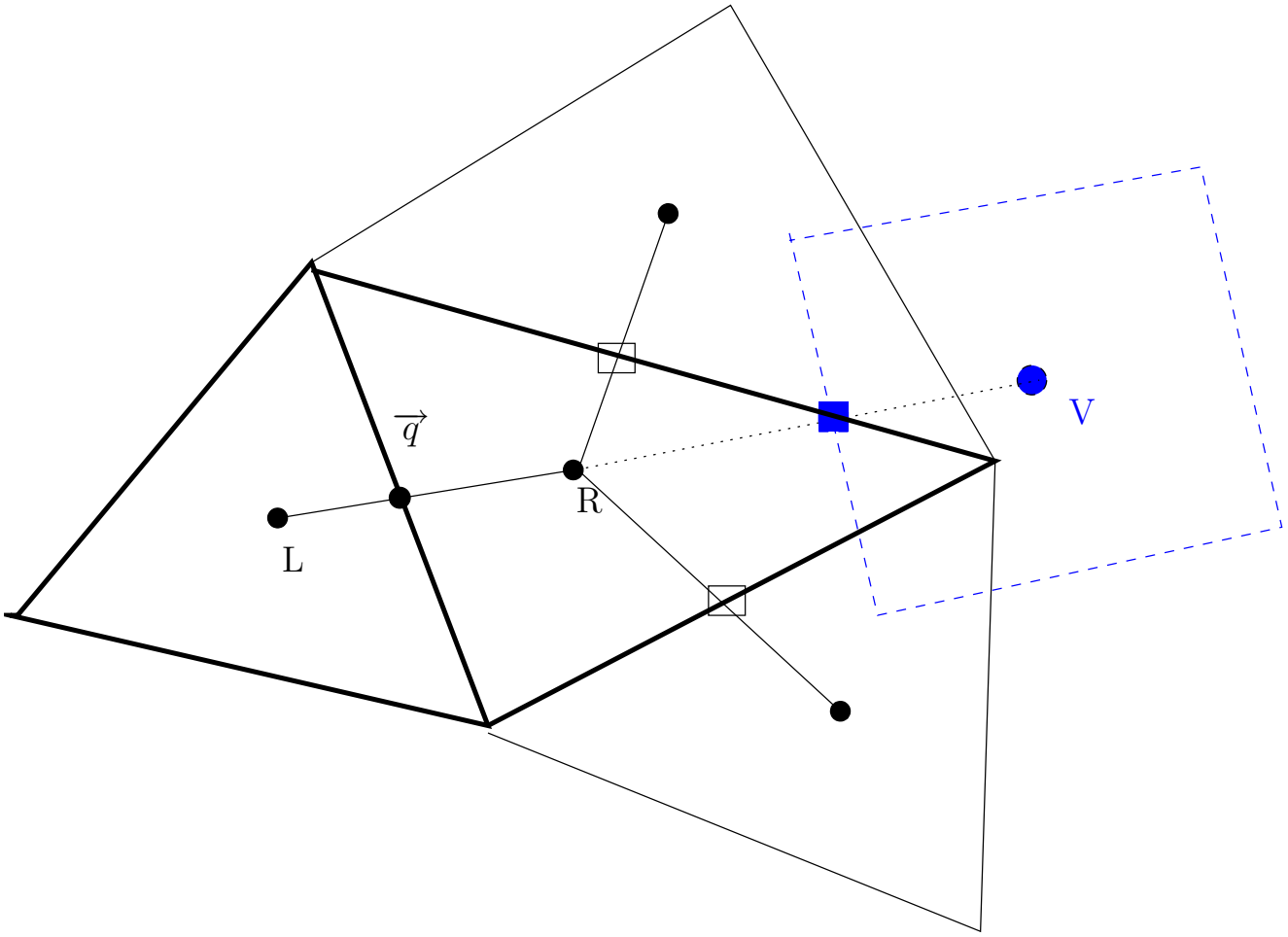

Figure 3.5: Construction of the virtual cell value for the definition of the limiter

In (3.17), if $s > 0$, the formulation for the limiter becomes:

$$r = \frac{(|a_{virtual}| - \lambda a_{virtual}^2)\,(h_{Right} - h_{virtual})}{(|a_{edge}| - \lambda a_{edge}^2)(h_{Right} - h_{Left})} \tag{3.22}$$

Note that the wave speed $\overrightarrow{A}$ is a vector. In the calculation of the ratio r, $a_{virtual}$ is the scalar product of the wave speed evaluated on the virtual cell and the normal of this cell. In the following results, the wave speed on the virtual cell has been evaluated using the virtual water height value and the exact derivative formulation. For that, the shear stress is calculated on the virtual cell using linear interpolation.

With Formula 3.22 if the gradient of h is smooth, the ratio:
$\frac{h_{Right}-h_{virtual}}{h_{Right}-h_{Left}} \simeq 1$ which would reduce the entire scheme to the Lax-Wendroff scheme. This is exactly what we want, as we are looking for a second-order scheme where the solution is smooth and an upwind near the front.
On the Figure 3.6 a plot is shown of the time history on one particular edge and respective Left face of the value of the water height , the ratio r and the limiter ϕ.

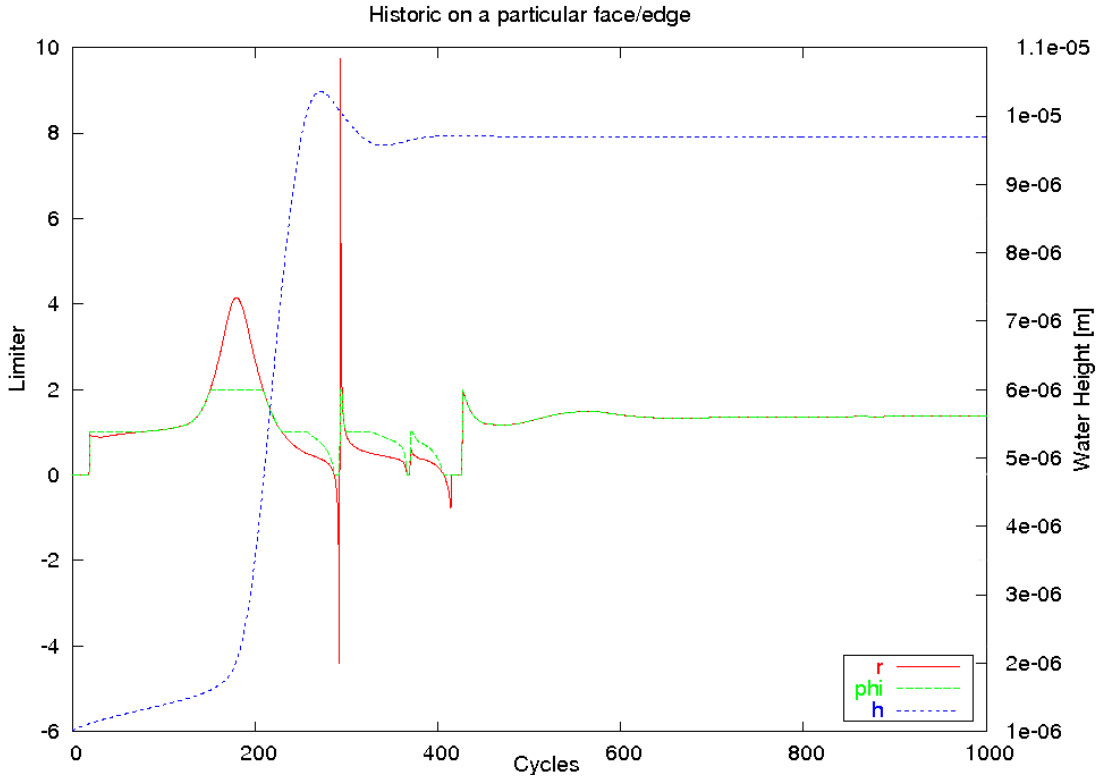

Figure 3.6: Evolution of h, r and ϕ on a particular face/edge with time

It can be seen with the water height historic, in green on the figure, that on this particular cell the shock arrive shortly after 500 cycles. The limiter ϕ is the restriction of the ratio r to the interval [0:2].

It can be observed that as the shock is passing by, over this particular edge, that the value of the limiter is changing. While the shock is over this particular region, the limiter reduces its value making the upwind scheme the dominant contribution to the global scheme. Once the shock has passed, the water film has reached its equilibrium height on this region and the limiter recovers its value of 2 making the global scheme second-order accurate.

Before the water reach this particular face, the water height is equal to the height of the precursor film so $\Delta h = 0$. Then, both Δh evolve when the shock reach the face and it reflects exactly the typical shape of the shock, Region 3 in (3.1). Once the shock has passed, the film height is in its pseudo-steady state , Region 2 in 3.1, so $\Delta h = 0$ again. In the following it can be seen first in Figure 3.7: Δh on the extended stencil , i.e.:$h_{Right} - h_{virtual}$; and secondly in Figure 3.8 the local $\Delta h = h_{Right} - h_{Left}$ together with the water height on the left face.

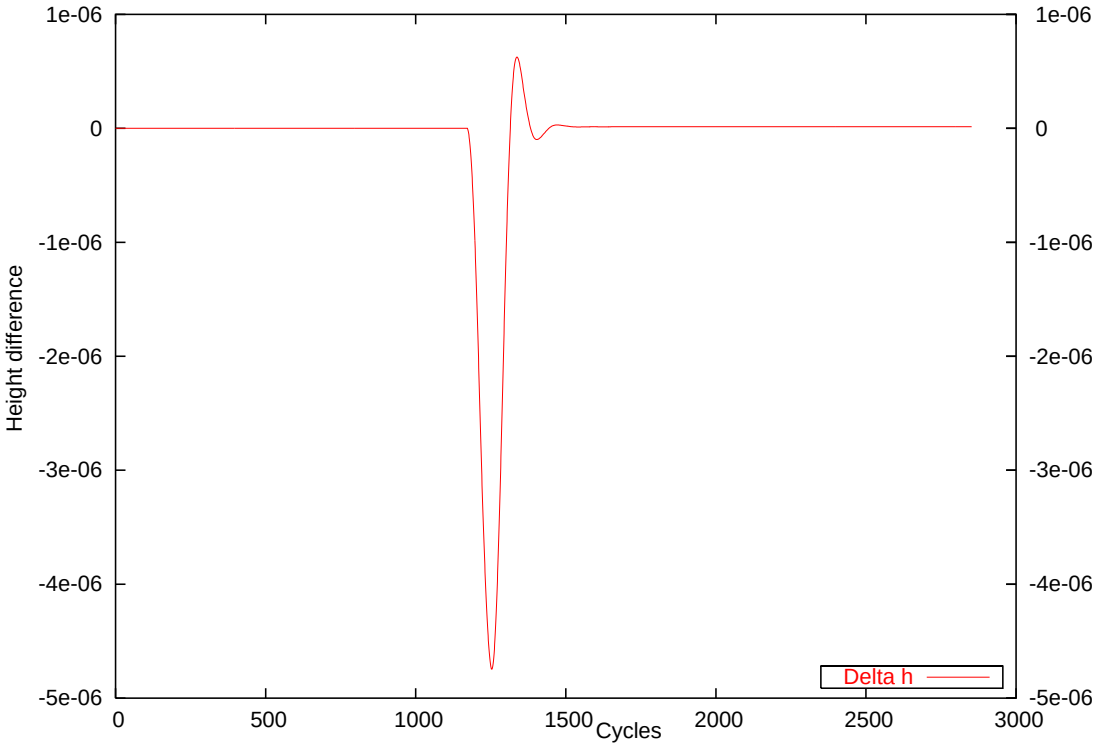

Figure 3.7: Evolution of $h_{Right} - h_{virtual}$

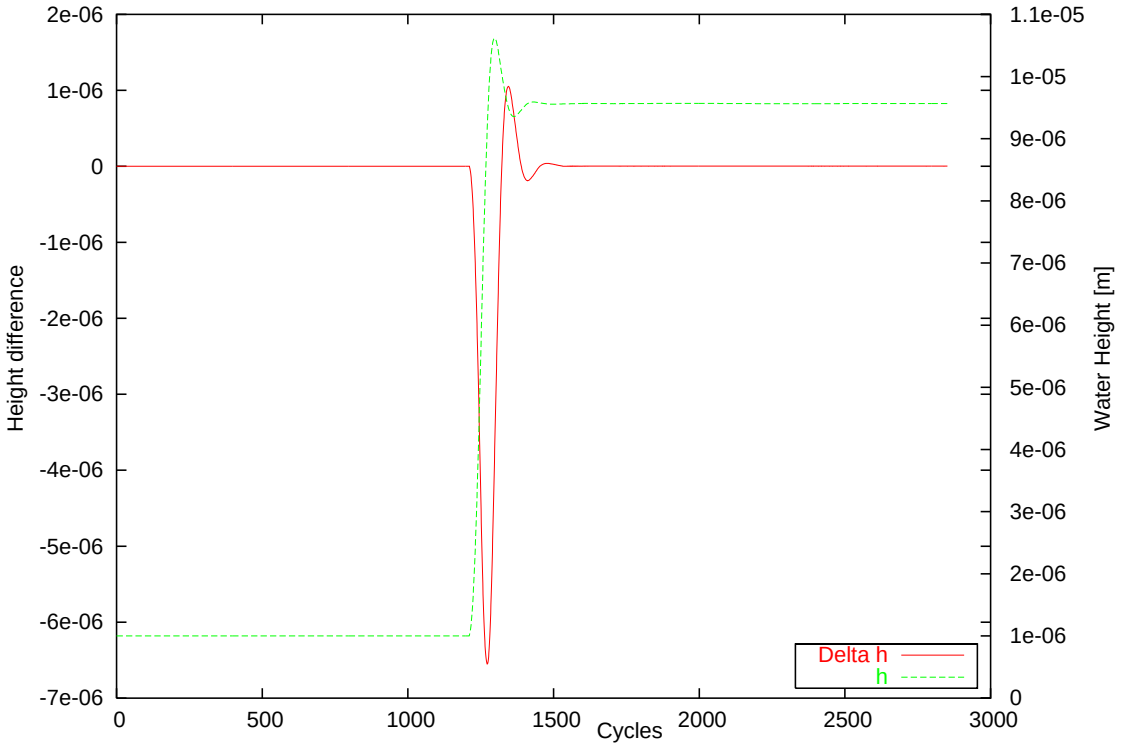

Figure 3.8: Evolution of $h_{Right} - h_{Left}$ and h on a particular cell

This sequence of figures allows us to check the behavior of the numerical scheme and its limiter under a typical simulation. This also confirms that the finite volume formulation and the different approach that had to be taken in order to implement this scheme on unstructured grid does not affect the overall solution by introducing more error. The study is carried on in the next section by looking more thoroughly into the different forces involved in the thin film equation and their influence on the final film shape.

3.4 Preliminary results in 2D

In this section, several calculations will be performed varying the different variables or initial conditions. The main idea is to give the reader a good understanding of the physics of the type of flow satisfying Equation 1.8. Let's start with a simple 2D flat case on which different angle of inclination are tested to show the impact of the gravity forces on the film shape.

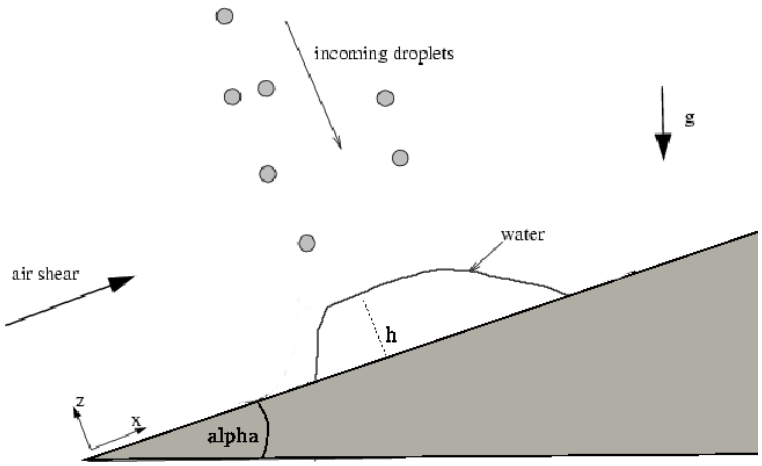

Figure 3.9: The 2D flat case.

The collection efficiency for this case has a gaussian shape (exponential inverse) centered at $x = 0.3m$. The length of the plate is $L = 1m$. The shear stress is parallel to the plate and gravity is acting vertically, $g_z = -9.8ms^{-2}$. For an angle $\alpha = 0$, the plate is at the horizontal position and results similar to those presented earlier are retrieved.

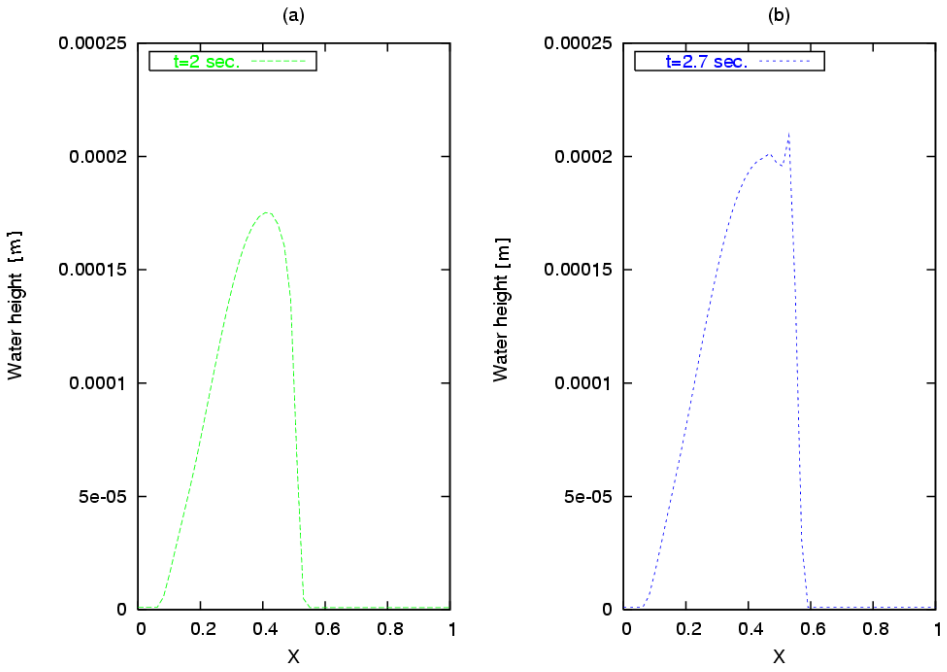

Figure 3.10: The early stage: as the liquid starts moving, the front sharpens.

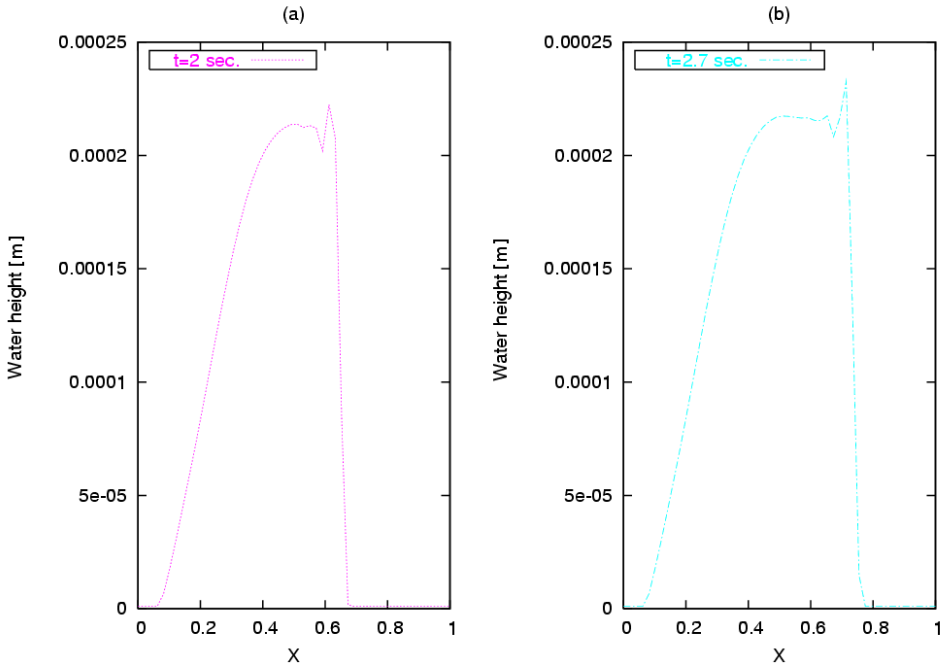

Figure 3.11: The front wave is forming .

As the incoming water enter the domain , the shear stress acting from left to right is pushing slowly the liquid toward the right. In Figure 3.10(a), the initial gaussian shape of the catch can still be observed but with a slight asymmetry. As the water advances on the plate the slope is increasing and rapidly becomes very sharp. Around $t = 2s$ the shock starts to form.

This shock will rapidly evolve to a constant shape. This front wave shape is typical of thin film flows [1].

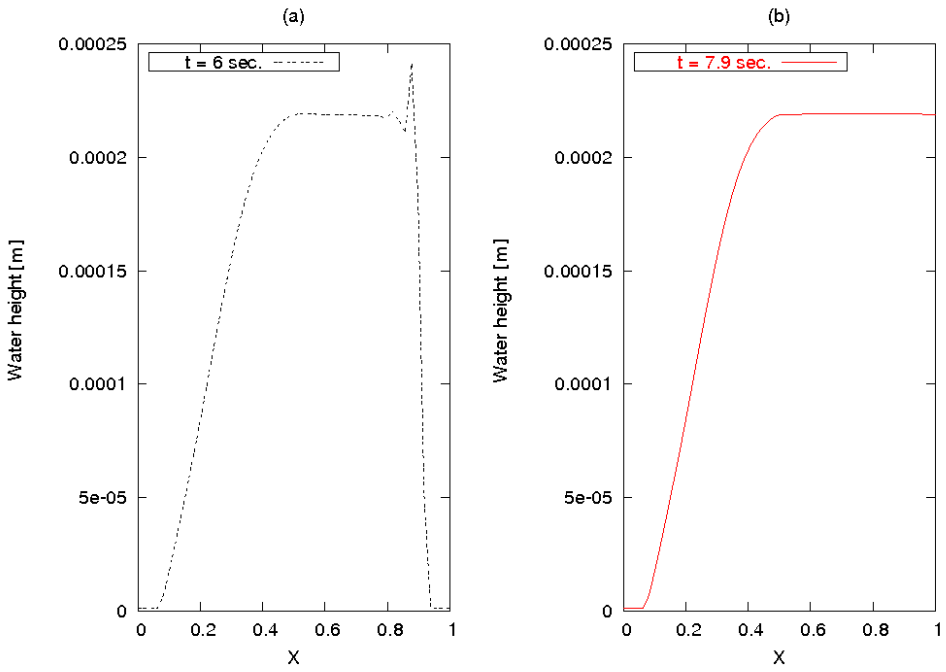

Figure 3.12: The water film reaches a quasi-steady state.

The film then reaches a quasi-steady state. As depicted in Figure 3.1, the film can be divided into three parts. The flow development region (Region 1 in Figure 3.1) remains unchanged. The central part of the flow (Region 2 in Figure 3.1) is in an equilibrium height and only its length will vary with time. The front wave (Region 3 in Figure 3.1) keeps the same shape and is moving toward the right as the liquid advances on the domain.

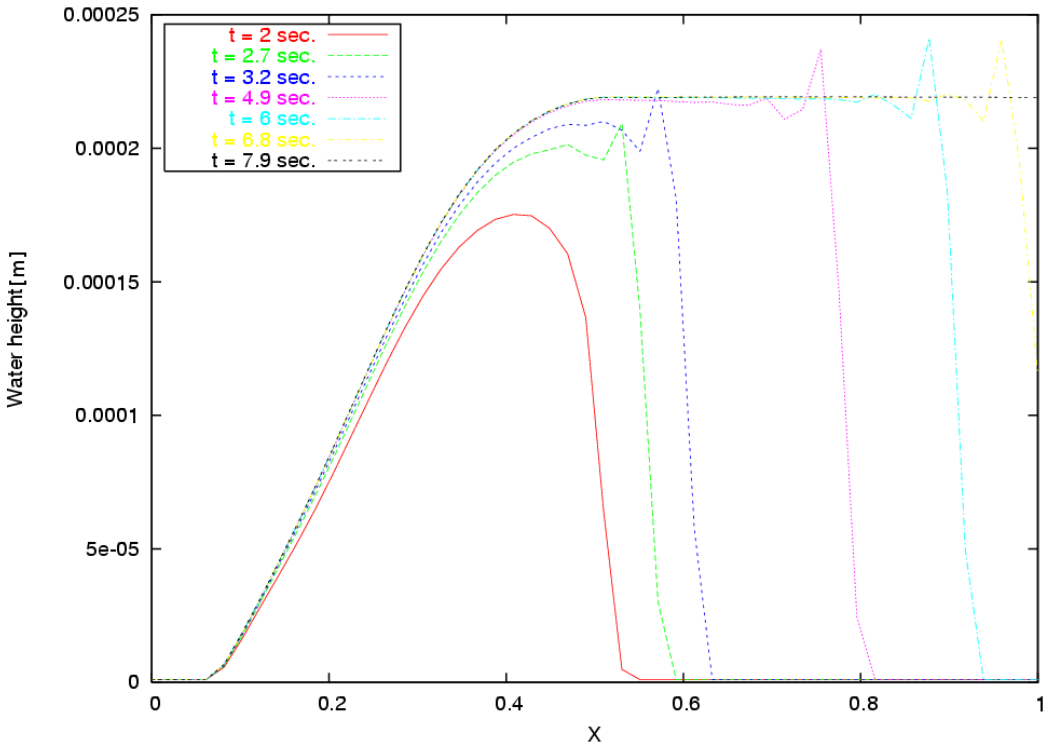

Figure 3.13: Evolution of the water film with time on a horizontal plate

The results on an horizontal plate are in good agreement with those found in the literature, see [1] for example. In the following paragraphs it is shown how the different forces influence the front wave.

3.4.1 Angle of inclination

Negative angles

If the angle α is negative, the gravity will act in the same direction as the shear stress. The speed of the wave front is increased and the flow reaches its pseudo-steady state a bit earlier.

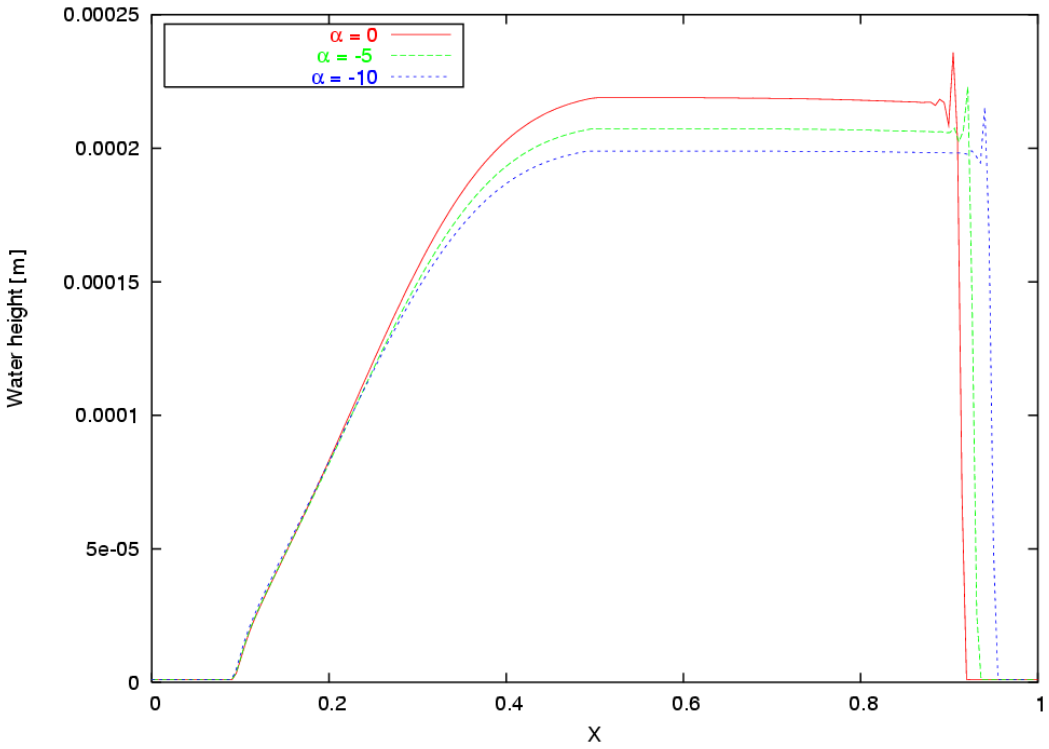

Figure 3.14: Water film at t = 6 s, for $\alpha = 0°, -5°$ *and* $-10°$

The shape of the front wave remains unchanged. The equilibrium height is decreasing with the angle of inclination. The more the plate is inclined the faster the film is. Gravity is acting with shear stress to stretch the water film over the plate which result, for a same exposure time, to a thinner but longer film.

Positive angles

On the opposite, if the angle α is positive, gravity and shear stress will act in opposite directions. As shown in Figure 3.15, for relatively small angles gravity will only be slowing down the flow yielding in a higher equilibrium height.

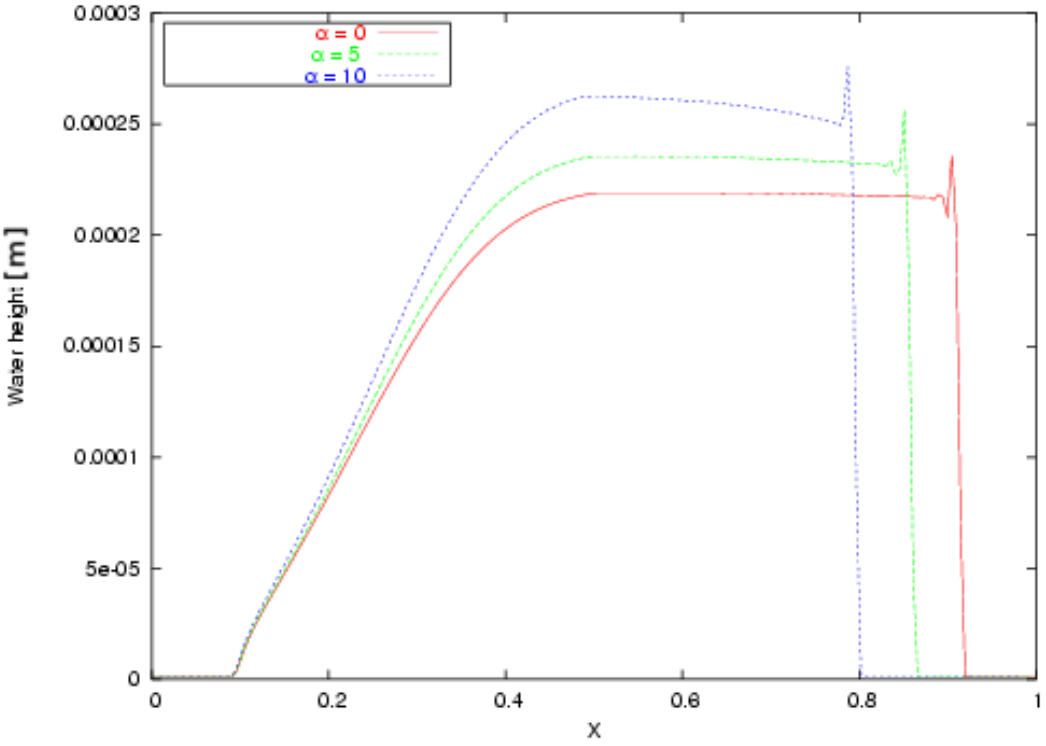

Figure 3.15: Water film at t = 6 s, for $\alpha = 0°, 5°$ *and* $10°$

- For $\alpha = 5°$, gravity has a compressive effect on the flow. Still, the shear stress is dominating and the water is propagating on the plate but with a lower speed. The wave front shape remains unchanged and the global shape of the film stays as described previously for horizontal plates, except for the value of the equilibrium height.

- For $\alpha = 10°$, gravity forces have a bigger impact on the film. The front wave shape begins to change. The main difference is in the flow development region and the steady state region. As less water is pushed through the right side of the plate by the shear stress, the liquid accumulates to the central part of the plate. No equilibrium height is reached yet.

In the following we will observe more closely what happens when gravity takes over shear stress. The angle of inclination is increased to 20°. The evolution of the water film is significantly different, see Figure 3.16. First results obtained without surface tension are presented. The angle of inclination has been chosen to obtain a balance between the shear stress and the gravity forces. Surface tension is added later to observe its effect.

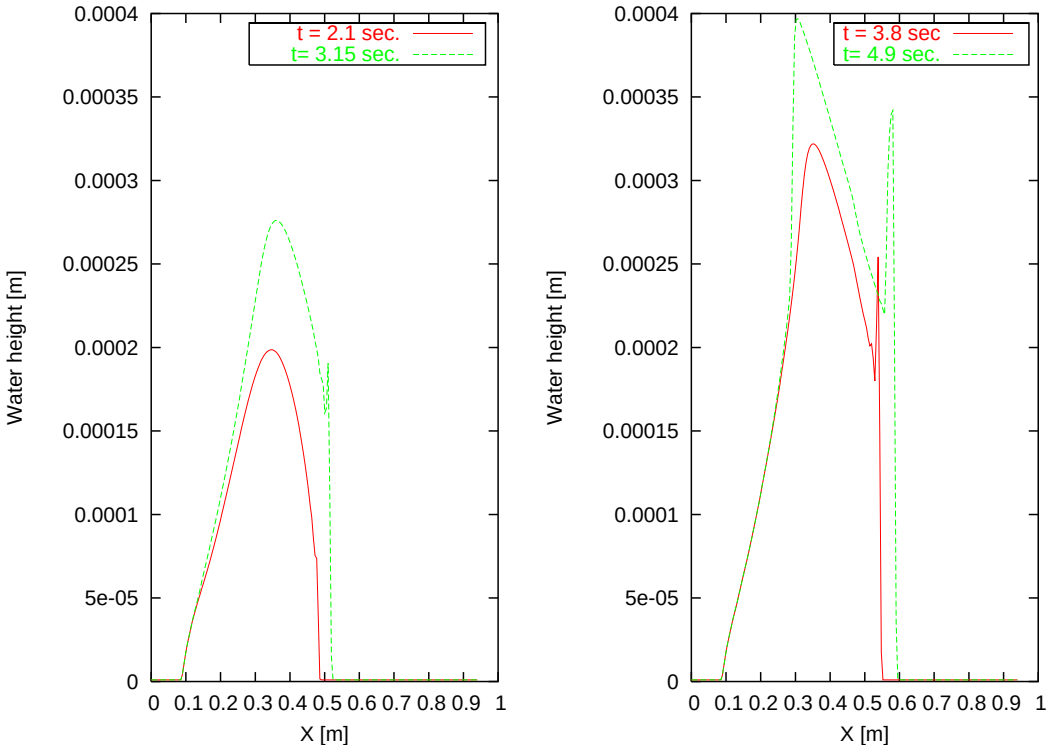

Figure 3.16: Water film for $\alpha = 20°$, first stage.

It can still be observed that the formation of a Lax shock as the wave front becomes steeper. The central bulk does not take the shape of the catch and is deformed by the effect of gravity. As the shear stress is pushing the liquid up the plate (to the right), gravity acts in the opposite direction and forces the water to the bottom of the plate (to the left).

The wave front advances very slowly towards the top of the plate. The maximum height reached by the shock is higher, and as it reaches its maximum, the shock begins to increase

in width, see Figure 3.17. Soon a plateau forms behind the shock. As liquid will pile up, the length of the plateau will extend. This type of shape has been observed experimentally. The gap between the plateau and the rest of the liquid on the left part of the plate is known as undercompressive shock [84]. As time goes on and the plateau extends the gap is closing up and the undercompressive shock disappears.

The height of the plateau comes to an equilibrium height, see Figure 3.18 (a). And as the undercompressive shocks completely disappears the film can be considered again in a pseudo-steady state where only its length is varying with time, see Figure 3.18 (b). As time goes on now the liquid is advancing towards the left, the bottom of the plate, under gravity effect.

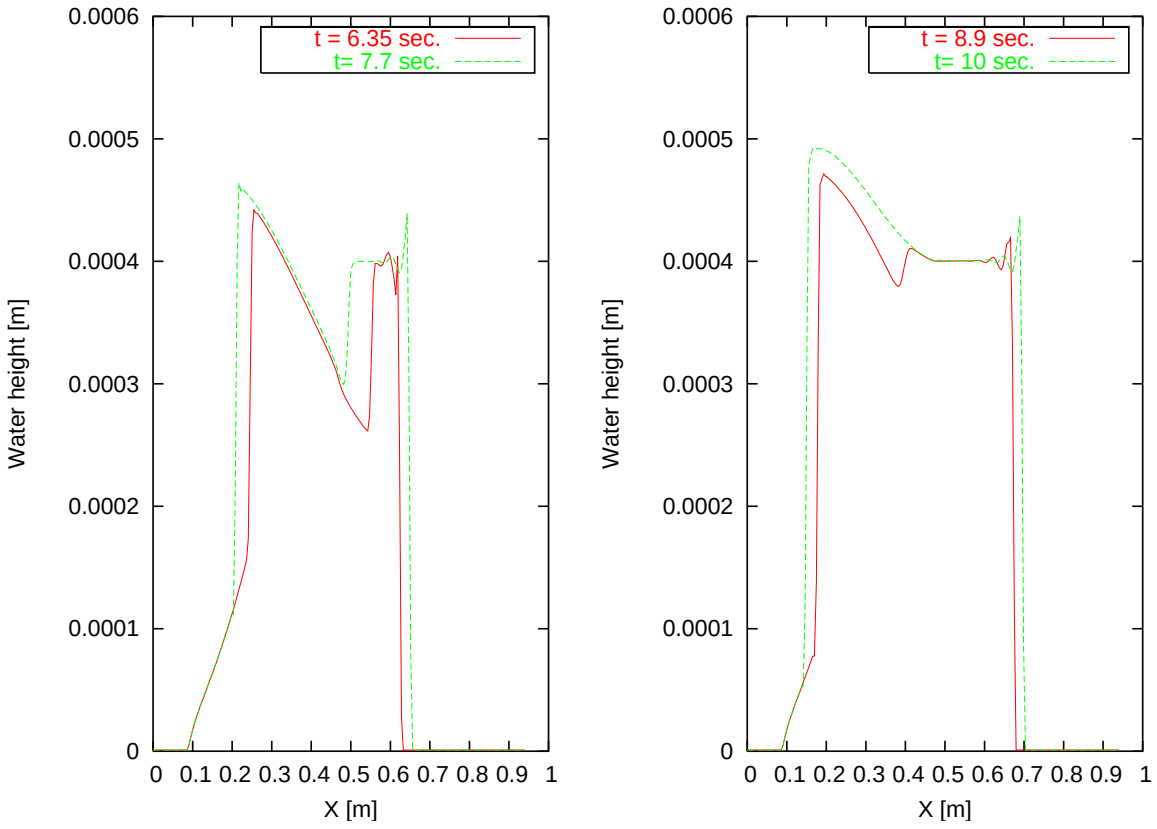

Figure 3.17: Water film for $\alpha = 20°$, second stage

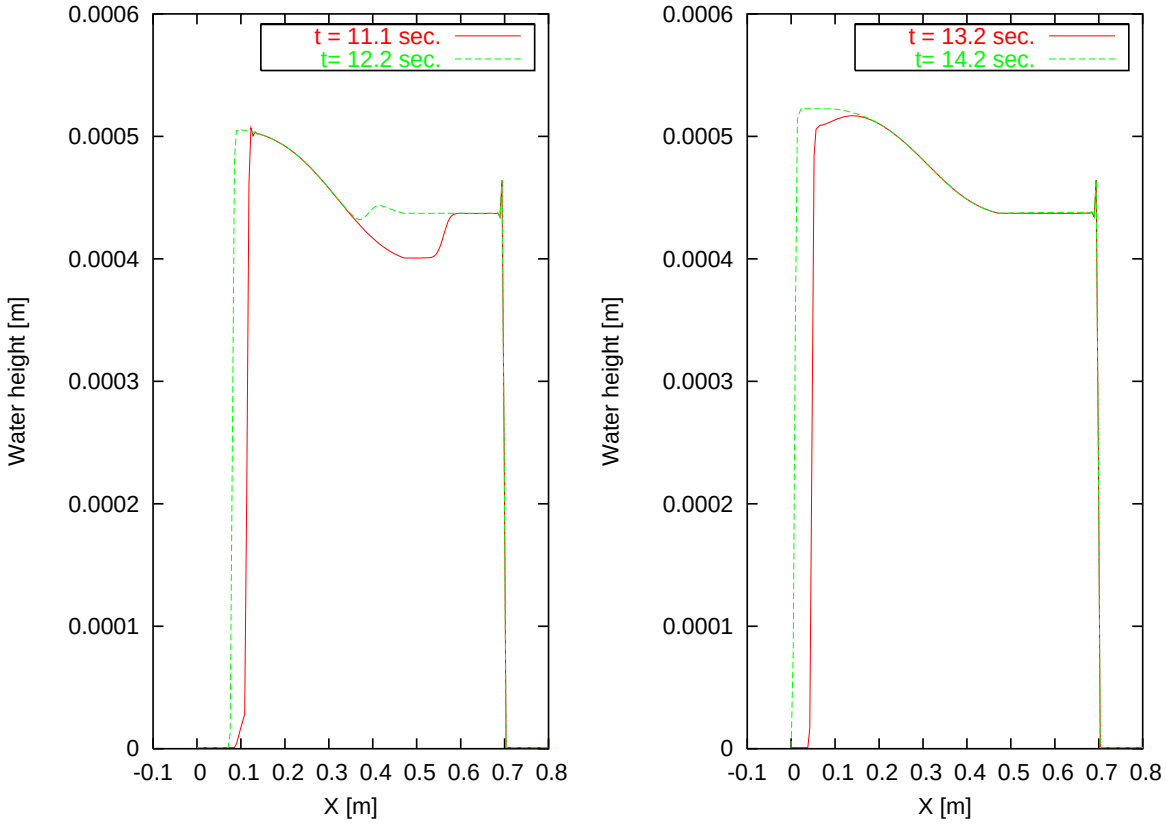

Figure 3.18: Water film for $\alpha = 20°$, final stage

In this section, the flow of a water film on a flat surface has been considered under different conditions. This has permitted two things. First we have been able to illustrate the different shapes that the front wave can take as well as the influences of the different forces, represented by the Fluxes (3.1), (3.2), (3.3) and (3.4), on the final solution. Secondly this validates the scheme in its finite volume formulation, presented in the previous section. In the next section we extend the study to the third dimension and with more complex test cases.

3.5 Preliminary results in 3D

In this section we present some water film simulations in three dimensions. The calculations are done on an ideal surface, a flat plate, under various conditions but on a regular grid. For a better visualization, the water height has been magnified by a factor of 1000 in all the figures, so we can fully appreciate the structure of the film.

The first example shown in Figure 3.19 represents a liquid spreading over an horizontal flat plate under shear stress forces. The shear stress is acting parallel to the plate equally in x and y direction. (i.e.: its vector is collinear to (1,1,0).)

The initial conditions for the water film is a 3D gaussian, representing the impinging droplet zone. The solution is output at regular interval, in the next calculation a time unit is approximately 0.1 seconds.

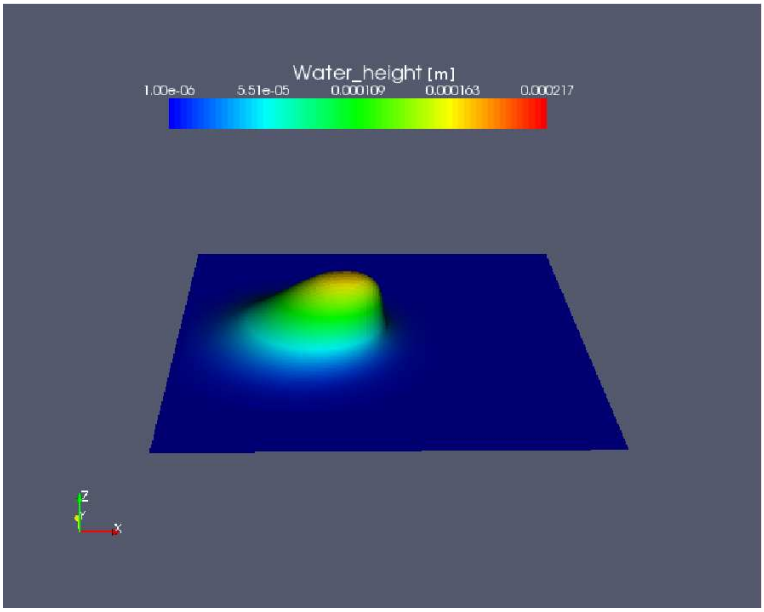

Figure 3.19: Water film on an horizontal plate at $t = 0.1s$

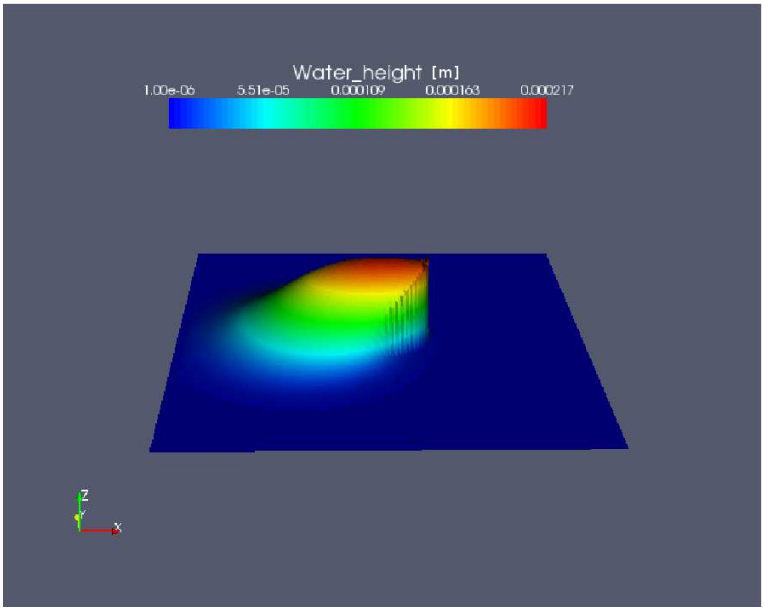

Figure 3.20: Water film on an horizontal plate at $t = 0.3s$

In Figures 3.19 and 3.20 we can observe how the initial gaussian shape it pushed by the shear stress to force the water towards the right corner.

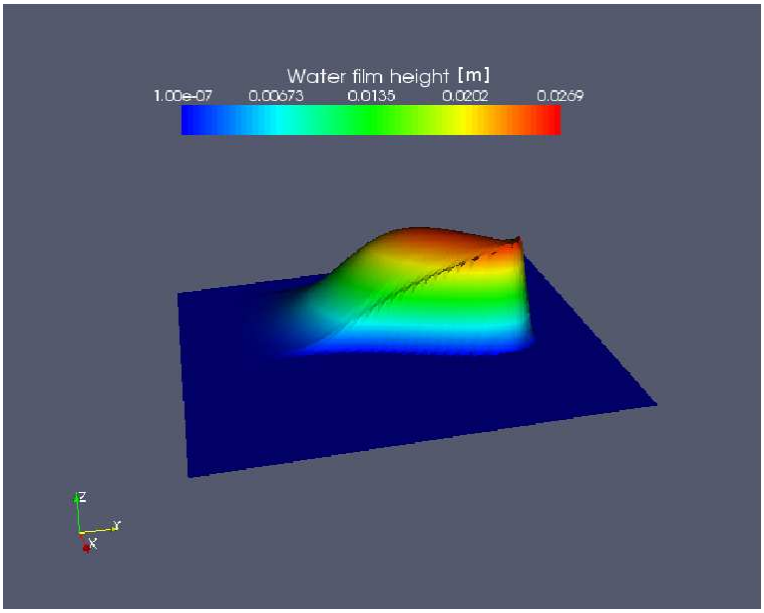

Figure 3.21: Water film on an horizontal plate at $t = 2.1s$

As time goes on, see Figure 3.21, the film evolves into its pseudo steady state. The

main part of the bulk reaches an equilibrium height whereas the front is fully formed and continue to advance on the surface. The shape of the interface between liquid and surface is similar than in 2D and produces a bump or peak. Only in 3D we can see that the maximum height of this peak is decreasing towards the side of the bulk. This is due to the initial condition being a gaussian shape. The mass of water on the side of the bulk is less than in the centre and will produce smaller peaks.

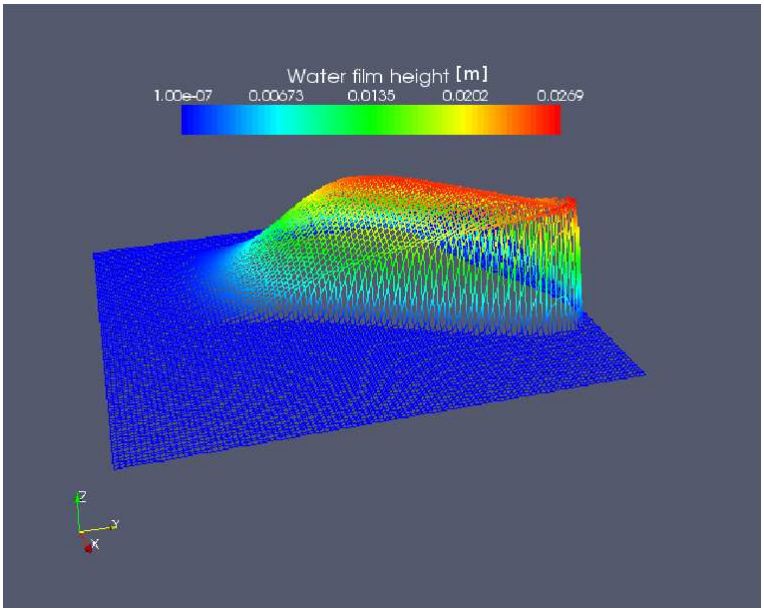

Figure 3.22: Water film on an horizontal plate at $t = 3.4s$

In Figure 3.22, the liquid reaches the other end of the domain. The water film height is projected on the mesh. By looking at a single line of the mesh at the interface we can see the shape of the front similar to the two dimensional case.

Next we change the inclination of the plate, negative and positive angle, we also present some rotating cases.

3.5.1 Flow down an inclined plate

With a negative angle, $\alpha = -10°$, the gravity acts in the same direction than the shear stress. The resulting behavior of the water film under such conditions is not very different than on the horizontal plate. The same initial condition is applied. A time unit is 0.1 second.

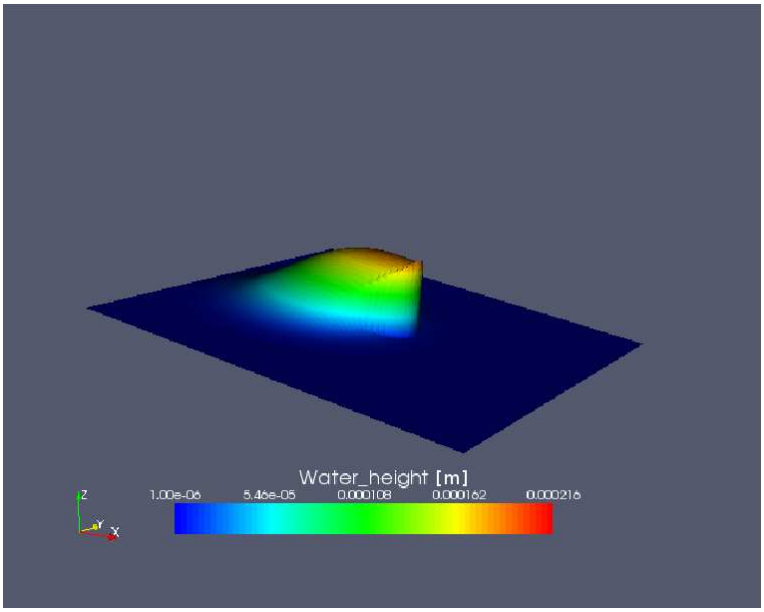

Figure 3.23: Water film on an inclined plate, $\alpha = 10°$ at $t = 0.2$

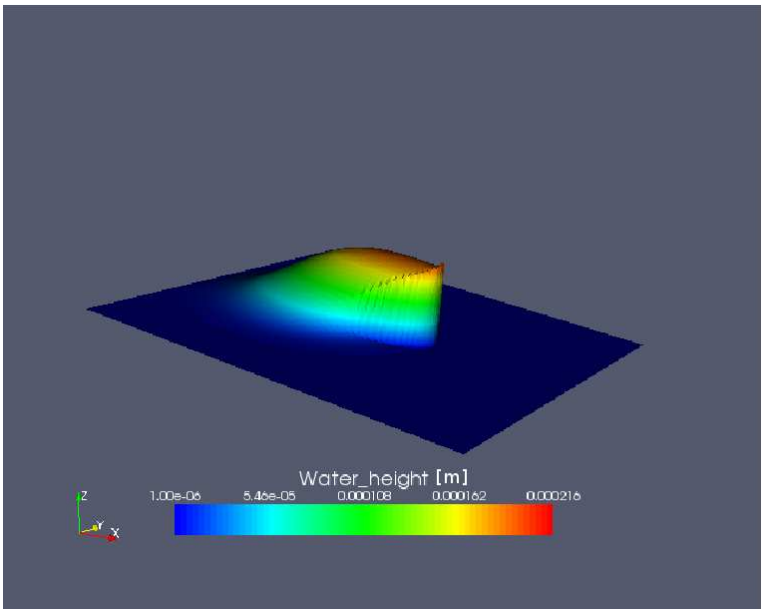

Figure 3.24: Water film on an inclined plate, $\alpha = -10°$ at $t = 0.3$

We can observe in Figure 3.24 that in the first moment of the initial gaussian shape is pushed by shear and gravity forces toward the bottom of the plate.

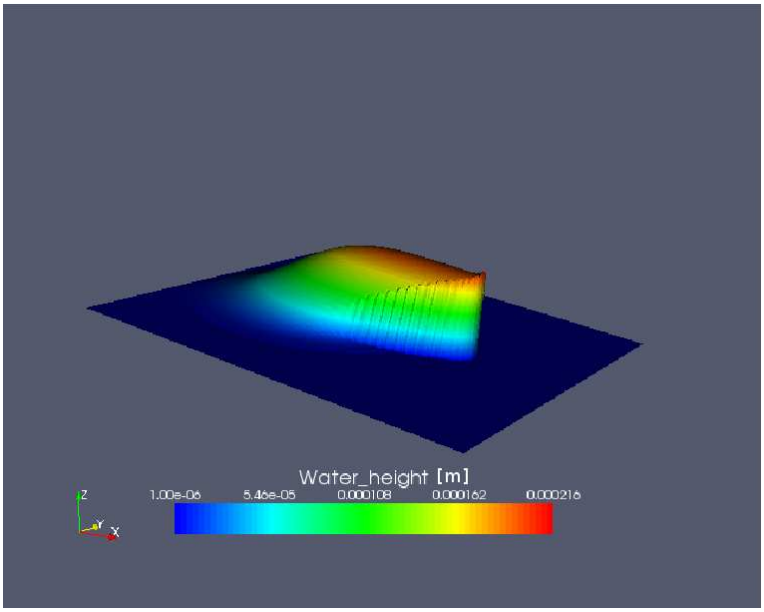

Figure 3.25: Water film on an inclined plate, $\alpha = -10°$ at $t = 0.5s$

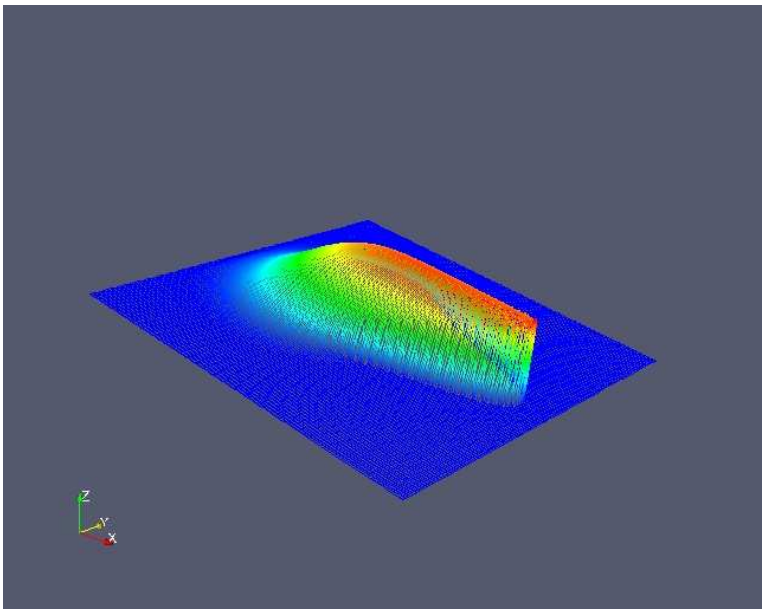

Figure 3.26: Water film on an inclined plate, $\alpha = -10°$ at $t = 0.8s$

As the water flows down the surface, the main part of the film reaches an equilibrium height, see Figure 3.26. This equilibrium height is slightly less than in the horizontal case. As the gravity and shear act together the resulting speed of the flow is higher and the mass of water spreads more rapidly over the domain. One can argue as well that the interface between the liquid and the surface is a bit less sharp on the side of the bulk. This is probably because gravity exerts less pressure in the normal direction of the surface.

Positive angle

When the angle is positive and the shear stress still acts in the x-direction, the gravity force is now in opposition to the shear stress. On the following calculation the flat plate has been given an angle of 20° with the horizontal increasing substantially the gravity force in the x-direction. The initial condition or incoming water is applied in a gaussian shape at the bottom of the plate. At first, the shear stress is dominant and pushes the bulk towards the top of the plate forming the now usual front shape. But as the water

mass is increasing at the bottom of the plate , see Figures 3.27 and 3.28, the lower part of the bulk is slowly driven towards the bottom of the plate. Note that for the remaining of this chapter the water film height is represented in meters in the figures.

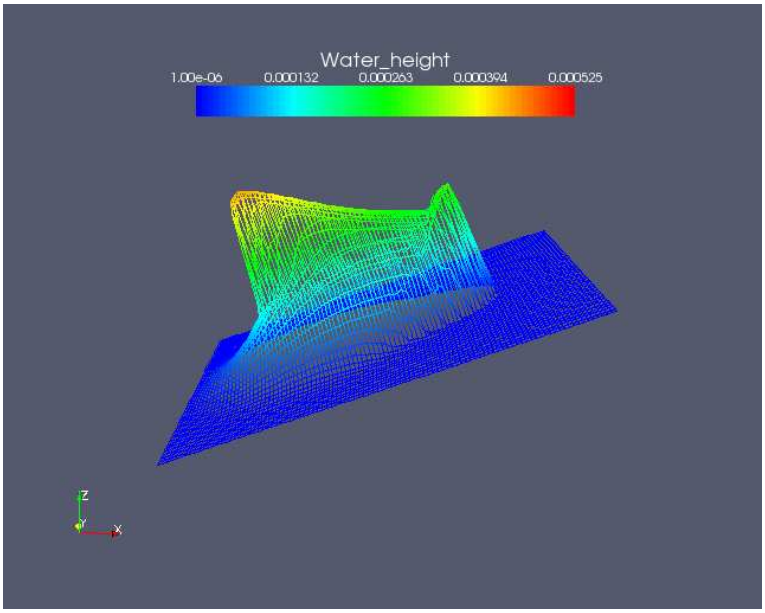

Figure 3.27: Water film on an inclined plate, $\alpha = 20°$ at $t = 0.6s$

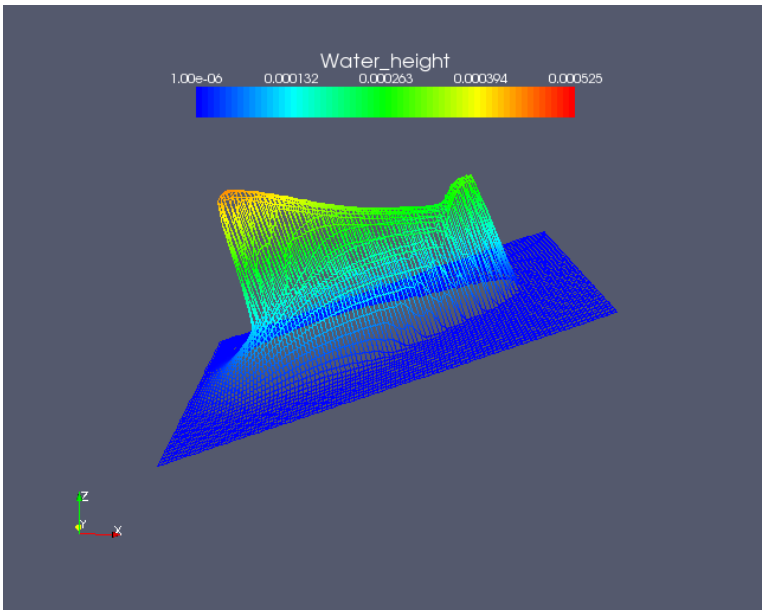

Figure 3.28: Water film on an inclined plate, $\alpha = 20°$ at $t = 0.8s$

As more time elapses, the undercompressive shock disappears, as observed before in 2D, and a plateau appears between the two bulks, see Figures 3.29 and 3.30.

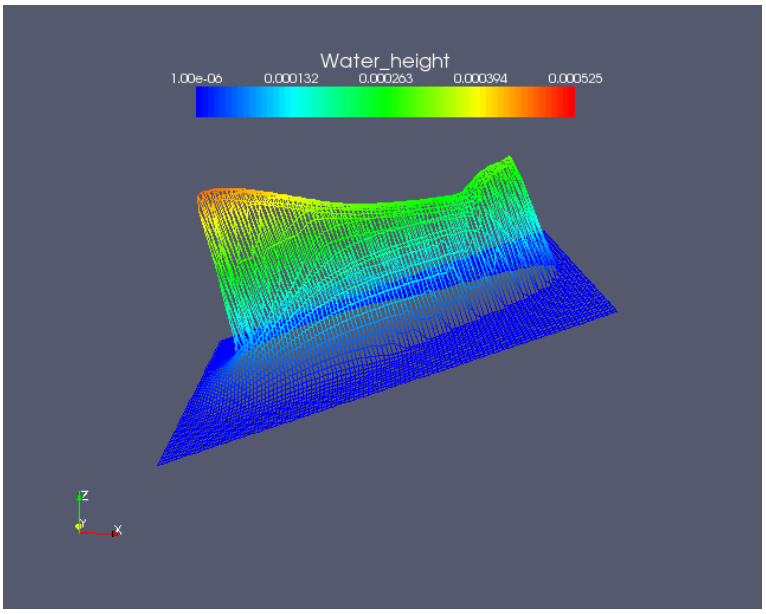

Figure 3.29: Water film on an inclined plate, $\alpha = 20°$ at $t = 1.2s$

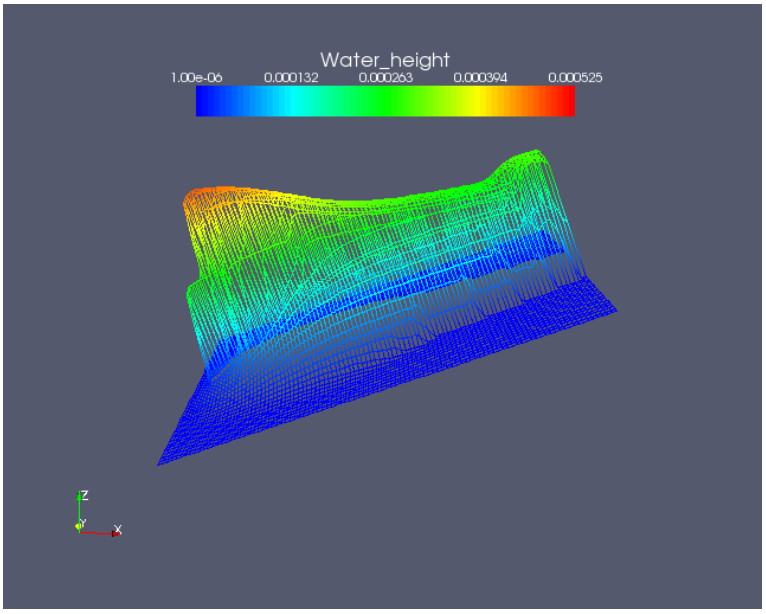

Figure 3.30: Water film on an inclined plate, $\alpha = 20°$ at $t = 1.8s$

Again in 3D we can observe the full structure of the film. As the initial conditions

are in a 3D gaussian shape, the liquid on the side of the bulk does not reach the critical height where gravity and pressure forces take over shear stress [1]. By following closely a mesh line on the side of the bulk in Figure (3.30), we can see that the undercompressive shock has not appeared here and the liquid continues to flow towards the top of the plate. A double shock structure can be observed at the front.

3.5.2 Rotational flow

We now present some simulations of water spreading over a rotating surface. This type of simulations is useful to spin coating applications or icing on a rotor of an helicopter for example. A simple upwind scheme would be unable to perform well due to the endless change in the direction of discretisation and a classic central scheme would be unstable. The high resolution methods developed in this work allow us to perform such calculation. A simple test case is used to illustrate the spreading of liquid on a rotating surface. The source of water is imposed in a rectangular shape centred in the middle of the plate. The axis of rotation is in the vertical direction also centred in the middle of the plate. So that under centripetal forces the liquid will be pushed from the centre of the domain towards the edges.

At first the water piles up in the middle of the domain as the outward flow is not strong enough to spread the liquid, see Figure 3.31. Then the liquid starts to move towards the edges. Note that the centripetal force gets stronger away from the centre, which explains the four fingers observed in Figure 3.32 corresponding to the four corners of the initial source.

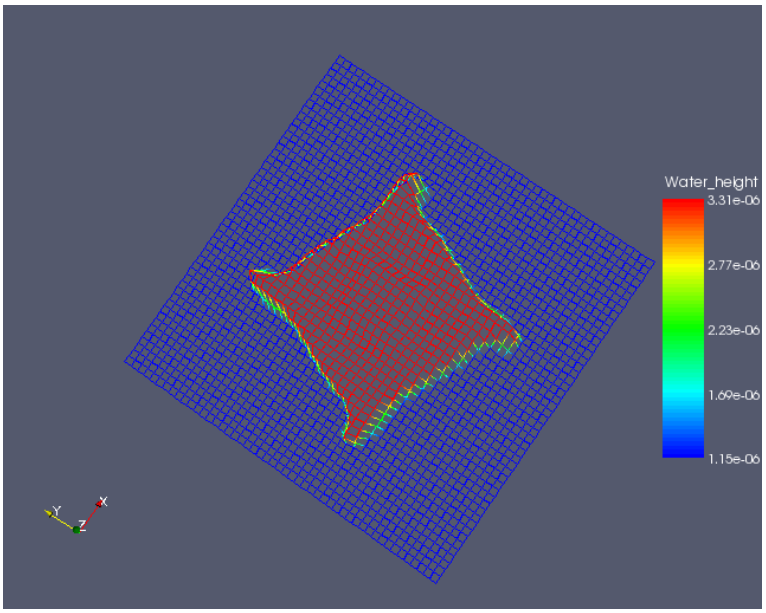

Figure 3.31: Water film on a rotating plate at $t = 4s$

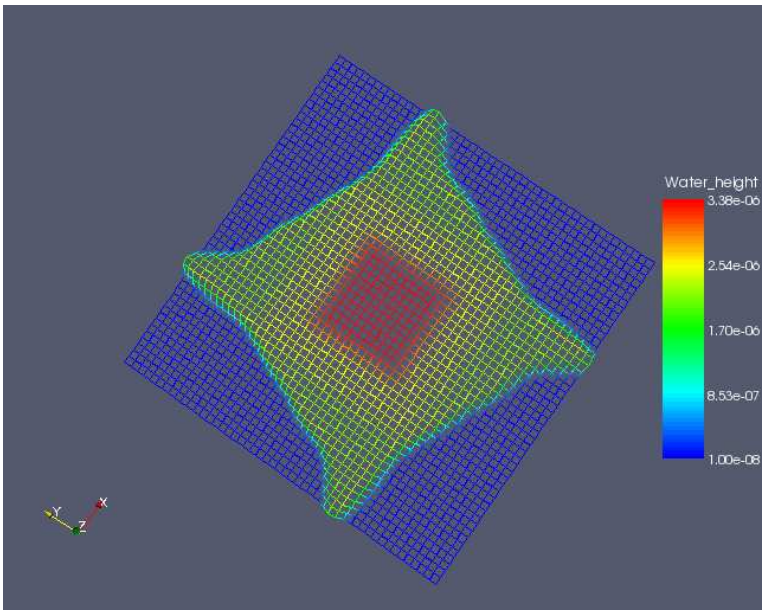

Figure 3.32: Water film on a rotating plate at $t = 8s$

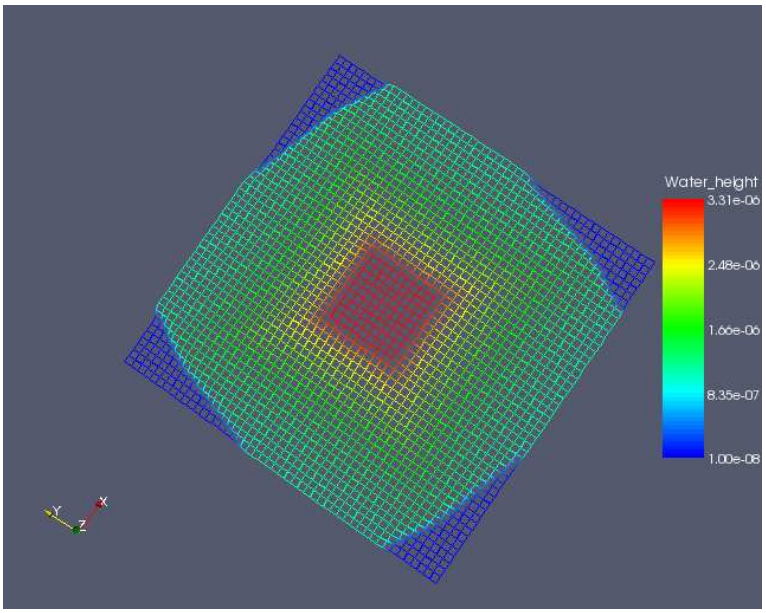

Figure 3.33: Water film on a rotating plate at $t = 12s$

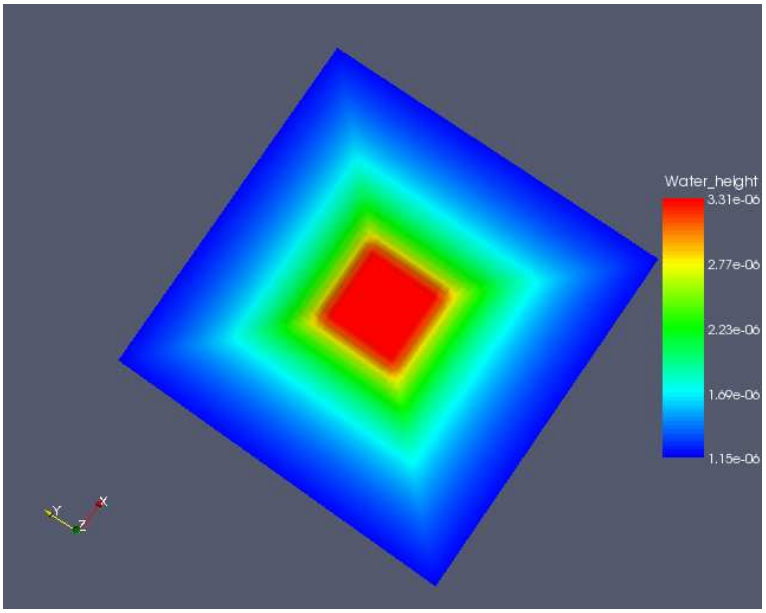

Figure 3.34: Water film on a rotating plate at $t = 20s$

Finally the liquid spreads over the entire domain , Figures 3.33 and 3.34. As all the surface is covered by the liquid we can see, Figure 3.34, that the film thickness decreases towards the edges. Qualitatively, these results compare well with those obtained in [76].

3.5.3 Surface tension effect

We now repeat the first test with the shear stress acting across an horizontal plate. Only this time the surface tension force has been artificially increased. The inverse capillary number in Equation 3.4 is magnified by a factor of ten.

The same initial conditions are applied and at first the bulk, in a gaussian shape, is pushed forward by the shear stress, see Figure 3.35. As the interface between liquid and substrate becomes sharper, the surface tension force increases. The shape of the peak is much smoother than with water (see Figure 3.36 compared to 3.19). This is due to the surface tension.

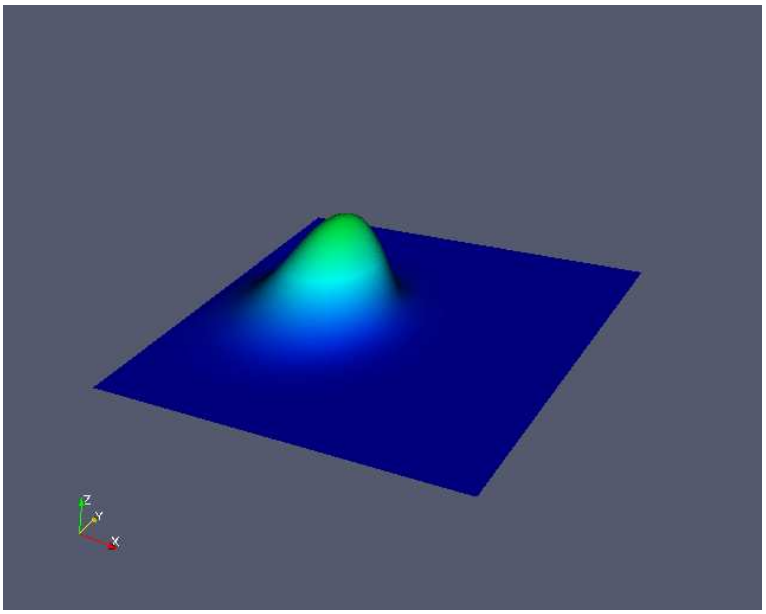

Figure 3.35: Structure of a film with high surface tension at $t = 0.2s$

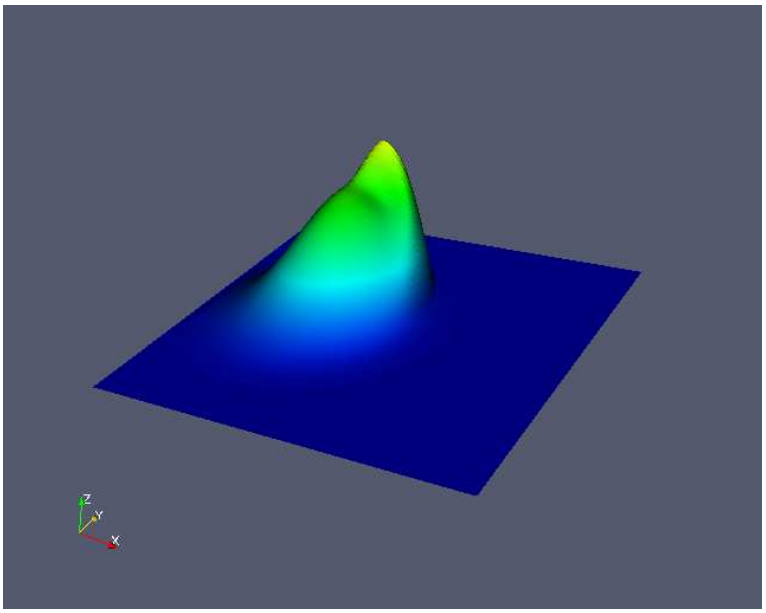

Figure 3.36: Structure of a film with high surface tension at $t = 1s$

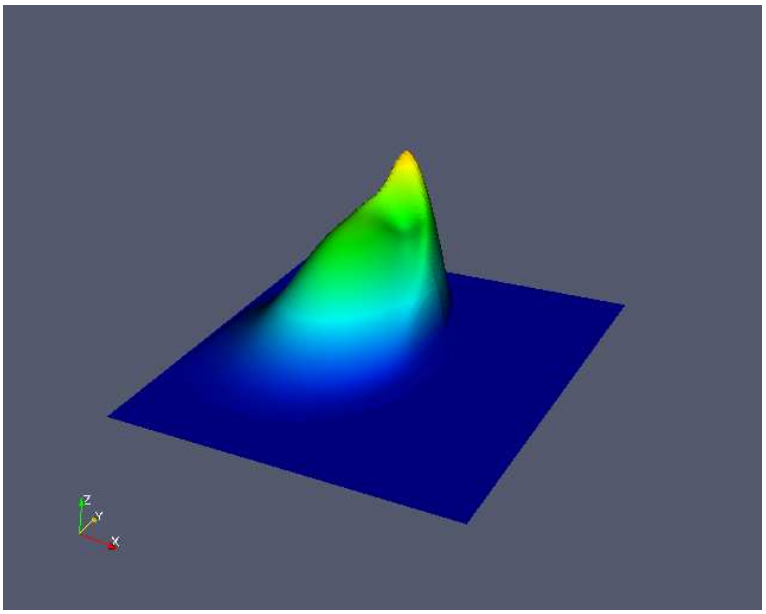

Figure 3.37: Structure of a film with high surface tension at $t = 2s$

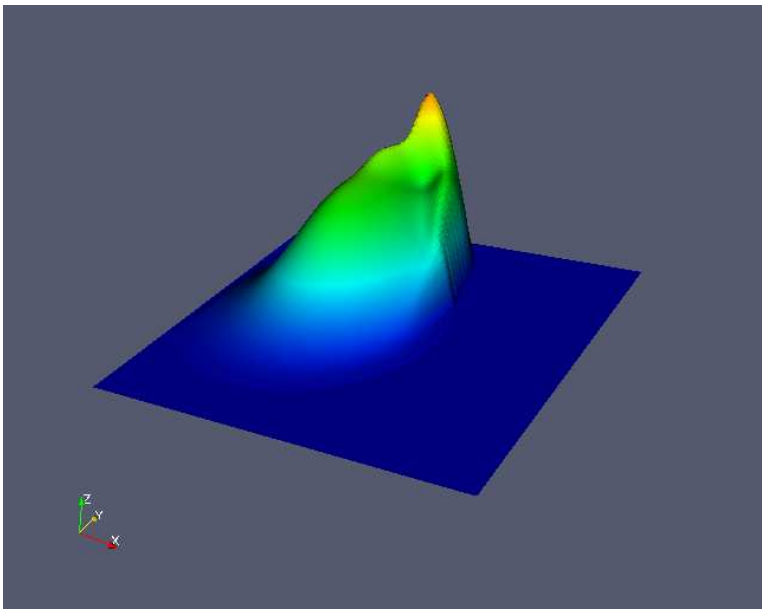

Figure 3.38: Structure of a film with high surface tension at $t = 2.8s$

As the flow spreads over the surface we can observe the effect of wind stress on the film in Figure 3.38. The wind blowing sideways creates a hole in the plateau while the surface tension maintains the position of the peak formed on the side.
This test case illustrate how the surface tension affects the shape of the front. Presence of surfactant, anti-icing chemical or even the curvature of the substrate will affect the surface tension. We will show in the next chapter how important is the resolution to resolve correctly the surface tension effect.

3.6 Conclusion

In this chapter we have presented the numerical scheme developed in ICECREMO2. This scheme belongs in the high resolution methods and combines a first-order upwind scheme with a second-order Lax-Wendroff coupled with the superbee limiter in order to keep the entire method stable. The final scheme is a shock capturing method and is able to solve the thin film equation accurately. However the implementation of the limiter for

unstructured meshes is not trivial and requires to evaluate fluxes in a virtual neighbouring cell.

The validation of this scheme has been performed on idealized test cases, flat plate, under various conditions, in two and three dimensions. The shape of the water film obtained is confirmed with what has been observed or simulated in [1] for example. This scheme is also very robust and because it uses mainly a central discretisation for the entire flux, we have been able to perform simulations on rotating components. The results again agree with those observed before.

We also highlighted the surface tension effect on the front shape. In the next chapter we will demonstrate how important is resolution to solve accurately the interface between water and substrate. We will use the inherent dual discretisation of the scheme to define an error indicator and an adaptive mesh refinement method.

Chapter 4

Error Control And Adaptivity

4.1 Introduction

All numerical methods based on discrete approximations are by nature highly dependent on the level of resolution. Finite differences, finite volumes and finite elements methods all share the same aspect: under different assumptions, the numerical solution converges to the exact solution as the resolution is increased (i.e.: $\Delta x \rightarrow 0$). Despite the continuing progress in computer power, the complexity of the problems to solve also increase and the question of how to solve a problem with a minimum resource is more than ever relevant. Unstructured grids are powerful to discretize complex domains. They are also the only reliable option for adaptivity where different levels of resolution are used on different regions of the domain. Indeed, by refining locally, adaptivity offers the possibility to resolve an equation accurately without the fine global resolution that structured grid would have required.

There are different sorts of adaptivity. The r-adaptivity, so named in the finite elements method, consists in re-meshing or moving the grid points in order to equidistribute a given error all over the grid.

The h-adaptivity or mesh enrichment refines the grid locally by adding more grid points and cells to the domain. Only this last method is considered in this work.
The first step is then to define where to refine. An error indicator or error estimator must be derived for the equation. Such error measures are usually difficult to obtain and depend on the physical quantity of interest one wants to solve with the highest accuracy. For example, in icing computations, two choices are already possible. One might want to define the error measure as a function of the water film or ice height.
Once the error measure is defined, a typical refinement procedure may be described as follow:

1. Compute the solution on an initial grid
2. Perform an error estimation returning which part of the grid as to be refined.
3. Refine the grid and interpolate data from coarse to fine grid (these last two steps can be performed until the error is below a given threshold for example)
4. If necessary coarsen the region where current resolution is not needed and interpolate data from fine to coarse grid.

4.1.1 Different sources of error

The numerical computation of wet/dry bed fronts is very difficult and there are several sources of error to be considered. Note that we will not deal with all these errors in this work but nonetheless it is worth to mention it in our quest for the ideal numerical method.

Precursor film:

A popular way of dealing with the wet/dry front problem is by *artificially wetting the dry bed*(see [35]). Setting the minimum water height to a small positive value $h_p = \epsilon > 0$

is mathematically equivalent to specifying a contact angle at the water front, but is computationally simpler. This very thin film is called the **precursor film**. Toro presents in [35] a parametric study showing the importance of the precursor film height on the speed of the dry front. He also shows that very small variations of the precursor height lead to large variations in the predicted speed of front. In most of the test cases presented in this thesis, the precursor height has been chosen significantly small ($h_p = 1\ \mu m = 10^{-6}\ m$).

Conservation induced error

This type of error, so named in [35], comes from the way the velocity is computed in conservative methods. Recall the definition of the wave speed made in the previous chapter (Equation (3.12)):

$$A_{i+1/2} = \begin{cases} (Q^k_{i+1} - Q^k_i)/(h^k_{i+1} - h^k_i) & \text{if } \ h^k_{i+1} - h^k_i \neq 0\ , \\ \partial Q^k/\partial h\Big|_{i+1/2} & \text{if } \ h^k_{i+1} - h^k_i = 0\ , \end{cases}$$

Although we avoid dividing by zero, the way we do that is by introducing another small constant, $\epsilon 2 > 0$, and considering two different cases whether $|h^k_{i+1} - h^k_i|$ is greater or smaller than $\epsilon 2$. This can introduce more errors. Also near wet/dry front both numerator and denominator are small. This can also combine with error from the artificial bed wetting depicted above as the two constant $\epsilon 2$, the minimum tolerate of $|h^k_{i+1} - h^k_i|$, and the precursor height are clearly linked.

Sonic point and stagnation line

Another place where the wave speed can get very small is around the stagnation line. These are also called sonic lines, or sonic points in 1D, they represent a change in the direction of the flow. Around these points two sorts of error can occur. This is because of the very low amplitude of the wave speed, as depicted above, but also because of its

change of direction. We already explained in the previous chapter how an upwind scheme could failed to converge at these points because of a constant change of discretization (see also [41]). A central scheme like the one proposed in this thesis permits to overcome this second problem, but caution must still be taken.

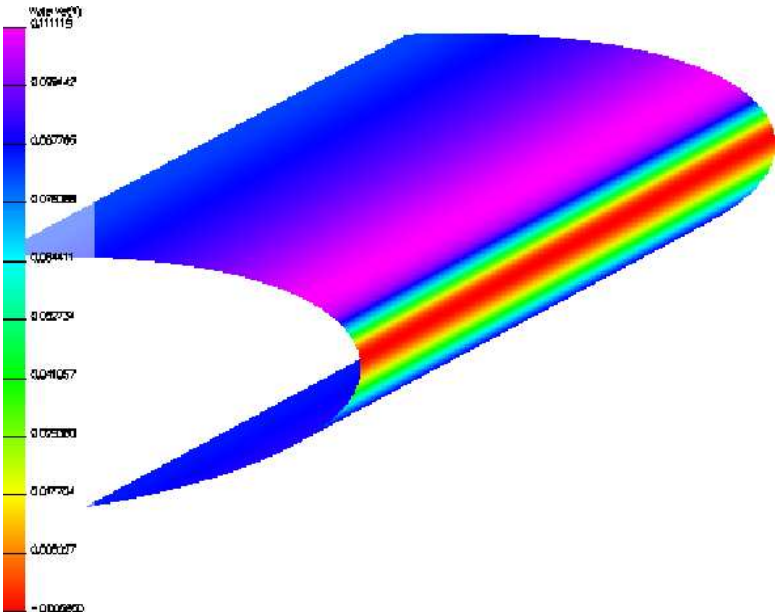

Figure 4.1: Wave speed on a NACA0012 airfoil

The Figure 4.1 represents the horizontal value of the wave speed in the c17 test case [28]. The red part is the stagnation region where the flow separates.

4.1.2 Truncation error

Finally, truncation error is the sort of error that adaptivity aims to reduce. This error comes from the discretization itself. Directly dependent on the type of scheme used and the level of resolution, this is the main error of approximation that all numerical algorithm try to keep within reasonable bounds, trying to find a good compromise between the computational resources required and the quality of the solution. Truncation error is both spatial and temporal as we can consider a time-based grid as well as a spatial one.

However, we have seen in the previous chapter how the time step and the space step where linked by the CFL number and the stability condition. The local truncation error is the error introduced in a single time step. Showing that this error is small and stays bounded (the method is stable) can be used to prove convergence. In linear theory this is the Lax equivalence theorem. The global truncation error of a finite difference or finite volume leads to its order of accuracy. The scheme presented in the previous chapter is first-order in time and first to second-order accurate in space depending or not of the presence of a discontinuity. This is sometimes called the **clipping error**. Osher and Chakravarthy [40] proved that TVD methods must degenerate to first order near extrema. The explanation has already been given in Chapter 2 and 3: to keep the scheme globally stable, the limiter is zero near a discontinuity, which reduces locally the method to a first-order upwind scheme.

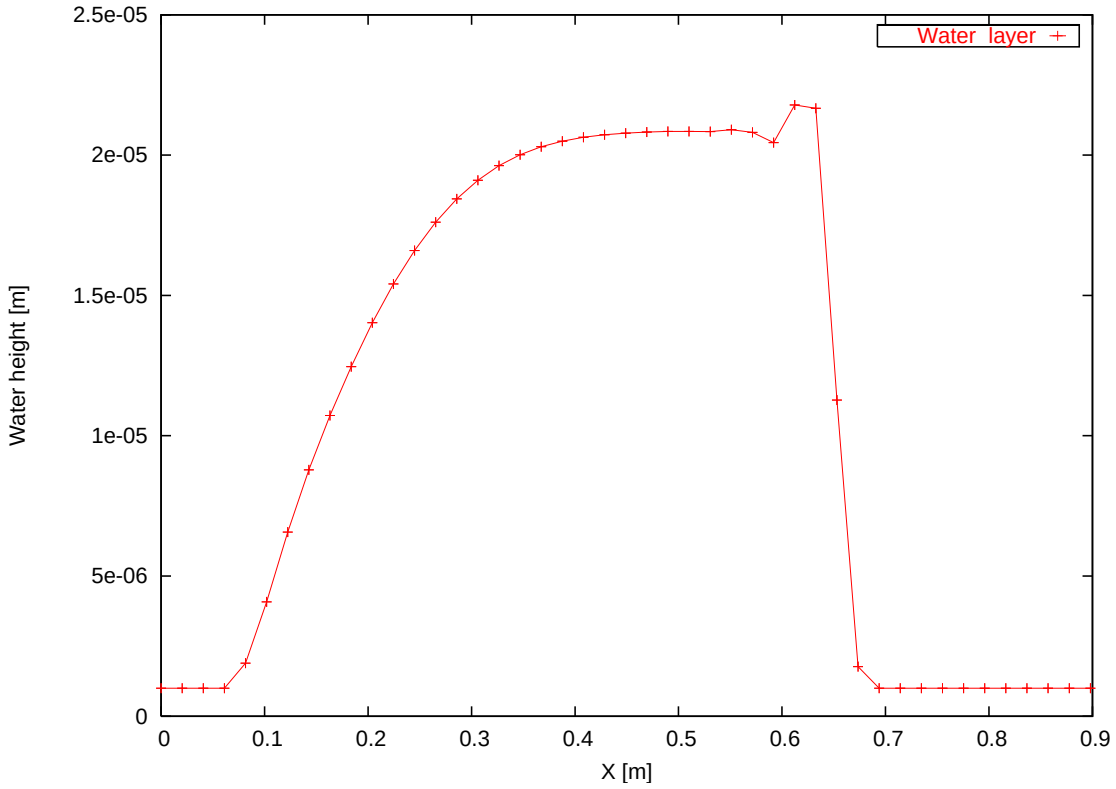

Figure 4.2: Water advancing on a plate on a 50 cells grid (1D)

In Figure 4.2 we can see how the scheme behaves near maxima on a coarse grid. The peak seems to have been cut off. Again, this is due to the change of discretization of high resolution methods near extrema.

4.2 Error estimation and Double discretization

4.2.1 Global refinement

Before defining an error estimator for adaptivity, it is important to know what is the effect of refinement on the numerical solution. A simple quantitative analysis usually gives very interesting results. On a one dimensional test case, we compare results obtained on grids of different resolution. The first grid contains 50 cells which corresponds to a space step of $\Delta x = 0.02m$. The second grid contains twice as many cells, this corresponds to a space step reduced by half $\Delta x = 0.01m$. Comparing the results obtained on the coarse and fine grid gives us valuable information on how the numerical solution reacts to grid refinement.

Figure 4.3 represents the numerical solution obtained with an upwind scheme on a coarse (green) and a fine grid (red). Differences between the two solutions can be noticed in two regions. The most obvious being at the front of the flow. The upwind scheme being very diffusive does not catch the front properly, but we can observe as the grid is refined that the front becomes sharper. The second part where a difference may be seen is in the flow development region as depicted in Figure 3.1. Again as the resolution is increased, the solution becomes sharper.

Finally and probably as important as the two other remarks, the steady state region is unaffected by the refinement. As the flow progresses on the surface, the water reaches an equilibrium height. The solution being constant, there is no benefits in increasing the resolution in this region.

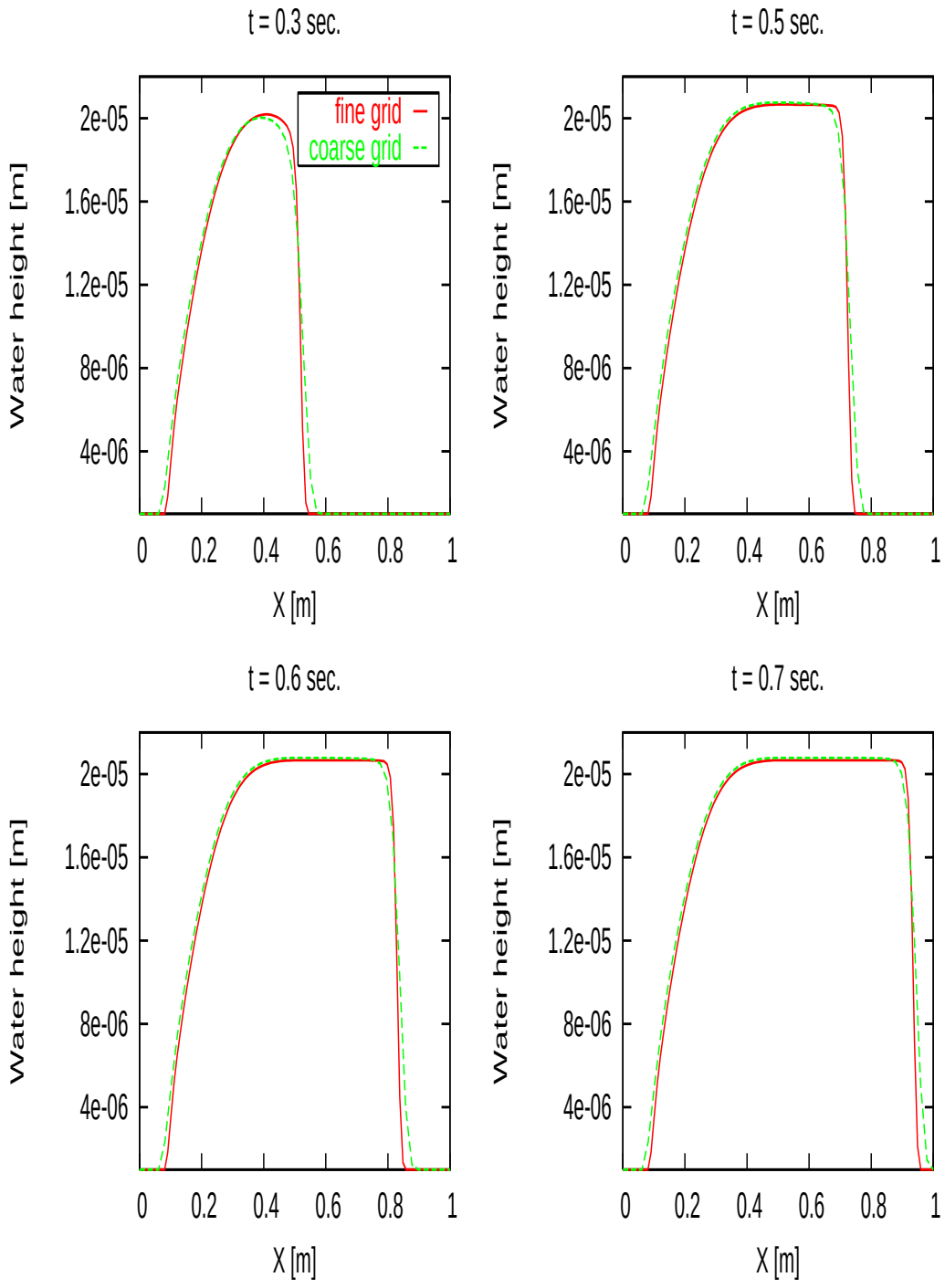

Figure 4.3: Effect of refinement with upwind scheme

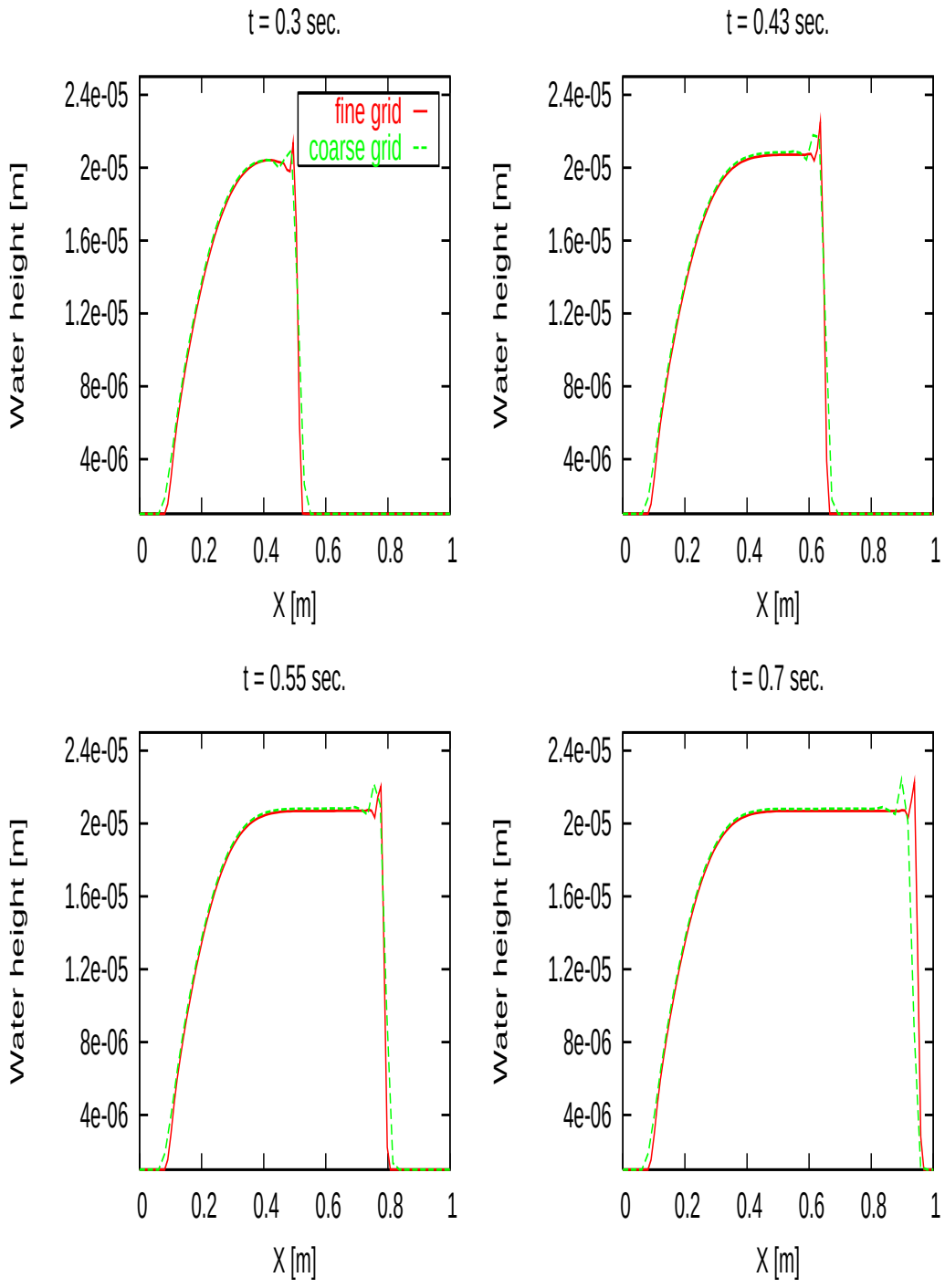

Figure 4.4: Effect of refinement with high resolution method

The same calculation is reproduced using the high resolution method developed in the

previous chapter. We can see the results in Figure 4.4. As with the upwind scheme, the flow development region and the front are affected by the grid refinement. We can notice that the global shape of the front is not changed, only its width varies, the maximum height stays the same. Again, the solution on the fine grid is much sharper.

Owing to this simple experiment, we have been able to pinpoint the part of the grid which would benefit of an increase in resolution. The flow development region, which represents the part where the incoming water enters the domain, stays fixed for the entire calculation. The front part is the most problematic as it constantly moves as the water advances on the domain. Ideally we would then like to refine the grid only at these two regions while leaving coarse the part where the liquid reached its equilibrium height. It is imperative to define an error indicator which will have high value in the two regions of interest and low values in the equilibrium part.

Resolution for surface tension

The increase of resolution does not only bring more accuracy in the sense of truncation error. The surface tension term in Flux 3.4 include a third-order derivative. To compute such term in ICECREMO2, we first define the curvature of the water film on which we calculate the gradient. Seeing the structure of the water film in the previous figures we can foresee that the surface tension will be more important at the interface between substrate and liquid where the curvature is higher. It is therefore necessary to have several grid points at the front to be able to compute the curvature correctly. However the feature at the front is of much smaller length that the rest of the film. And resolving the entire domain with high resolution would require too much computing ressources.

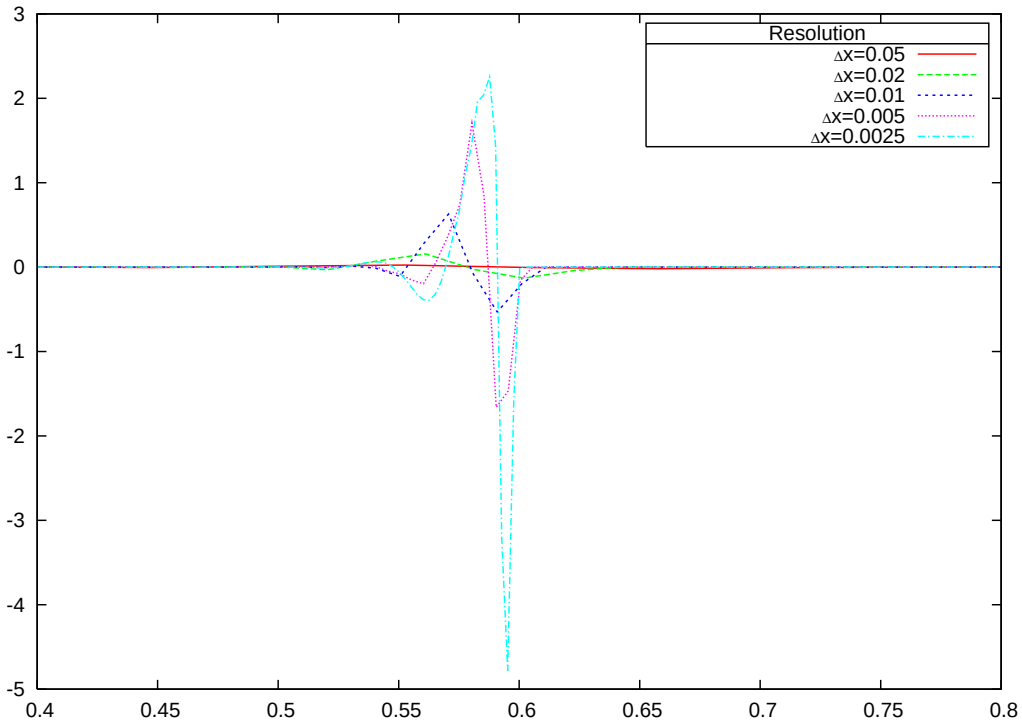

Figure 4.5: Evolution of curvature with the resolution

Figure 4.5 represents the curvature at the interface between substrate and liquid. With the same physical parameters for all calculations, only the resolution is varying. We can see that the curvature of the liquid film increases with the resolution. At low resolution the peak at the front is not resolved and the curvature is almost null. Only with high resolution, the value starts to converge. It would be possible to develop a sub-grid scale model in order to simulate the surface tension effect on a coarse grid. In practice and for the flat plate case only, where the curvature of the substrate is null, we can increase the surface tension coefficient. Only the front region is affected as in the other parts the curvature is either null or significantly smaller.

4.2.2 Double discretization

To define our error estimator we use the property of the numerical scheme employed to solve the equation. We recall that our high resolution method is a combination of a second-order Lax-Wendroff scheme and a first-order upwind scheme. Furthermore, near high gradient or discontinuity the scheme switches to first-order to stay TVD and for global stability purposes.

We also recall the finite volume formulation of the scheme: at each cell interface or edge the flux through this edge is evaluated with:

$$Q_e = (1 - \phi(r))Q_e^{UP} + \phi(r)Q_e^{LAX} \tag{4.1}$$

where Q^{UP} and Q^{LAX} represent the upwind and Lax-Wendroff contribution respectively. We define the error estimator as the difference between the second and first-order discretization:

$$\epsilon_e = \left|Q_e^{LAX} - Q_e^{UP}\right| \tag{4.2}$$

If we consider the case where the wave speed is positive, we have in fact:

$$\epsilon_e = |\frac{1}{2}(Q_r + Q_l) - \frac{\Delta t}{2\Delta x}A_e^2(h_r - h_l) - Q_l| \tag{4.3}$$

With the notation of the previous chapter where the subscripts r and l represent the evaluation at the center of the right, and left cell respectively. It is difficult to obtain a general analytic form for this term but if we recall the definition of the wave speed we have:

$$\epsilon_e = |\frac{1}{2}(Q_r - Q_l)(1 - \frac{\Delta t}{\Delta x} A_e)| \tag{4.4}$$

Note that the fluxes Q in all the notation above are vectors so when we evaluate the difference of two fluxes, we actually compute the difference of the scalar product of these fluxes with the edge normal $\overrightarrow{n}_e$.

By simplifying the notation in (4.4), we can interpret the error estimator ϵ_e as being the change of flux through the edge weighted by the wave speed.

Although the Lax-Wendroff is not an adequate scheme for the computation of the solution as it exhibits high level of dispersion which can lead to instability, it is perfectly justified to use it as a higher order method for the error estimation. Used in the global scheme, the dispersion of the Law-Wendroff scheme would yield to oscillations of the numerical solution as the error is forwarded after each time step. Here the scheme is only used locally, between each time step, and not for the solution itself but for the error indicator. No contribution is made to the global solution over time hence the stability of the global numerical scheme stays unaffected.

A second error indicator has been implemented, taking this time the difference of discretization between our high resolution method and a fully second-order Lax-Wendroff scheme. Recalling the discretization of the limited scheme (4.1) we computed:

$$\begin{aligned} \epsilon_e^* &= \left| Q_e - Q_e^{LAX} \right| \\ &= \left| Q_e^{UP} - Q_e^{LAX} + \phi(r) \left(Q_e^{LAX} - Q_e^{UP} \right) \right| \end{aligned} \tag{4.5}$$

Which is a similar formulation as (4.4) with the introduction of the limiter $\phi(r)$. We

expect this error estimator to be zero when $\phi(r) = 1$ and equal to ϵ when $\phi(r) = 0$. Figure 4.6 represents these two error estimators together with the corresponding flow solution.

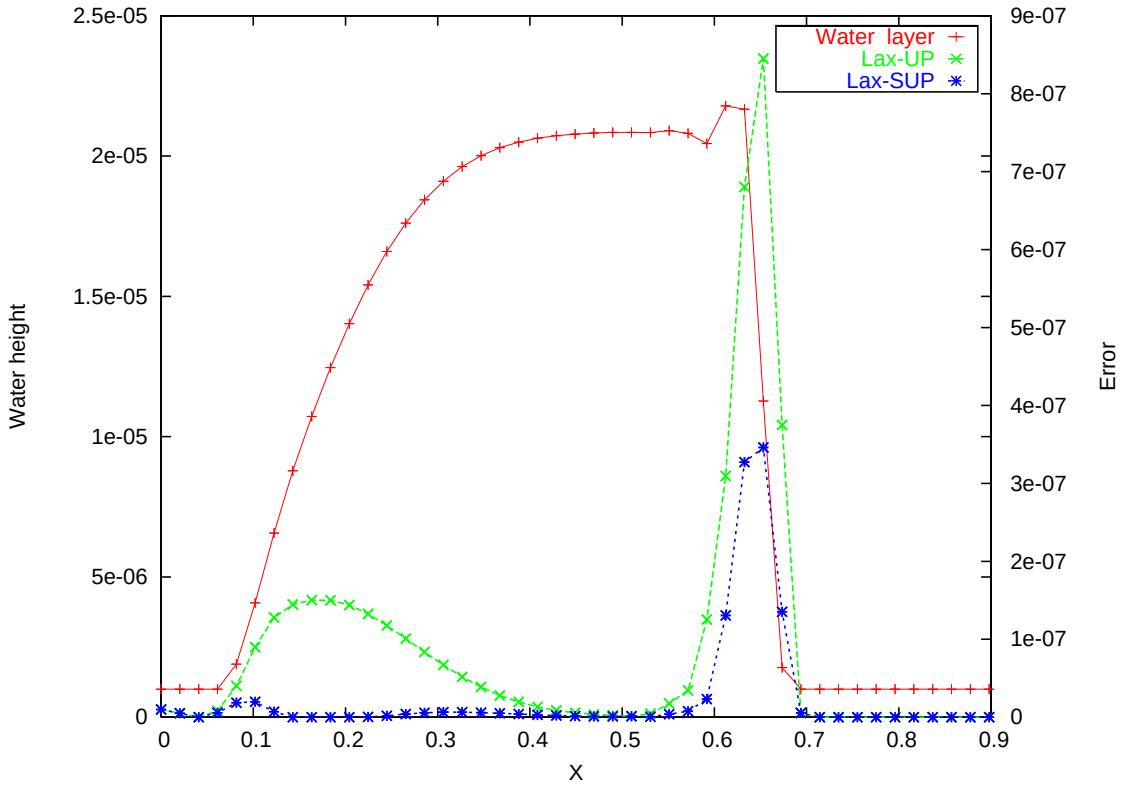

Figure 4.6: Error indicators and water film

Figure 4.6 shows the water film in its advanced phase when the shock at the front is already formed. On the right axis the two error estimators described above are plotted at the exact same time than the water film. We can therefore observe the distribution of the error as the water film progresses on the surface. Although the error estimators are computed at each cell interface or edge, the values plotted here are cell centered. The value on each cell is determined by the sum of the error over the edges.

We can see that both estimators exhibit the same properties. The maximum error is at the front of the flow. A small bump in the flow development region indicates that accuracy can be gained in this region as well. Finally very small differences are noticeable in the

steady state region.

The difference between the two error estimators is also very clear. The double discretization using the Lax-Wendroff and the upwind scheme gives much higher values for the error estimator. However, this is not this particularity which will guide our final choice but rather the fact that this error estimator also shows error in a wider region around the front. This will prove to be very useful in the following work as it will allow us to refine a larger part of the grid around the front.

The second error estimator (4.5) however gives us valuable information about the scheme we use to solve the equation.

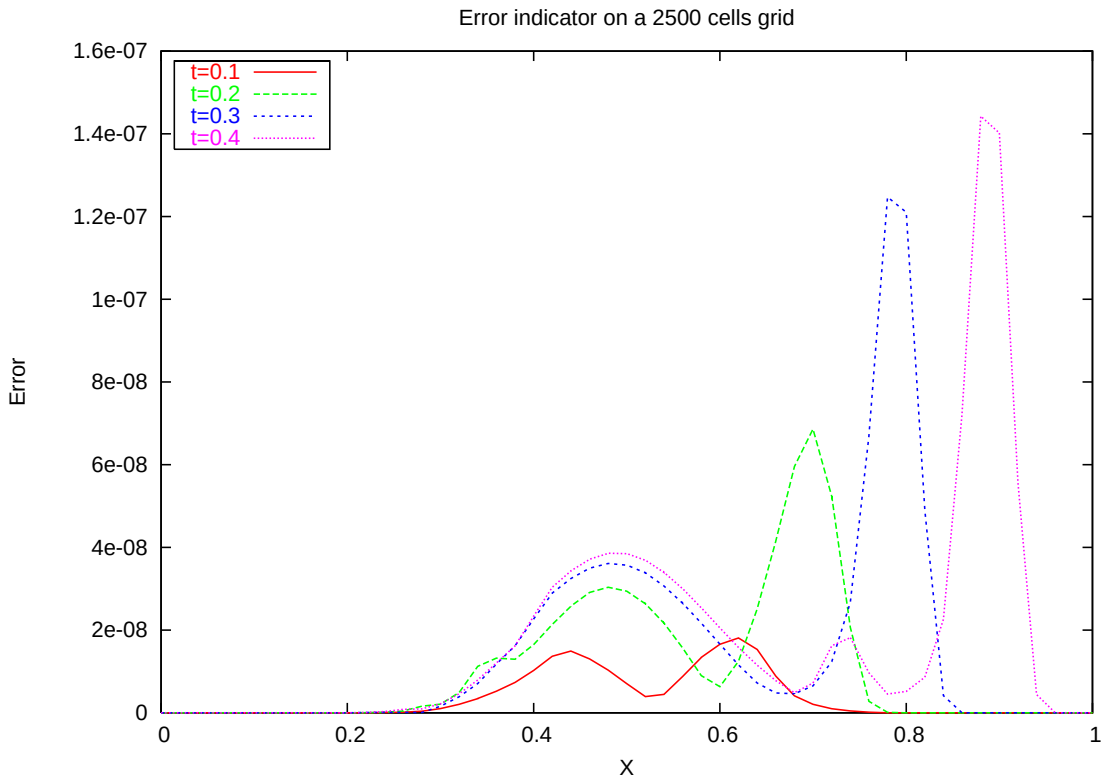

Figure 4.7: Error indicator on a 50x50 cells grid

Figures 4.7 and 4.8 represent the difference between the high resolution method and a fully second-order Lax-Wendroff scheme on 2D grids. Again we can observe the action

of the limiter as the flow progresses on the grid. The region with high error values are those where the flux limiter $\phi(r)$ is not equal to 1, where the global scheme switches to the first-order upwind. Looking at this error on grids with different level of resolution will give us an idea of the global order of accuracy of our scheme. We can see in Figure 4.8 that the error is reduced by 4, compared to Figure 4.7, everywhere except at the front where it is reduced by almost two. This confirms that the high resolution method we use in this work is second-order accurate except near a discontinuity where it is first-order only.

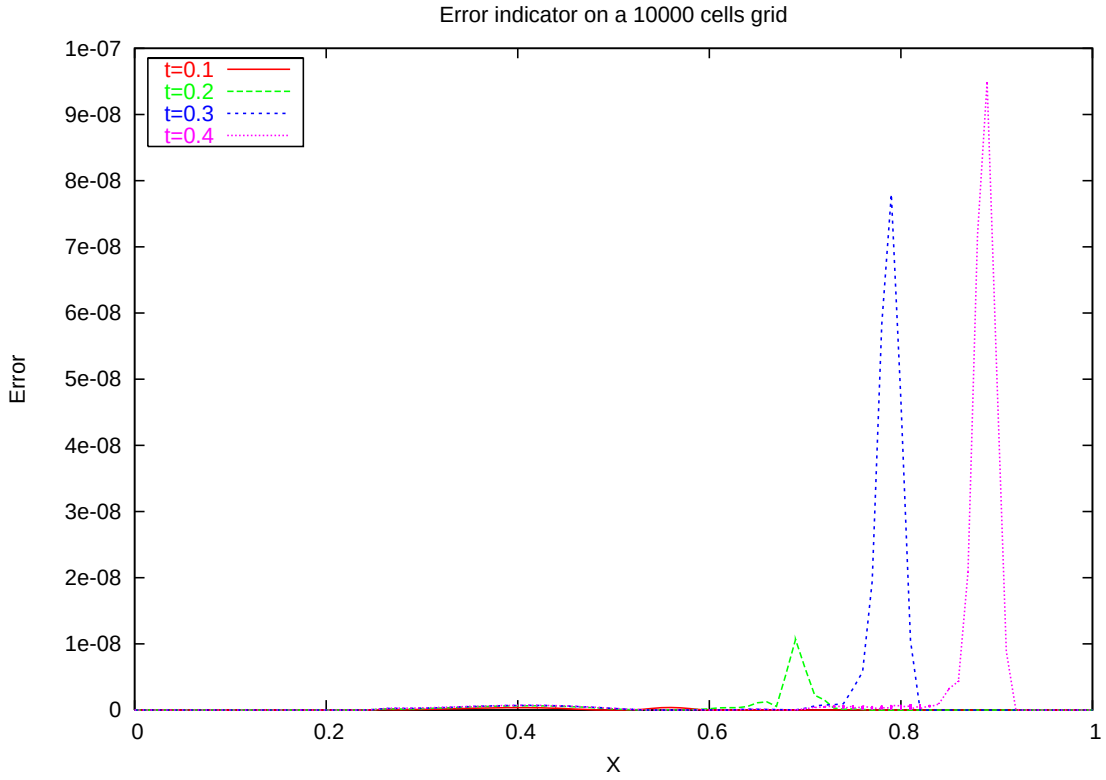

Figure 4.8: Error indicator on a 100x100 cells grid

In this section we have shown with a simple qualitative study the effect of the grid resolution on the solution. As the grid is refined, the solution is improved in two main regions. The first one is static and is the region of incoming flux or flow development, the

second where the benefits of a high definition is the most obvious is the front region and varies with time. An ideal adaptive method for this type of flow will then keep this two regions very fine whilst leaving the rest of the grid at lower resolution.
Using double discretization, we have then derived an error estimator which has a high error value in the regions where refinement is required. This error estimator catches the front perfectly. Furthermore it uses directly the properties of the numerical scheme used in the solver and does not require any additional computation. It has also the nice property to be computed at each edge which will prove to be rather useful for the refinement technique detailed next section.

4.3 Adaptivity in ICECREMO2

The two main advantages of the unstructured meshes are the possibility to treat and discretize accurately very complex geometries as well as optimizing the grid for the numerical solution.

Grid generation has become a field of its own and many different techniques can be used. The advancing front technique, the Delaunay triangulation , and the quad tree method are only examples. The reader will be referred to two surveys of unstructured grid techniques. The first one by Mavriplis [12] gives an overview of mesh generation, adaptivity, discretization and solution strategies for unstructured meshes. The second by Owen [11] is accessible through the web and presents a survey of unstructured mesh generation, together with a review of almost a hundred grid generation softwares. **Adaptivity** is the second main advantage of unstructured meshes. Because no inherent structure is assumed in the representation of the mesh, points can be added, deleted or moved to optimize the accuracy of the numerical solution. As mentioned previously, we will consider only h-adaptivity or mesh enrichment where resolution is increased by adding more mesh

points as opposed to r-adaptivity where the points are moved or redistributed.

4.3.1 Grid refinement strategy

In ICECREMO2, the grids are generated using arbitrary polygonal shapes which gives a great flexibility for the mesh generation. However, to develop an automatic mesh refinement strategy on such general grids becomes really difficult. For this reason the method employed here for the mesh refinement utilizes a combination of edge splitting techniques and point insertion. This offers a very general and robust approach. For practical reasons however, this method has only been tested here on a hybrid mesh formed of squared and triangular cells. If there is no obvious reason why the entire method could not be generalized directly for an arbitrary polygonal grid, it would however be necessary to test it on different configurations. All the data interpolation part would remain exactly the same but the actual mesh enrichment could produce some elements of bad quality, such as flat triangles. It is important to outline that all of the methods described in this work relies extensively on the quality of the initial grid as the mesh is never regenerated during the refinement process. Although great care has been taken in order to avoid bad quality elements when the mesh is refined, if the initial grid is not of good quality originally, refining it could in some cases make it worse. Nevertheless, it is wise to assume that the computational grid input into the ICECREMO2 icing module MAGNUM is of reasonably good quality.

Splitting edges

Even when considering triangles and quads only, it is important to consider the different scenario. Although the error estimator is likely to flag edges for refinement which are in the same region of the domain we can not exclude particular cases.

Considering triangular cells first, for an element the error indicator can return one, two or three edges for refinement. Figure 4.9 represents how these cases are dealt with.

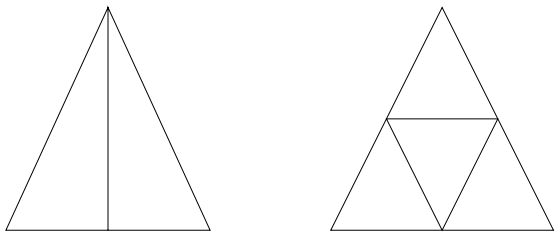

Figure 4.9: Edge splitting method on triangle

If only one edge is flagged for refinement, this edge is split into two edges and an additional point is created in the middle of the edge. By joining this new point with the opposite corner, a new edge is created and the original face is split into two. In a triangle if more than one edge is flagged, then all three edges are split and joined together leading to four new cells. With this method a reasonable mesh quality is kept. More, the same method could be used to improve grid quality by refining flat triangles this way.
There are more possible scenario with quads. One to four edges could be set for refinement. Figure 4.10 shows the different cases. If only one edge is refined, this edge is split into two as before but an additional point is created at the center of the cell and joined with the middle of the refined edge. The centroid is also joined with the two opposite corners to form a triangle. The division results in three new elements: one triangle and two quads. This splitting method is also used to deal with the hanging nodes (see below). If two opposite edges are flagged by the error indicator, these two edges are split into two and their middle points are joined to simply form two new quads. If more than two edges have to be refined or if these edges are not opposite to each other, then all edges are refined. An additional point at the centroid of the element is created and joined with each of the middle-point at the edges resulting in four new quads.

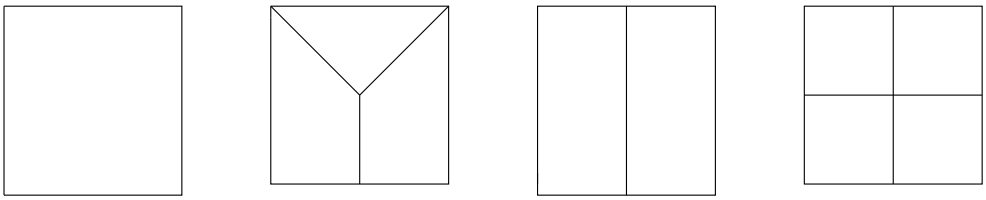

Figure 4.10: Edge splitting method on squares

This illustrates the fact that as a certain number of edges are indicated by the error estimator for refinement, a different number of additional cells can be created depending of the scenario. For example sending ten edges for refinement could result in only twelve new cells or thirty depending on how the edges are linked to each other. The main reason for that is the presence of hanging nodes. These hanging nodes appear between two adjacent cells when only one has been refined. The additional point created on the edge shared by these two adjacent cells is called an hanging node. If not treated these hanging nodes would create many complications. The solution would be discontinuous at these points and the conservation of the numerical scheme could not be assured. In many numerical methods, and this is the case of the finite volume, two adjacent element can only share one edge and an edge can only belong to two elements. To prevent hanging nodes additional refinement is needed. Once all flagged edges have been refined, we search for the presence of hanging nodes and perform additional refinement when necessary as pictured in Figure 4.11 where the dashed lines show how the adjacent cell is refined.

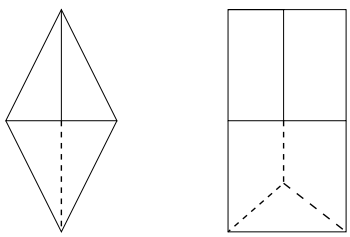

Figure 4.11: Hanging nodes

A typical sequence of refinement is represented below. On an arbitrary grid the error

estimator could return a list of edges to be refined, represented in dashed line in Figure 4.12. The resulting fine grid would then be as in Figure 4.13. Additional cells have been created to prevent hanging nodes. Note also that even when quads only are presents in the original grid, after several refinements, triangles may appear, creating an hybrid mesh.

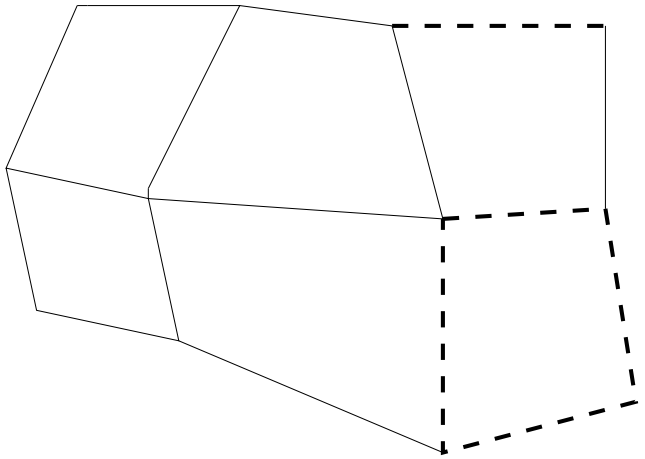

Figure 4.12: Before refinement

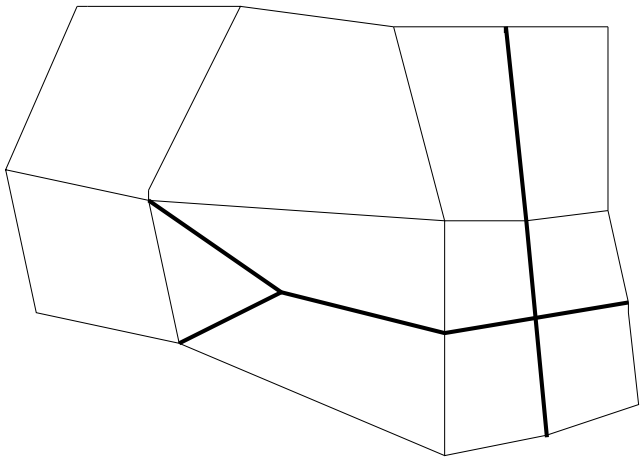

Figure 4.13: After refinement

This refinement process is made through three subroutines in ICECREMO2. Once the new edges are created the faces are reconstructed through the wingEdge structure. Old faces are deleted and the adequate data structure is built for the new elements. The

process is fully automatic and has proven to be very robust, although improvement might be done to generalize it to an arbitrary polygonal mesh and to make it more time-efficient.

Data interpolation

There are two aspects to the grid adaptation strategies. In the previous section we have described the mathematical and software mechanisms for deciding which mesh elements need to be refined or removed and the data structure manipulations involved in generating the new grids. Additionally, it is necessary to generate the appropriate data values associated with new cells.

As described previously, after the refinement has been made, the entire mesh structure has been reconstructed. Among many things this means that the elements have been renumbered. Some new elements have been created but also the indices of non-refined elements may have changed. In such case the data structure has to be modified so it carries the right information for the corresponding elements. A hierarchical data structure would have been ideal for mesh refinement. An element is refined into several children-cells which can in turn be refined in a tree sort of way, carrying the information up and down the tree branches have the mesh is refined or coarsened. However no such data structure is available in ICECREMO2. We opted instead for a mapping technique. As the mesh is refined each element carries the reference for its parent cell. Technically speaking a vector array is created at each refinement which carries the list of parent and children cells. The implementation of such algorithm is quite fastidious but still very robust and efficient. Once the mapping is done, the interpolation is straightforward. We used a constant interpolation for all the test presented in this thesis. Some work has been done to develop a more complex interpolation technique such as an operator based interpolation, but no generalization could be made for a two dimensional flow. One thing to keep in mind when

interpolating is the conservation principle. But when going from coarse to fine grid this is not a problem. The mass related variables here are the ice and water heights. As a face is refined into several children, setting the water and ice heights on these new faces so that it is equal to the value of the parent cell will conserve the overall mass. The other variables are also updated using constant interpolation although this is of less importance as these variables are updated at the beginning of each time step and the refinement is always performed at the end of a time step. The external flow as well as the heat transfer are interpolated and not recalculated after each refinement. This can be improved using a multi-stepping approach [20].

4.3.2 De-refinement

We use the term de-refinement in this document to distinguish between coarsening: the arbitrary removal of grid nodes (or edges) and de-refinement: the removal only of edges which have been added in a earlier refinement process. The data structure in ICECREMO2 does not support arbitrary removal of nodes and edges so the original surface mesh is retained as a reference and refinement is performed relatively to this initial mesh. If the de-refinement option is selected, a second mesh, mesh initial, is created during the initialization as a copy of the current surface mesh. No computation will be perform on this mesh until the de-refinement cycle is reached. So it will keep the size, structure and face numbering of the initial grid. The first de-refinement will be performed the cycle before the second refinement, and then the cycle before every other refinement. The data of the fine grid are then injected to the initial coarse grid. This is done using the same mapping technique as described in the previous section which keeps the history of the refinement. The interpolation again uses a constant interpolation technique but this time the size of the parent and children faces has to be taken into account in order

to respect the mass conservation. The interpolation is made respectfully to the relation:

$$h_p * A_p = \sum_{i \in children} h_{C_i} * A_{C_i} \tag{4.6}$$

where the subscript $_p$ is for the parent cell, h is the water height, A is the area of the cell and C_i are the set of children cells. The same formula is valid for the ice. This will guaranty that no mass is lost or added during the interpolation.

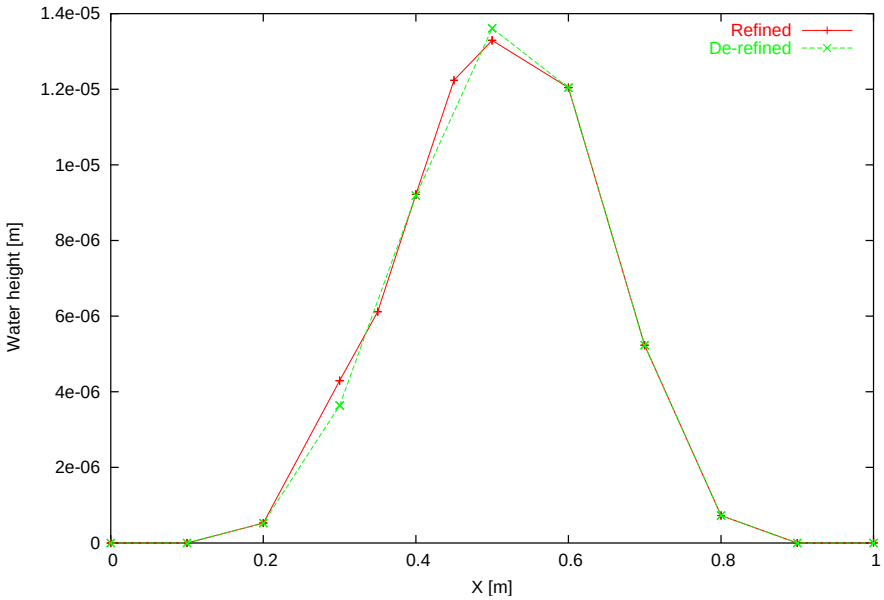

Figure 4.14: De-refinement on coarse grid

In the ideal case, where we can guarantee that the solution changes slowly in regions where the mesh is changing, then data transfer is not a critical problem since interpolation errors will be small. However, this is only possible where we can arbitrarily remove nodes. The current ICECREMO2 formulation necessitates to use the original mesh as an underlying reference and refinement is made relative to this and the coarsening process will never remove any of these grid structures. As highlighted previously the quality of the original grid is of great importance. To illustrate this, we performed a de-refinement

in a very coarse grid, see Figure 4.14. Although the solution is relatively smooth the loss of accuracy is quite visible. The same calculation is performed on a finer grid in Figure 4.15 and the difference is barely visible. A close up of the solution is given in Figure 4.16.

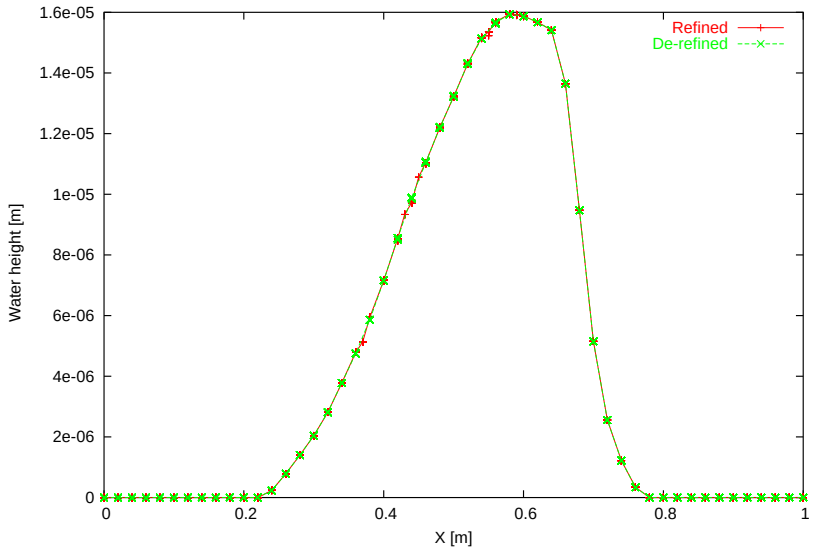

Figure 4.15: De-refinement on finer grid

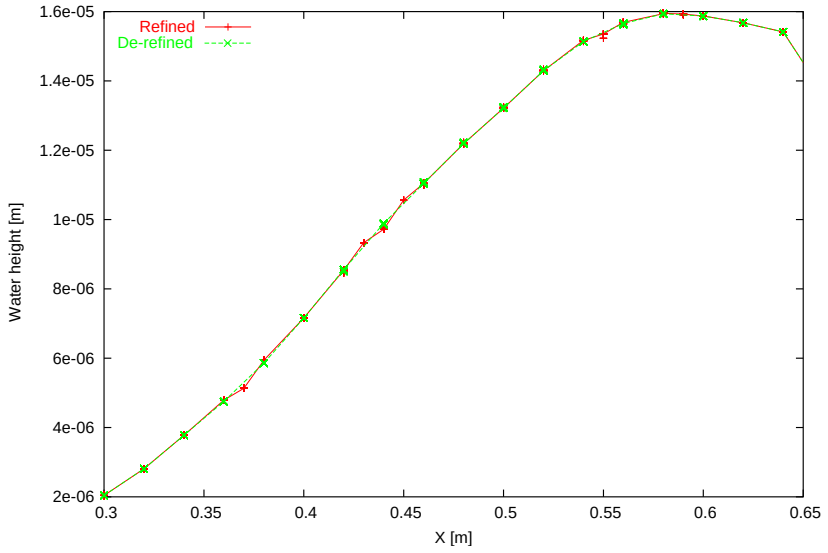

Figure 4.16: De-refinement on finer grid, close-up view

Furthermore as coarsening is supposed to happen only in region of very smooth flow

where high resolution is not required we can safely assume the good behavior of this method.

Grid transfer

Not having a hierarchical data structure brought another issue. In a transient problem like ours, the fine grid has to move together with the front so that the shock region stays under higher spatial resolution to compensate the loss of accuracy of the numerical scheme which switches to first-order in this region. The original intention was to perform grid refinement and coarsening subject to these constraints and to transfer solution data from one refined grid directly to the new mesh. Such implementation is very difficult and requires complex mapping algorithms which are not time efficient. Furthermore, the generalisation to arbitrary polygonal cells is virtually impossible as the number of child cells is unknown. The current implementation involves interpolation to the base grid and then re-mapping to the fine grid. Numerical experiments have shown that, providing the interpolation is reasonable this process is acceptable and efficient. The reason for this is interesting. The fine features of the flow are all associated with short length scales and short time scales. We have developed a coarsening map which preserves mass exactly. If the coarse grid is not sufficiently accurate to represent the small structures at a particular location then the associated mass is re-distributed. After interpolation to the fine grid is carried out and time-stepping is resumed the structures rapidly re-develop and there is very little inaccuracy observable after a few time steps.

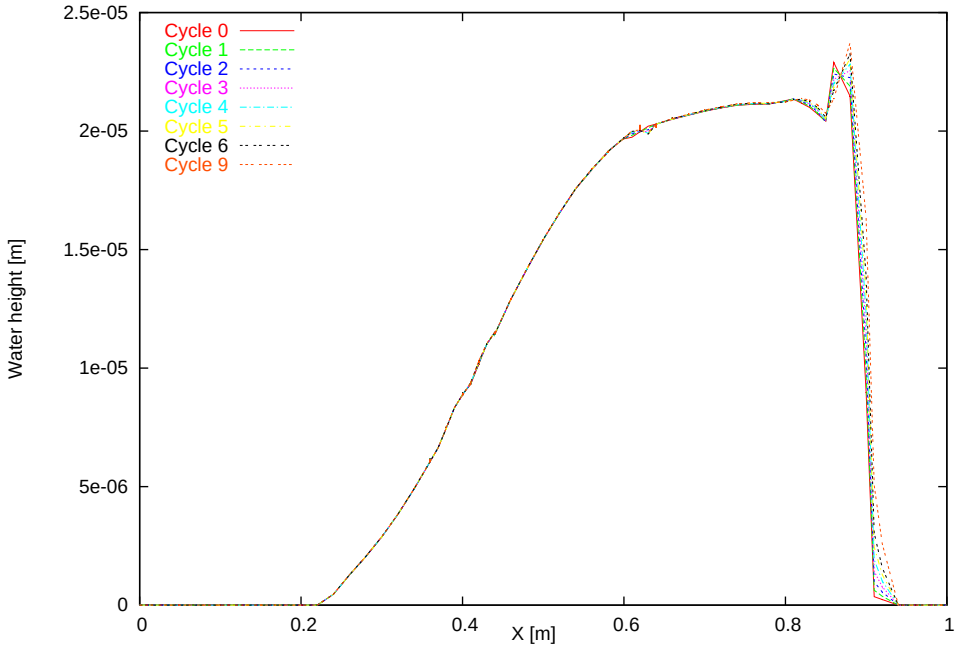

Figure 4.17: Peak recovery immediately after refinement

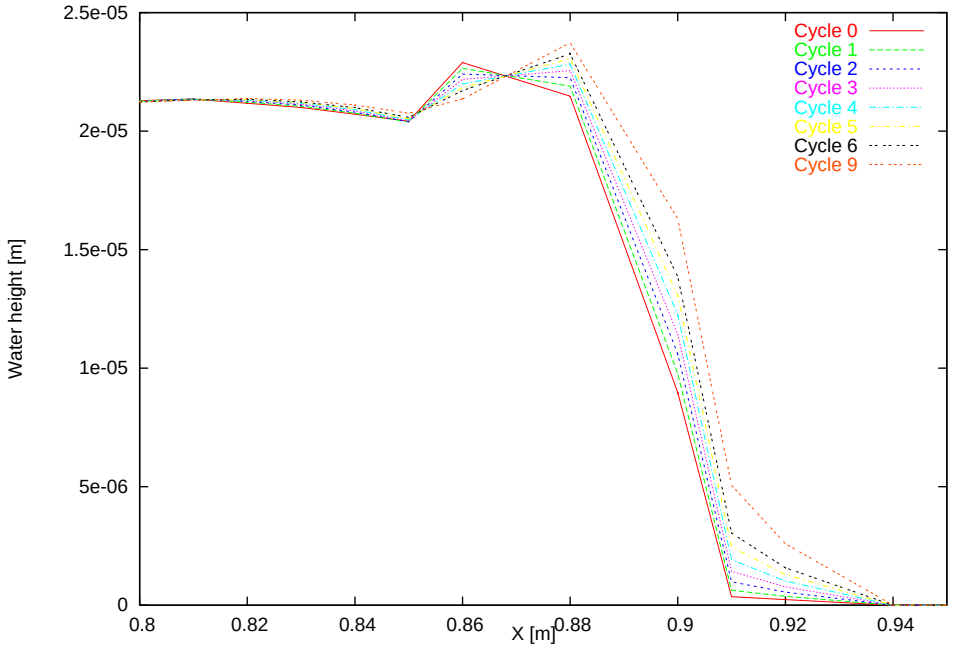

Figure 4.18: Peak recovery, close-up view

4.4 Automatic mesh refinement: results

The combination of refinement and de-refinement methods described above leads to an automatic adaptive method capable of producing a grid which will dynamically follow the flow. For simplicity we have fixed the number of edges to be refined to 10% of the original number of edges. This can easily be adjusted to a more convenient number or threshold depending of the complexity of the flow. The frequency of refinement and de-refinement is also taken constant. Depending of the speed of the front and the level of refinement (number of edges added for each refinement), this is the part one wants to keep as low as possible. Refining and de-refining too often would introduce some interpolation errors, and on the other hand if the front leaves a fine region we would lose accuracy. This can be avoided by testing and requiring that the maximum error does not go over a certain threshold. However this threshold would be dependent on the test case.

4.4.1 Moving grids with front: flat plate case

In this section we present a sequence of adaptive meshes obtained in the computation of thin water film spreading on a flat plate under wind forces. The shear stress is acting parallel to the plate in the X direction. The initial conditions are a 2D gaussian, the initial bulk of water is constant in Y direction. This calculation simulates a "wave" spreading on a flat surface. When adaptivity is performed, the observation of the numerical grid shows some indication of the evolution of the flow (see Figure 4.19).

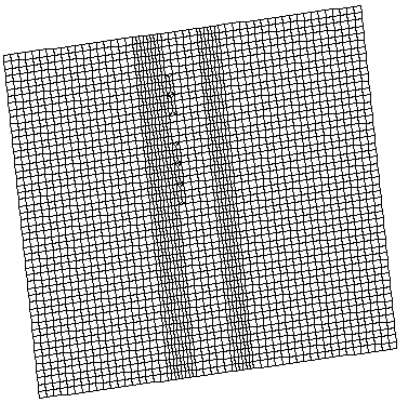

(a) grid-1

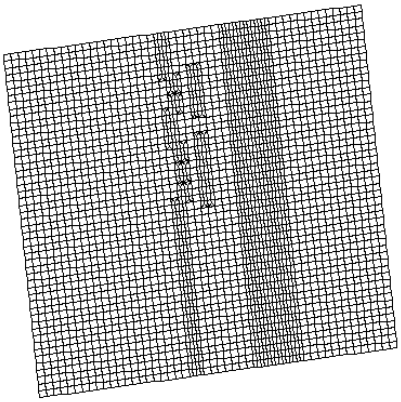

(b) grid-2

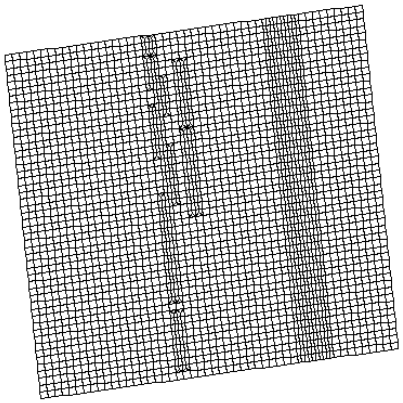

(c) grid-3

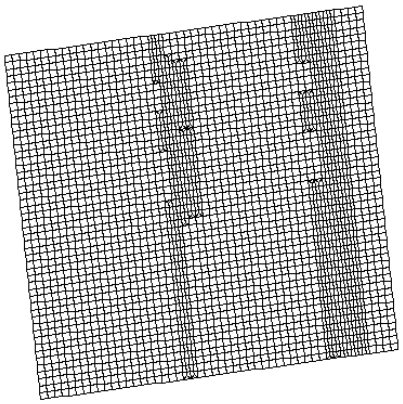

(d) grid-4

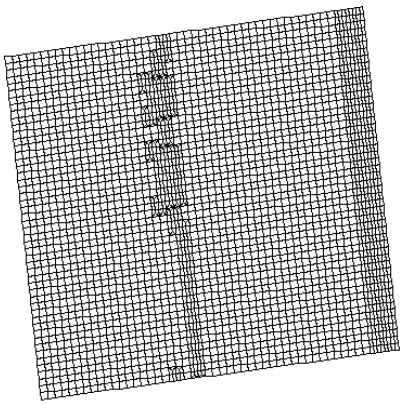

(e) grid-5

Figure 4.19: Adaptive mesh for an horizontal flat plate case at different time.

As the front advances and sharpens, this region moves rightward and becomes more broad. The left hand border becomes slightly thinner since the current refinement strategy maintains the total number of refined cells approximately constant (this is not essential, merely convenient). Moreover, this region becomes comparatively smoother as the computation progresses, so the error estimator selects the downstream front for the majority of the refinement. There are minor 3D effects in the calculation, and minor differences in the results of the computations which cause the variations in the grid. These do not have a significant effect on the calculated film heights and could be removed by adjusting the total number of refined cells.

In Figure 4.20, we present a similar test case but this time the flow is not alined with the grid. The shear stress has been given a 45° angle with the plate. More triangles are present in this case around the advancing front. Also we can observe that the flow development region is de-refined in one direction only as thin rectangles are visible instead of squares. The only region totally de-refined is the top of the water film where it has reached a steady height.

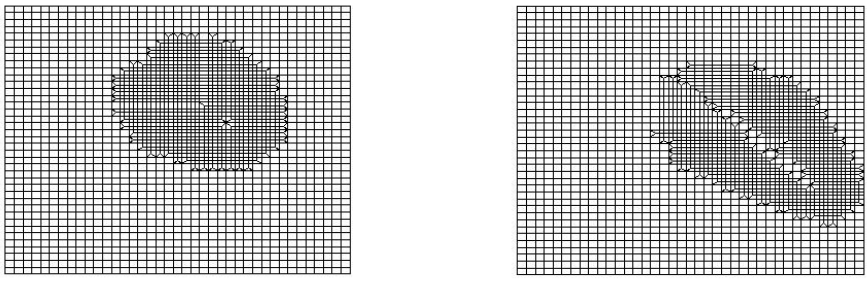

(a) grid-1 (b) grid-2

Figure 4.20: Adaptive mesh for an horizontal flat plate case at different time with an angle.

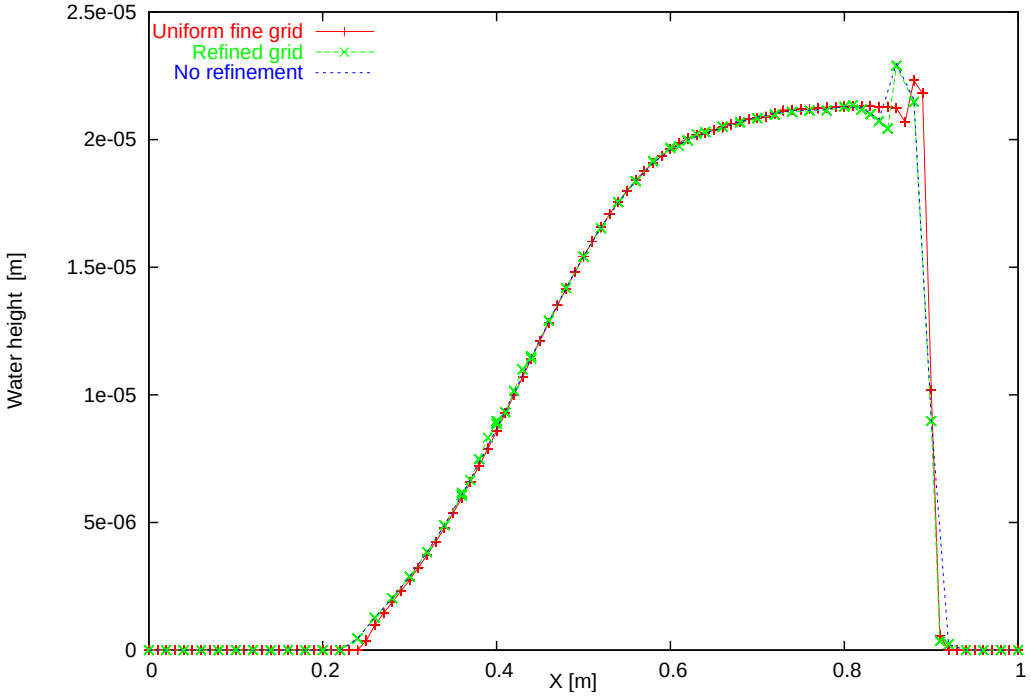

Figure 4.21: Comparison between coarse fine and adapted.

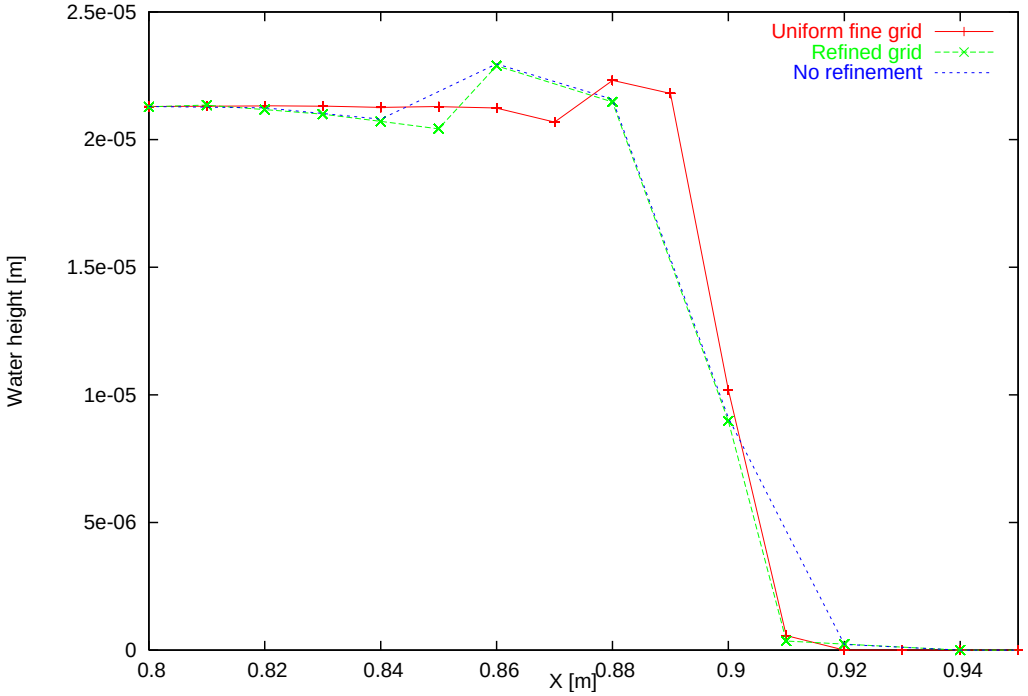

Figure 4.22: Comparison between coarse fine and adapted, close-up view

Figures 4.21 and 4.22 we show the solutions in two dimensions, after four seconds of exposure time, obtained on coarse, fine and adapted grids. The results are very similar. As expected the solutions agree where the film height varies slowly. At the advancing front there are some improvements in the solution obtained with the adapted grid (compared to the coarse grid solution). In particular the bottom advancing front is improved compared to the coarse grid solution.

Grid orientation

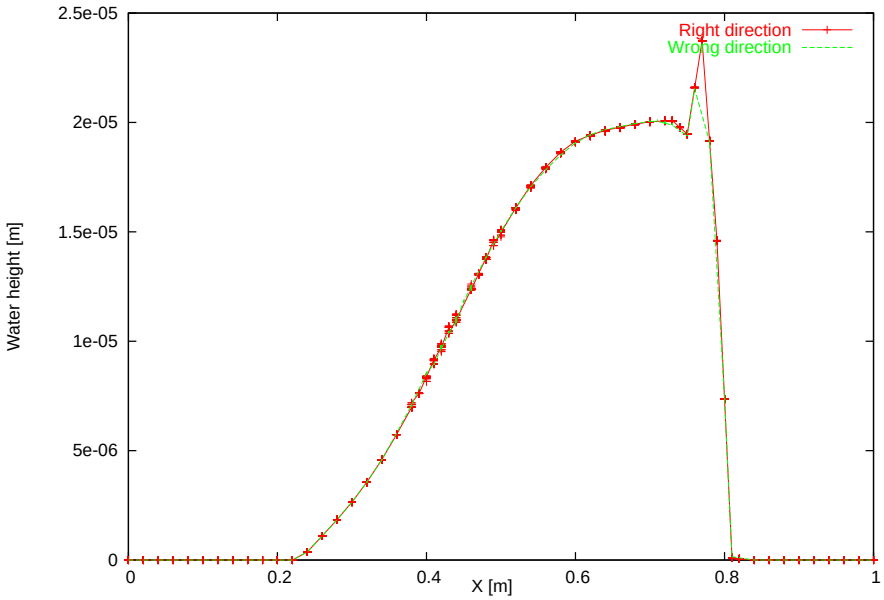

Figure 4.23: Difference in refinement direction

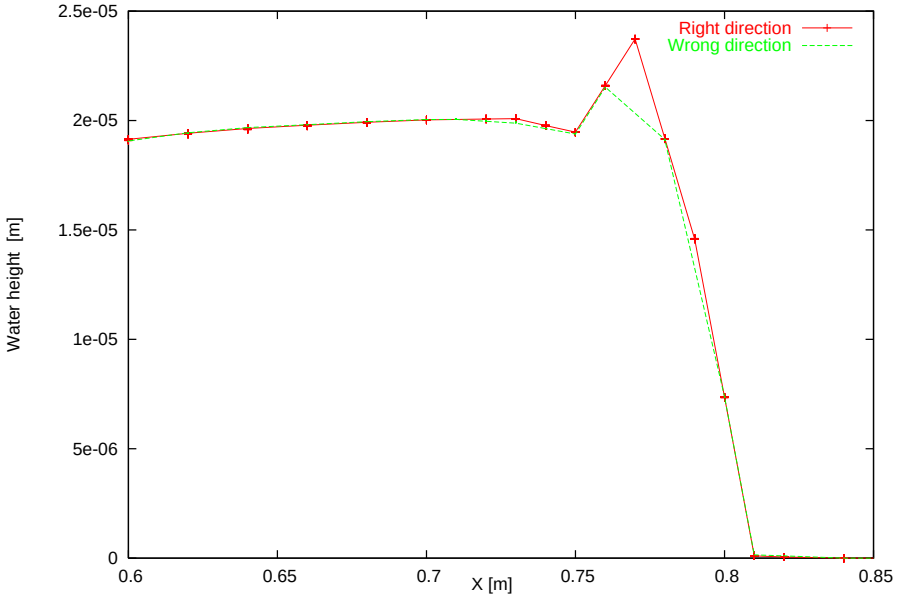

Figure 4.24: Difference of refinement, close-up view

Refining all the edges of a flagged cell is not always necessary, especially with idealized test cases like those used in this thesis when the direction of the flow remains quasi constant during the entire calculation. More precisely, in the case of quadrilateral cells like in all the cases presented so far, the edge flagged by the error estimator is not the one which has to be refined but the edges perpendicular to it. Basically if the flow is in the x-direction, refinement has to be made with respect to Δx not Δy. If this sounds like an obvious remark it is however very important to take this in consideration during the implementation of such method.

Figures 4.23 and 4.24 the film height is represented together with the grid points on a 2D case. Refining the grid in the right direction (here in red) add some more grid points in the front region. Also in Figure 4.19, refinement has been performed only in the x-direction, the direction of the flow, keeping the mesh quality and quadrilateral shape of the original grid. Only minor grid artefact or triangle appear in the flow development region due to the number of additional edge being too low and the presence of hanging nodes.

4.4.2 Results on a NACA0012 airfoil

The grid refinement strategy described previously will now be applied to a NACA0012 wing section. This airfoil has a symmetric shape and supercooled droplets impinge on the surface with an angle of attack of 3°. The water droplets hit the airfoil at the leading edge and the shear stress acting parallel to the x direction pushes the liquid towards the upper and lower part of the airfoil. A sequence of the computing grid resulting from the adaptive process is presented.

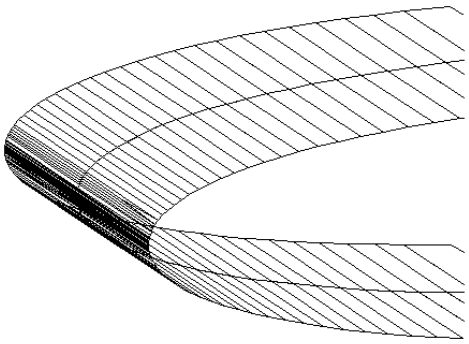

(a) initial grid

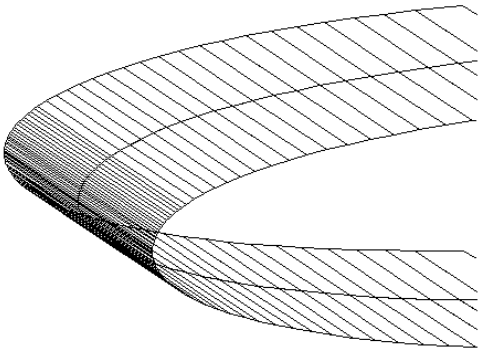

(b) grid 1

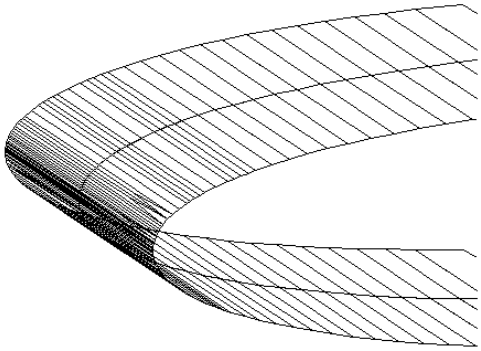

(c) grid 2

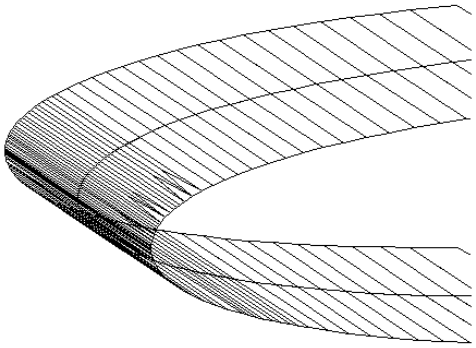

(d) grid 3

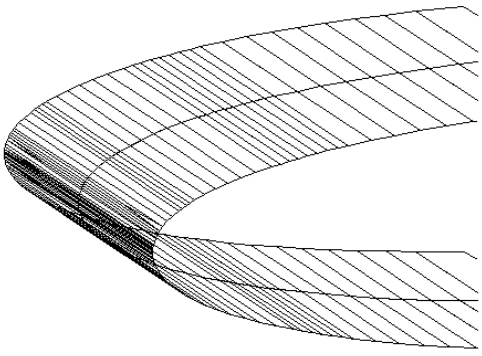

(e) grid 4

Figure 4.25: Sequence of adaptive grids on a NACA0012 test case.

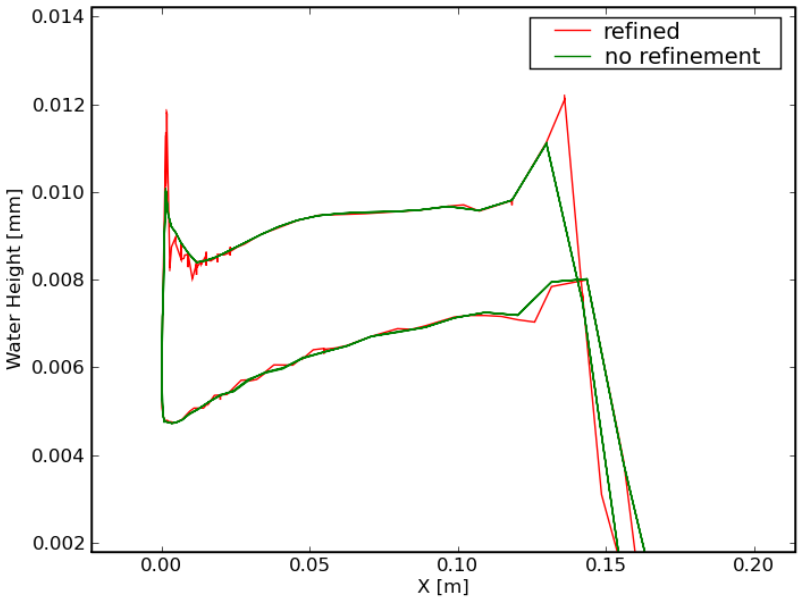

Figure 4.26: NACA0012, coarse and refined solutions

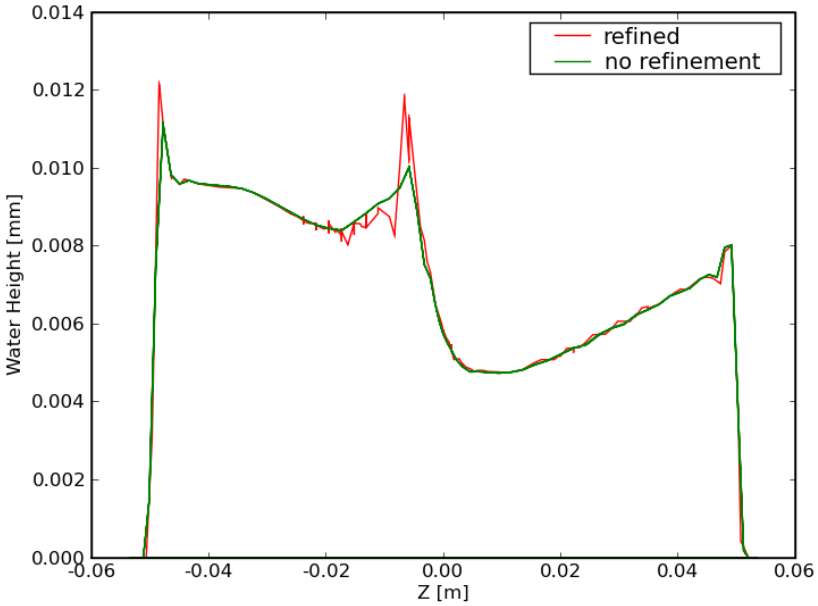

Figure 4.27: NACA0012, coarse and refined solutions, view with respect to z-coordinates

This test case is pseudo 2D, there is only two cells in the y-direction and the flow is unidirectional parallel to the x-axis. Figure 4.25 shows the evolution of the grid for the NACA 0012 (C17) test case. There is an initial concentration of cells at the leading edge and as time progresses and the water moves backwards there is refinement at the two advancing fronts, although the leading edge also retains a peak in the flow and so we see a concentration of grid cells remaining there.

We compare solutions obtained on a 132 cells grid and on an adapted grid with 170 cells in Figures 4.26 and 4.27. The upper curve represents the film height on the lower surface (the pressure distribution around the airfoil means that the catch is higher on the lower surface and this is reflected in the profiles). This phenomenon is due to the angle of attack and to a minor degree the effect of gravity. It is clear that the grid refinement has captured the height of the peak and the sharpness of the advancing front on the lower surface more accurately. On the upper surface the differences are less marked - although some improvements can be observed. The peak at the leading edge (x = 0) is also better captured by the adapted grid. This test case will be presented in more detail in the next chapter.

4.4.3 Computational requirement

The principal goal in developing an adaptive method is the gain of accuracy without increasing too much the CPU time. We have already compared the solution obtained on globally refined and adaptive grids. Although the test cases presented here do not contain many cells, we can already see a net increase in performance for the adaptive calculation. Each calculation has been performed in serial on one of the 19 computer nodes of the cluster grid at Cranfield University. Each 32-bit node is composed of two Intel Xeon 3.06GHZ processors with 6GB of shared memory attached to it.

The coarse grid contains a total of 1250 cells and the fine grid 5000 cells. The adaptive

computation starts on the same coarse grid and finishes with a mesh of 1306 cells. The total number of cells could vary slightly during the simulation as only a percentage of the total number of edges is added in the refinement process. The treatment of hanging nodes will vary the number of edges added hence the number of faces or cells. To clarify the advantage of the adaptive method in terms of computational resources, the total memory and CPU time required for each simulation are summarizes in the Table 4.4.3. The time is display in hours, minutes , seconds (hh.mm.ss).

	coarse	adaptive	fine
CPU Time [hh.mm.ss]	00.07.46	00.20.47	02.20.11
Memory MB	26.23	33.84	37.52

The improvement in CPU time is obvious, an adaptive calculation will take less than 15% of the CPU time required with an equivalent globally refined grid. There is however an overhead present when doing adaptivity due to the interpolation required from grid to grid after each refinement and de-refinement and also to the re-meshing itself. The resource required for the computation of the error estimator is negligible.

The improvement in memory requirement is less marked but still significant as the increase of memory with respect to the coarse grid computation is only of 29% for the adaptive computation against 43% for the globally refined grid. Note that these numbers correspond to a maximal memory load. During an adaptive computation, the reference grid will always be stored hence increasing the memory load compared to non-adaptive calculations. However, no data will be stored on this reference grid. During the interpolation from fine to coarse grid, the data are passed from one grid to another and the memory requirement will actually double. This had no effect for the simulations performed in this work as we never reached the maximum memory available, but for large scale or parallel simulations this phenomenon would have to be taken into account to prevent bottle-neck

effects. Also no effort has been made to optimize the performance of the adaptive process as for a global icing simulation, the computing requirement of the solver module MAGNUM is relatively small compared to the two other modules, specially CORNETTO the droplet trajectory module.

4.5 Conclusion

We have presented in this chapter the automatic mesh refinement method developed in this thesis. After a brief review on the different sources of error that should be taken into account when solving the thin film flow equation, we concentrated on the truncation error which is directly linked to the numerical scheme and the level of resolution used. It is therefore this numerical error that adaptivity ought to reduce. To obtain an adaptive method one must first define an error estimator which defines the region where the grid refinement is necessary. This is a difficult process and several choices are possible. As we concentrate on the resolution of the liquid film, it was necessary to define an estimator which would allow the refinement of the advancing front region while leaving the rest of the mesh un-refined.

For the error estimator we used the double discretisation inherent from the numerical scheme presented in the previous chapter. This high resolution method combined a second-order Lax-Wendroff scheme with a first-order upwind and the main difference between the two discretisations is in regions of sharp gradient. The error estimator returns a list of edges to be refined. The amount of edges to refine is user-defined and the total number can vary slightly depending of the type of cells used and the presence of hanging nodes. Due to the data structure of ICECREMO2, the de-refinement is made with respect to the original grid. Only one level of refinement de-refinement can be performed at a time. Although it is possible to refine until necessary, the de-refinement can only be made to the

"previous" grid and never coarser than the original mesh. All the interpolation from grid to grid is conservative so the global solution method is also conservative. The overall process is an automatic mesh refinement method which will produce meshes which dynamically follow the front part of the liquid film (or any part where a sharp gradient is present). The solution obtained on adaptive grid compares well with globally refined grid with a 50% gain of CPU time on a simple 3D test case.

On the following chapter we test how the resolution of the front of the water film affects any icing related results as well as another refinement criteria with respect to the ice layer.

Chapter 5

Icing Calculations

5.1 Introduction

In this chapter we present the results related to icing obtained with the high resolution method developed earlier in this thesis. The main purpose is to assess the performance of a high resolution method and the importance of the water film resolution on glaze ice accretion. Water and ice evolve at different time scales and although they are obviously linked it is not sure if small changes in the water film will have a significant effect upon the final ice shape. In this work we show that the presence of the front and small scale features of the water film affect the ice shape in the first phase of the icing process when the water film has not reached a steady state. However the steady state is reached very quickly compared to a full icing simulation, and we present alternative criteria for the grid refinement which take into account the ice layer once the steady state is reached.
But first let's recall Equation 1.1 governing the water flow and ice accretion:

$$\frac{\partial h}{\partial t} + \nabla . Q = \frac{\beta W G}{\rho_w} - \frac{\rho_i}{\rho_w} \frac{\partial b}{\partial t} \tag{5.1}$$

where Q represent the water flux. A full derivation of this equation is available in [1, 2, 3, 4]. The left hand side of the equation describes the evolution of the water film, while the right hand side represents the incoming water or droplets and the ice grow $\frac{\partial b}{\partial t}$. In mild temperature when glaze ice forms, the ice thickness is derived from the energy balance at the freezing interface and can be written in its non-dimensionalised form as:

$$S\frac{\partial b}{\partial t} = \frac{1}{b} + \frac{c_{2g}}{1 + c_{1g}h} \tag{5.2}$$

S is the Stephan number and the c_{1g} and c_{2g} terms describe different terms in the energy balance such as evaporation aerodynamic heating, droplet kinetic energy, convection, etc (see details in [1, 4]). In this form we can predict the behaviour of the ice growth $\frac{\partial b}{\partial t}$ with respect to the ice and water thickness, b and h. For example, we can see that, at constant condition, the growth of ice will decrease as the water thickness increases. In the following sections we take a close look at the front of the water film and assess how the increase of water mass at the front when resolved with a high resolution method will affect the amount of ice to form.

We start with some idealised test cases in two and three dimensions at different temperature. Then we present the results obtained with adaptivity on a NACA0012 and a cylinder, on two-dimensional test cases which are references in the icing community.

5.2 Icing on a plate

5.2.1 Two dimensional case

In this section we simulate the spreading of a water film on a 2D flat plate at temperature below zero degree Celsius. The impinging zone is situated on the left hand side of the plate and the shear stress is acting uniformly in the x direction (from left to right). Figures 5.1

and 5.2 represent simultaneously the water film and the ice height at different exposure time. As the water spreads on the surface, a larger area of the domain is exposed to ice accretion. The water height in the steady state region is not constant anymore. As water freezes and transforms into ice, there is a sink of water mass and the height of the film decreases as the liquid spreads over the domain. The ice shape in such idealised test case is very simple. Two parts can be distinguished. The left part, in the impinging zone, conserves exactly the shape of the collection efficiency as the film height in this region stays constant. In the right part of the domain, ice starts to appear as the water film advances toward the right.

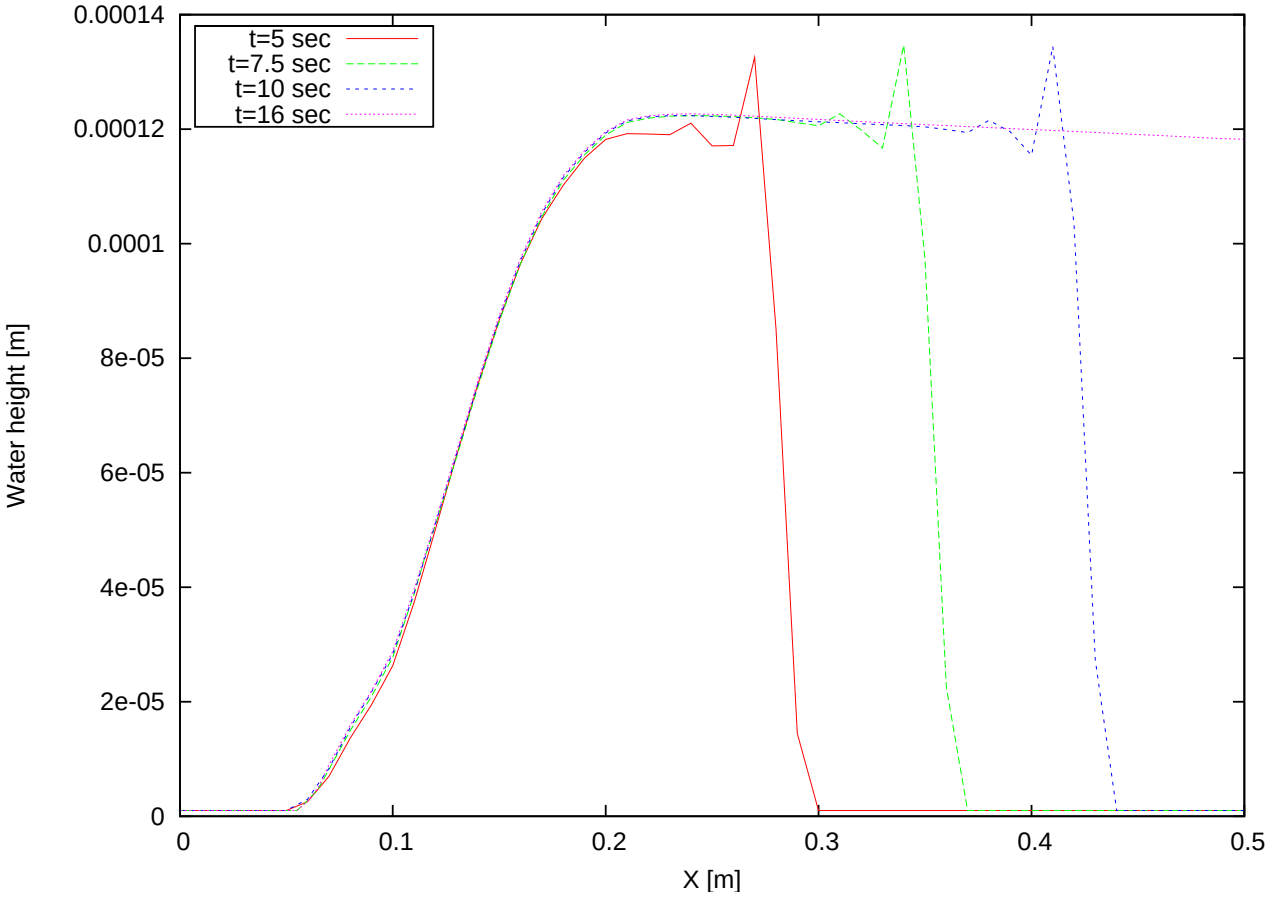

Figure 5.1: Water height on an horizontal flat plate

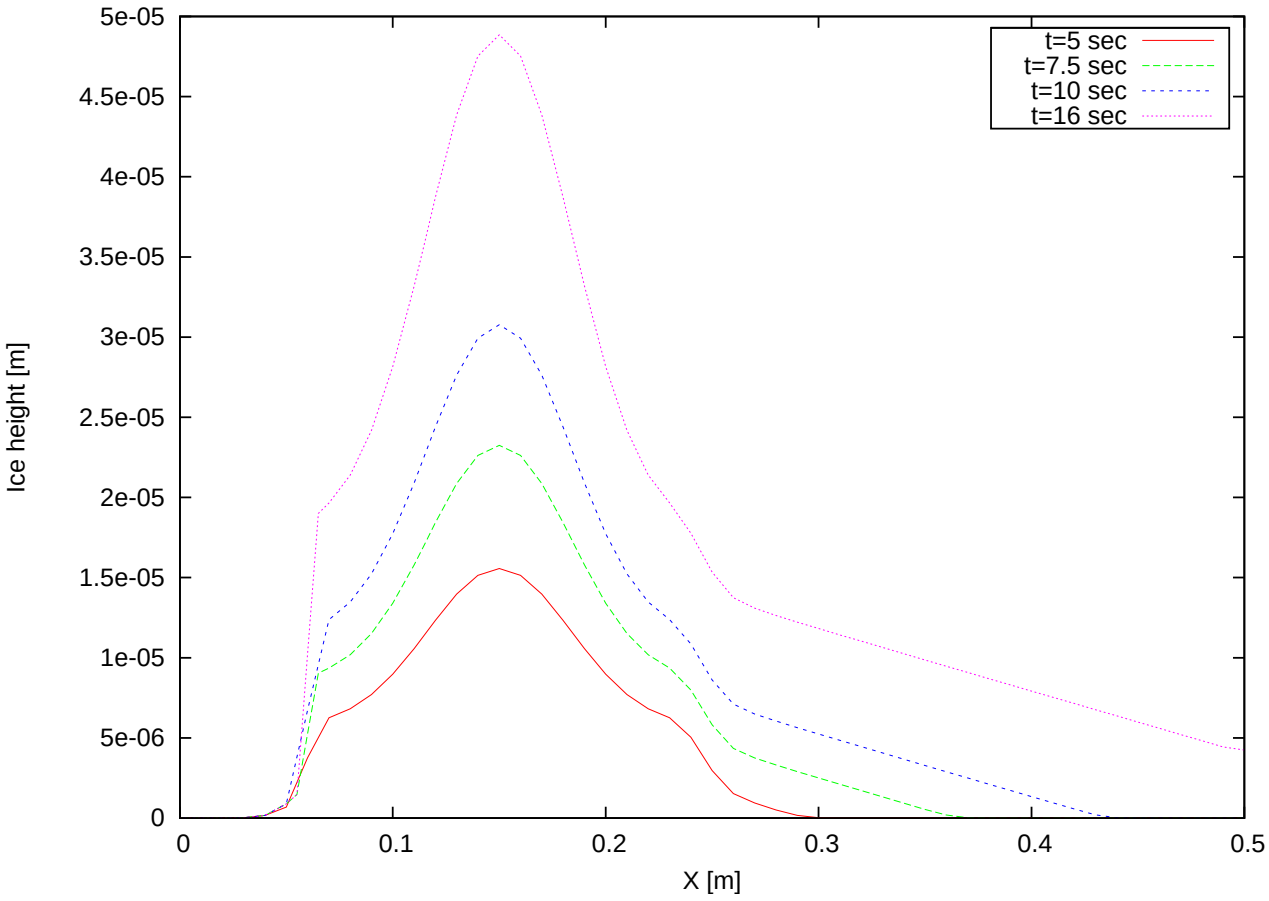

Figure 5.2: Ice height on an horizontal flat plate

The ice growth is of course dependent on the temperature. Here the water and the substrate temperatures are considered equal to the ambient temperature. Below in Figure 5.3 we show both water film and ice heights for different temperature after 45 seconds of exposure time. We can see that when the temperature decreases the growth rate increases , and for the lowest temperature the water does not reach the end of the domain.

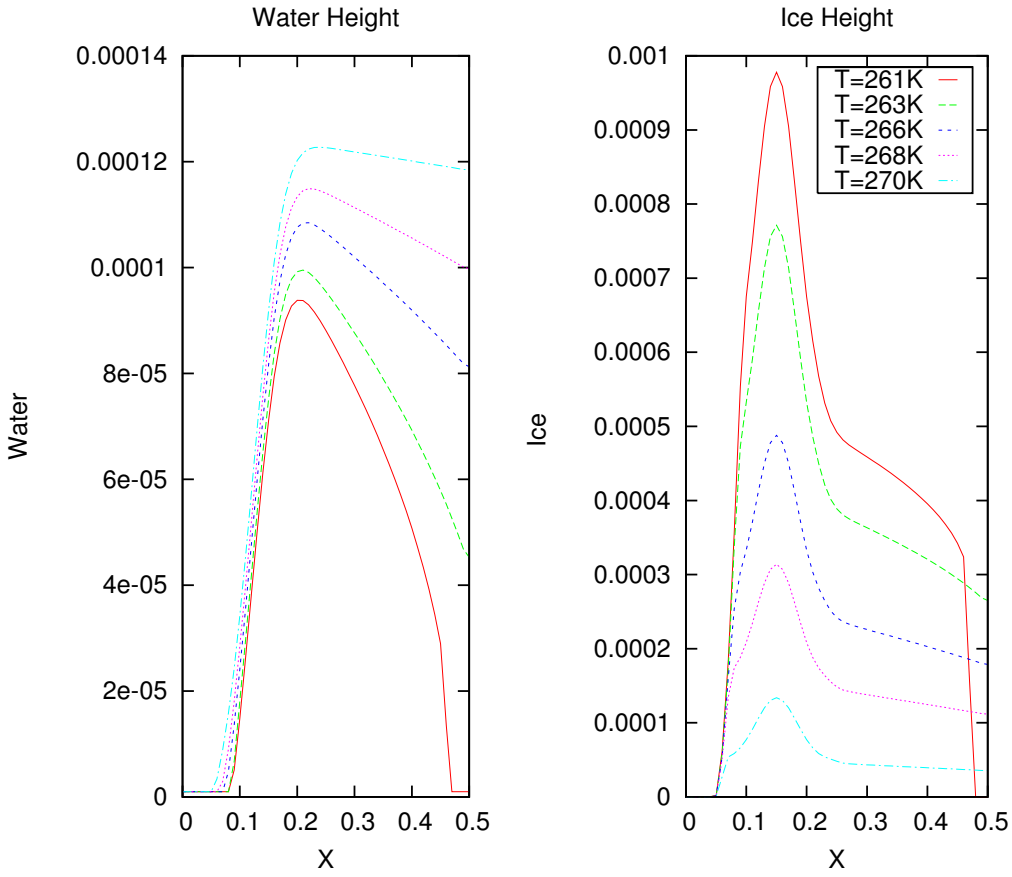

Figure 5.3: Water and ice heights on an horizontal flat plate for different temperatures after 45 seconds

In Figure 5.4 we represent the volume of water and ice over the all domain as a function of time. The moment when the water film reaches a steady state is illustrated by the point where the total volume of water stays constant. At that point the ice growth becomes linear in time. The steady state is reached later at lower temperature.

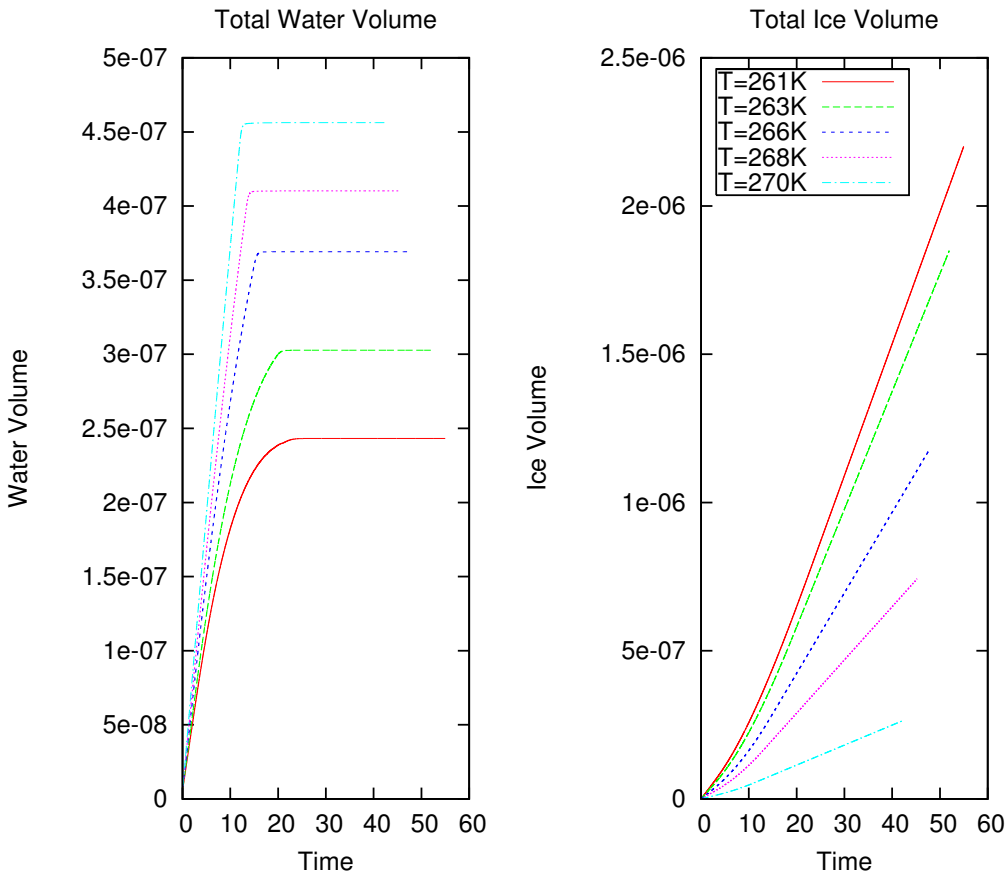

Figure 5.4: Total ice and water volume with time at different temperature.

We compare below the ice shape obtained with the first-order upwind scheme on fixed grid and the higher order method on an adaptive grid.

At temperature just below zero, T=270.2 K (figure 5.5), the difference between the two solvers is small. More ice has formed in the peak region, but both methods are globally equivalent for the whole domain.

At lower temperature, in Figure 5.6, we can notice a difference between the two methods on the right part of the domain which corresponds to the advancing water front. The high resolution method predicts less ice. The peak present at the front of the water film increase the water height h at the front compared to an upwind simulation. This increase

in water height results in a decrease of the ice growth rate $\frac{\partial B}{\partial t}$ (see 1.7 in Chapter 1) and thus the final ice height at a given time.

At even lower temperature, $T = 261K$, the difference at first is less noticeable. On 5.7 we can see that after $10sec$ of exposure time there is little difference between both methods. The high resolution method still predicts less ice accretion but not on the far right. However after a longer exposure, 30 and 45 seconds, we can see in Figure 5.8 that the high resolution method predicts some ice accretion further right than the upwind method. The presence of the front in the water film decreases the ice growth rate $\frac{\partial B}{\partial t}$ so less water is transformed into ice and the runback film extend further on the surface.

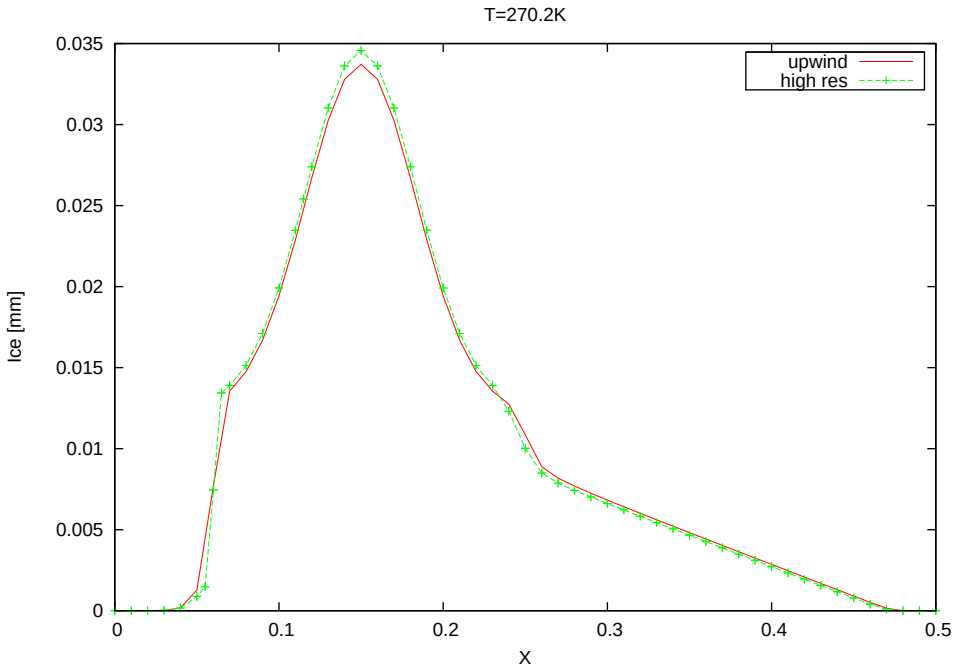

Figure 5.5: Ice growth after 10s at T=270.2K.

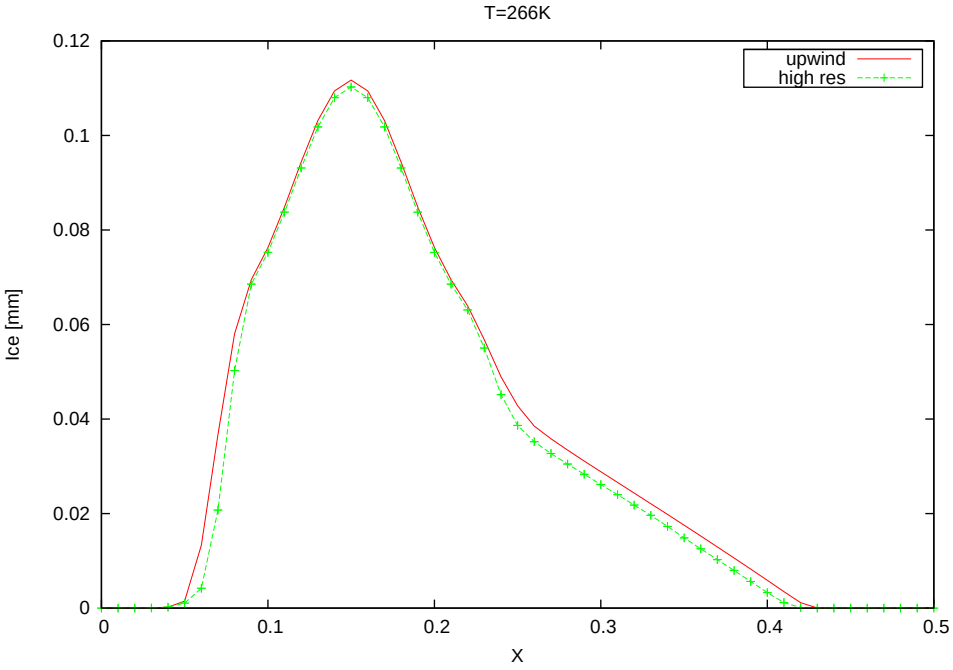

Figure 5.6: Ice growth after 10s at T=266K.

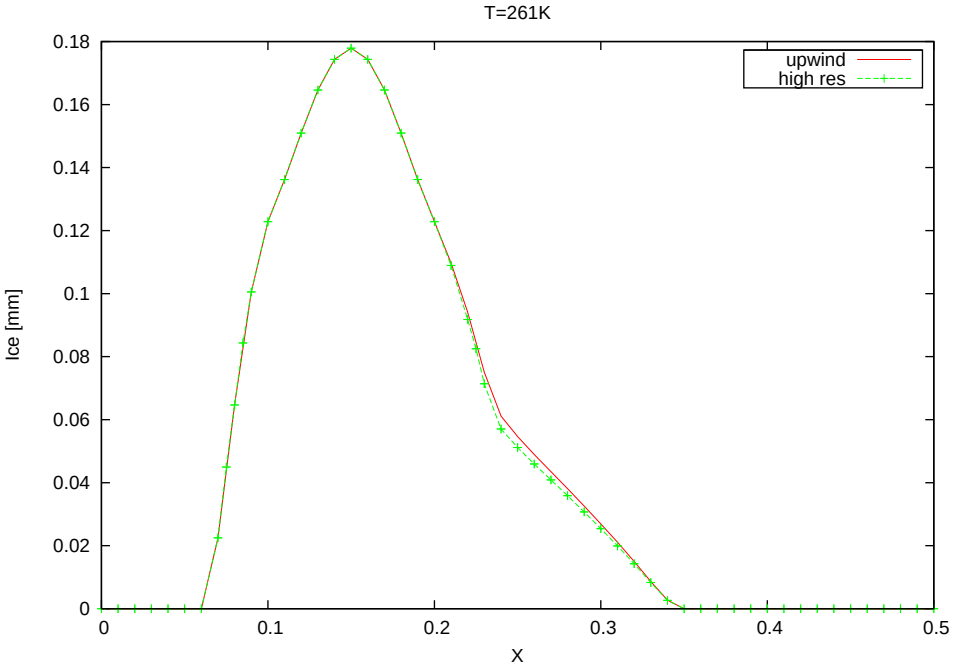

Figure 5.7: Ice growth after 10s at T=261K.

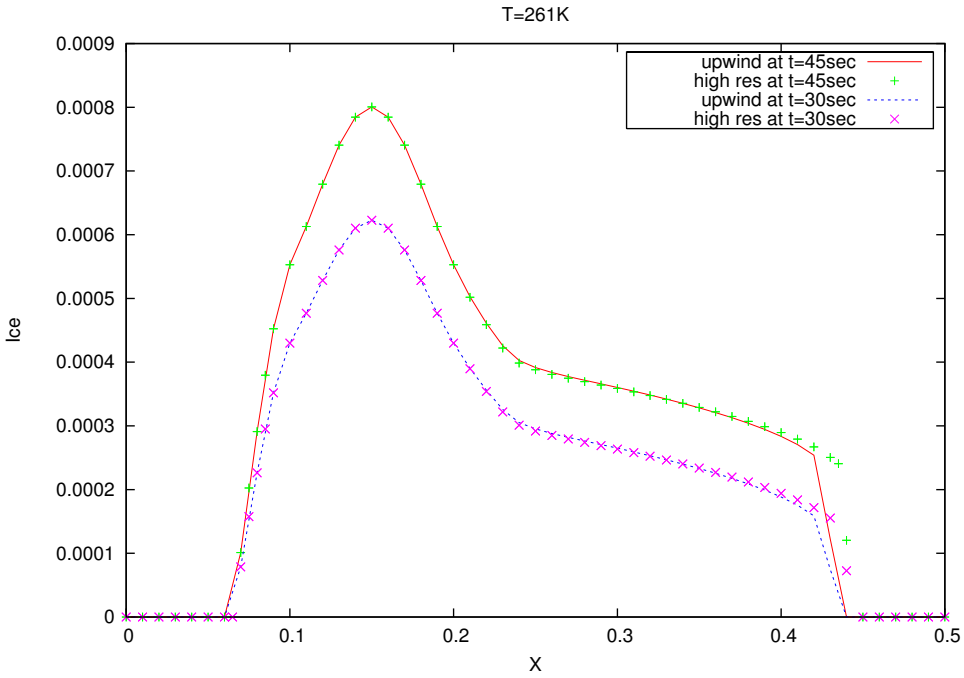

Figure 5.8: Ice growth after 30 and 45s at T=261K.

5.2.2 Three dimensional case

In this section, a three dimensional simulation of glaze ice accretion and water film flow on an horizontal flat plate is presented. The initial conditions for this test case are similar to the two-dimensional one. The usual pre-wetted substrate scenario is used with a precursor film height of $1\mu m$. The water entering the domain is modelled with a Gaussian shaped collection efficiency applied on one side of the domain and the shear stress is acting constantly in both x and y direction as illustrated in Figure 5.9. Droplet and substrate temperatures are considered constant in time and space and equal to the ambient temperature $T = 270K$.

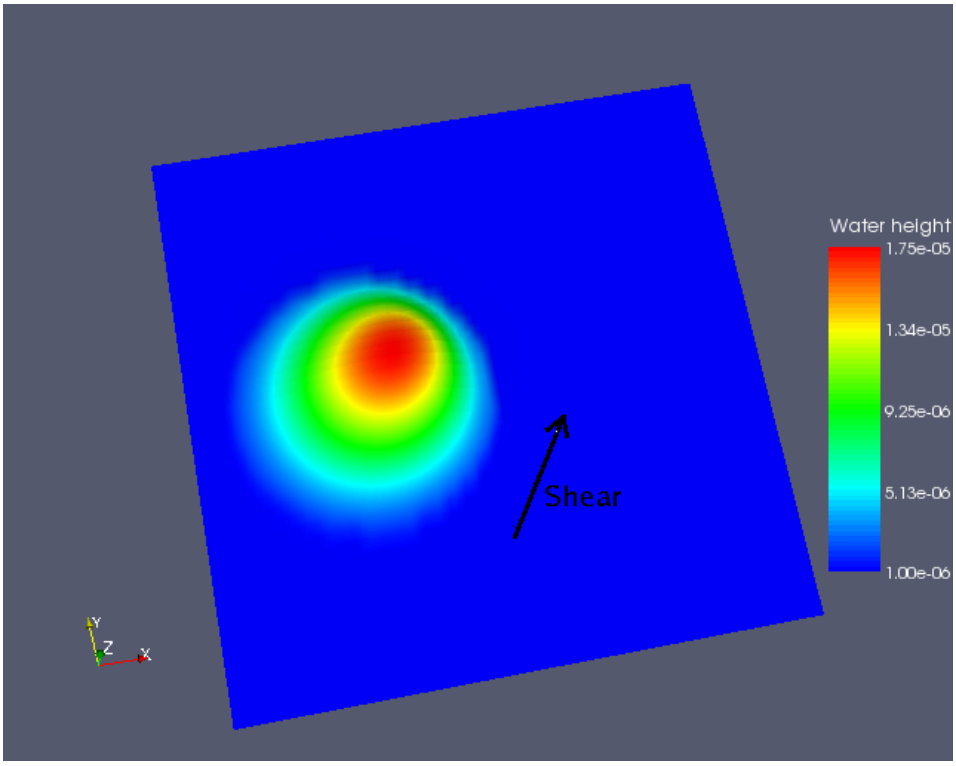

Figure 5.9: Initial conditions of 3D flat test case, collection efficiency

In the following we compare ice and water heights obtained with the classic first-order upwind method to those obtained with the high resolution method combined with adaptivity.

First comparing the water height after a short elapsed time we can see in the figure below that the difference is again mainly noticeable at the advancing front. The high resolution method, represented on the grid in Figure 5.10 presents a much sharper structure at the front as well as a slightly higher equilibrium height than the first-order calculation (represented as a plain surface). Also the water surface obtained with the upwind method is much smoother and the front is less advanced on the domain. This confirms the observations made on the two dimensional test case.

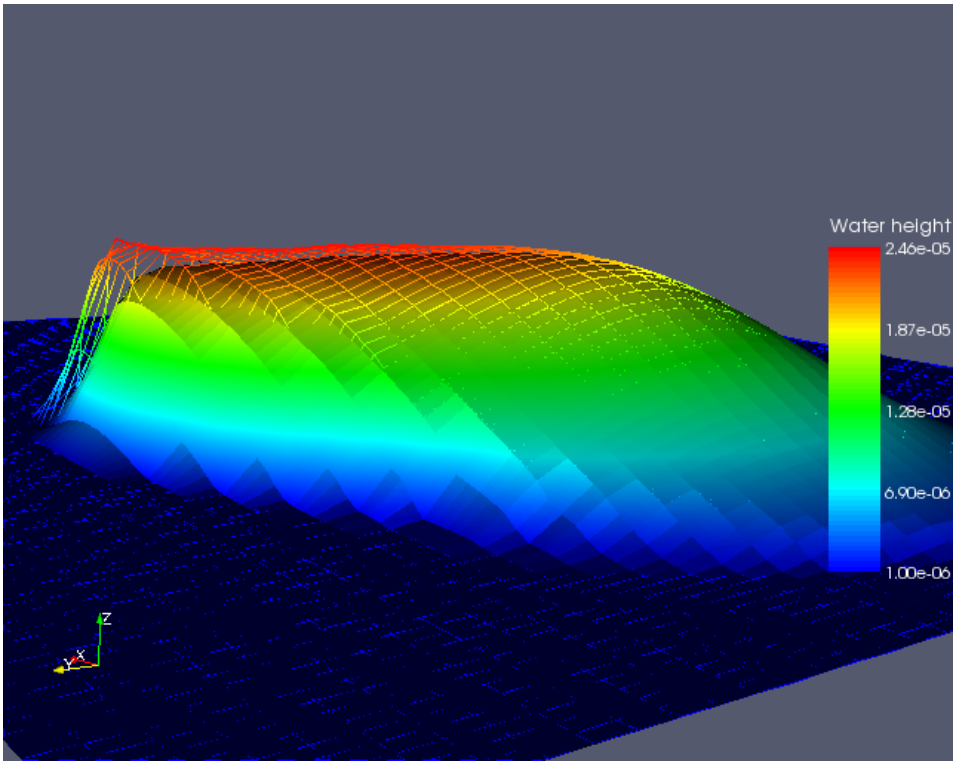

Figure 5.10: CloseView

The difference in water height in the equilibrium region can be explained with Figure 5.11. This time the upwind result is plotted on the grid and the high resolution method is represented as a plain surface. The view is from the top. With the additional dimension we can observe a difference on the lateral boundaries of the advancing front. In the upwind simulation the water film spreads more over the domain. The upwind scheme is naturally very diffusive and cannot cope with the sharpness of the front, both on the sides and at the advancing front. Naturally both results are compared after the same lapse of time and with the same initial conditions so the same amount or mass of water is present in the two simulations. As in the upwind scenario the water spreads more over the domain, this results in a slightly lower equilibrium height.

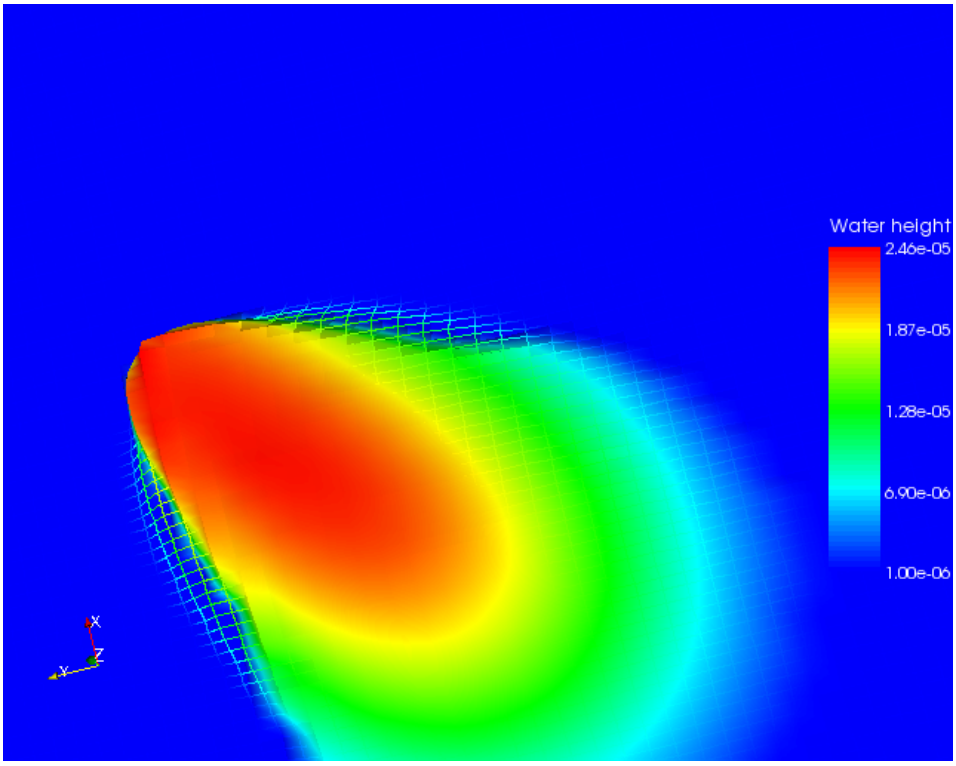

Figure 5.11: Flat plate 3d: Difference in water height. High resolution in plain, first-order rpresented on the grid

After a longer exposure time, the water has reached the end of the domain and the sharp advancing front is not present. Like in the 2D case, the difference in the equilibrium height is less noticeable but the high resolution result is slightly higher. In figures 5.12 and 5.13 we have a side and top view of the water film after several seconds, the water film modeled with the first-order method is represented in white opaque. We can see that the only difference occurs on each side of the water film. Again the upwind method has spread the water over a wider region while the high resolution method has kept the sharp structure of the water film.

Concerning the ice accretion the difference between the two solvers is reasonably small. In Figure 5.14 we show the ice height obtained after 12 seconds of exposure time. The

first-order results are in white while the higher order method is in color. We can see little difference in the impinging water zone, with an ice shape reflecting the Gaussian shape of the collection efficiency. Where the water has spread on the domain we can see that the upwind method predicts ice in a wider region than the high resolution method. Similarly to the water film, the ice layer obtained with the higher order method is sharper.

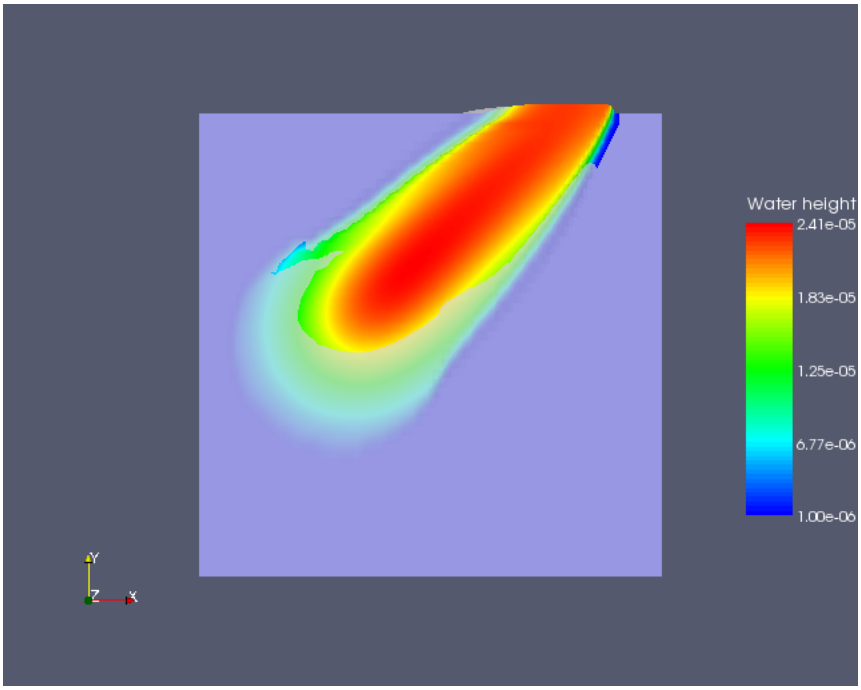

Figure 5.12: Flat Case: Water height, top view

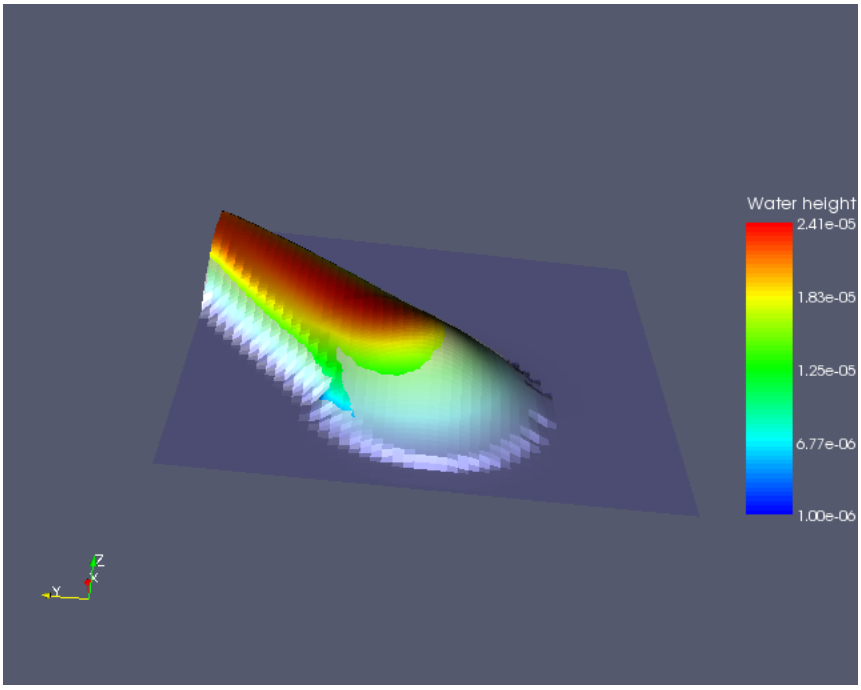

Figure 5.13: Flat Case: Water height, side view

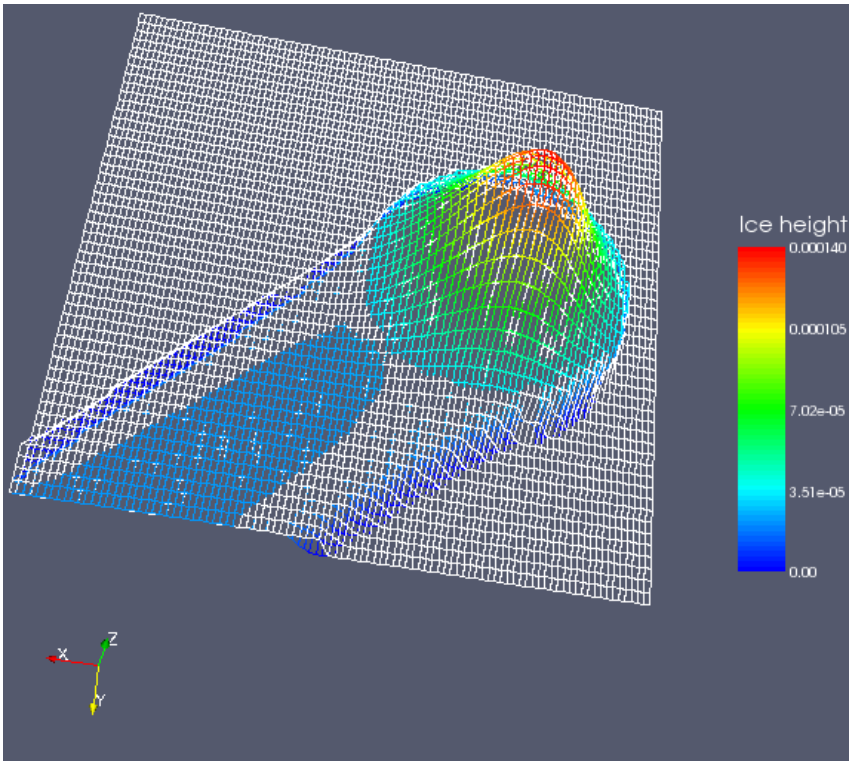

Figure 5.14: Flat case: Ice height comparison at 12 sec

In the following figures another comparison of ice height is made between the first-order upwind method and the high resolution method.

Figure 5.15 shows both method's prediction, side to side, after 6.5 seconds of exposure time. Both methods agree in the impinging droplet zone, the same maximum ice height is predicted. The ice in the upwind simulation has covered a larger area, and at the front where the ice is thinner, the high resolution method shows less ice accretion. The ice contours plotted in Figure 5.16 confirm this conclusion.

After a longer exposure time, Figures5.17 and 5.18, the difference is still visible. The ice extent in the high resolution case is more narrow.

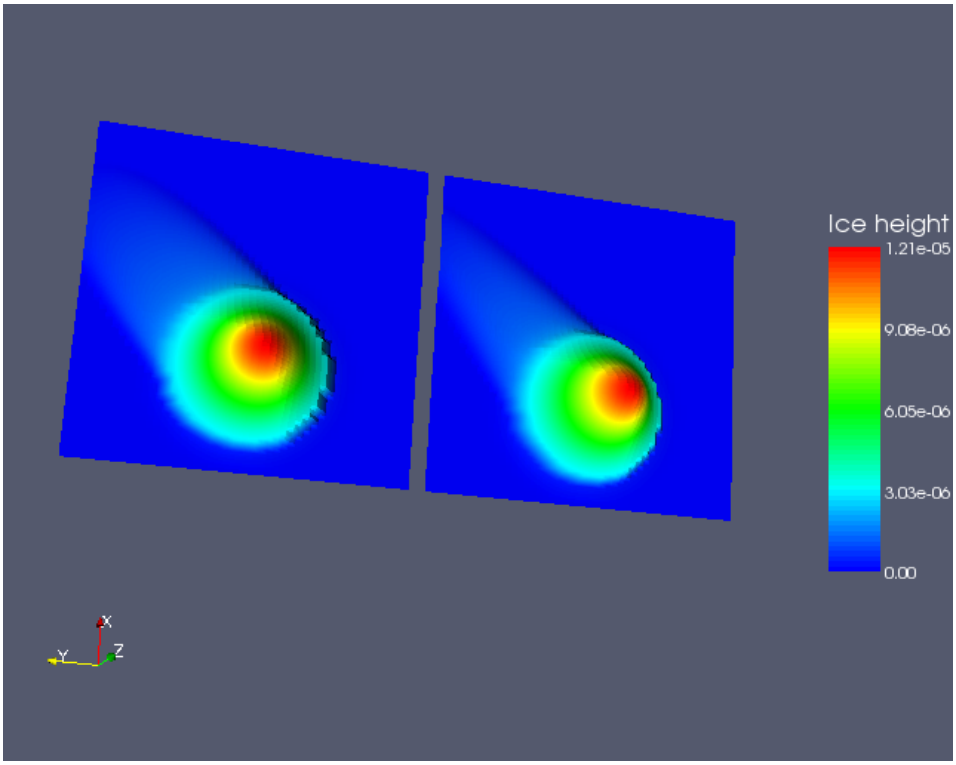

Figure 5.15: Ice height at 6.5 sec, upwind (left) high resolution (right)

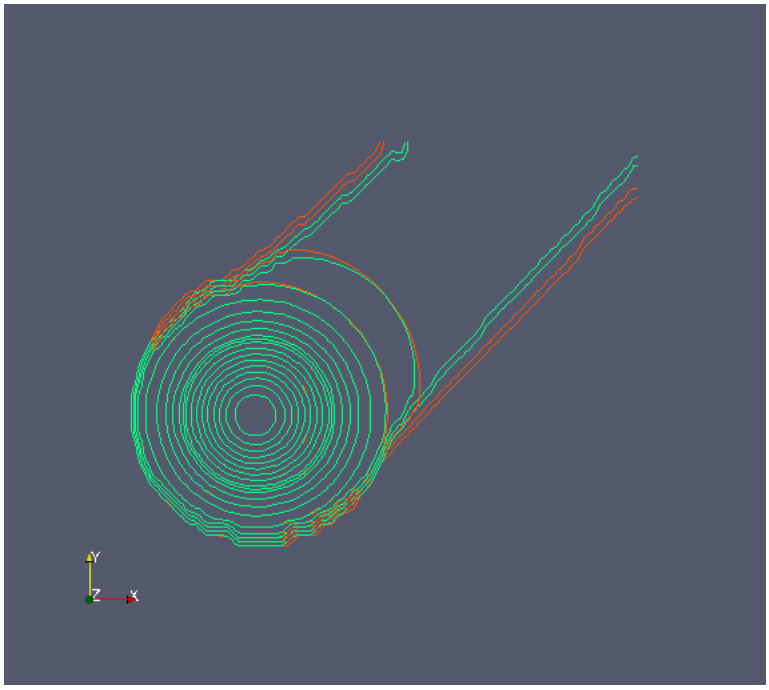

Figure 5.16: Ice contours at 6.5 sec, upwind (red) and high resolution (green)

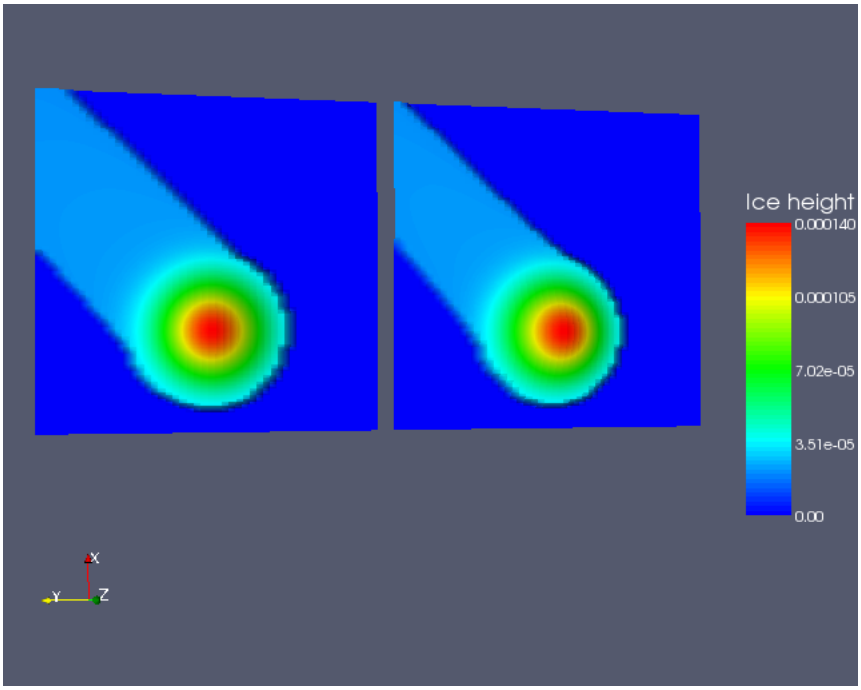

Figure 5.17: Ice height at 12 sec, upwind (left) high resolution (right)

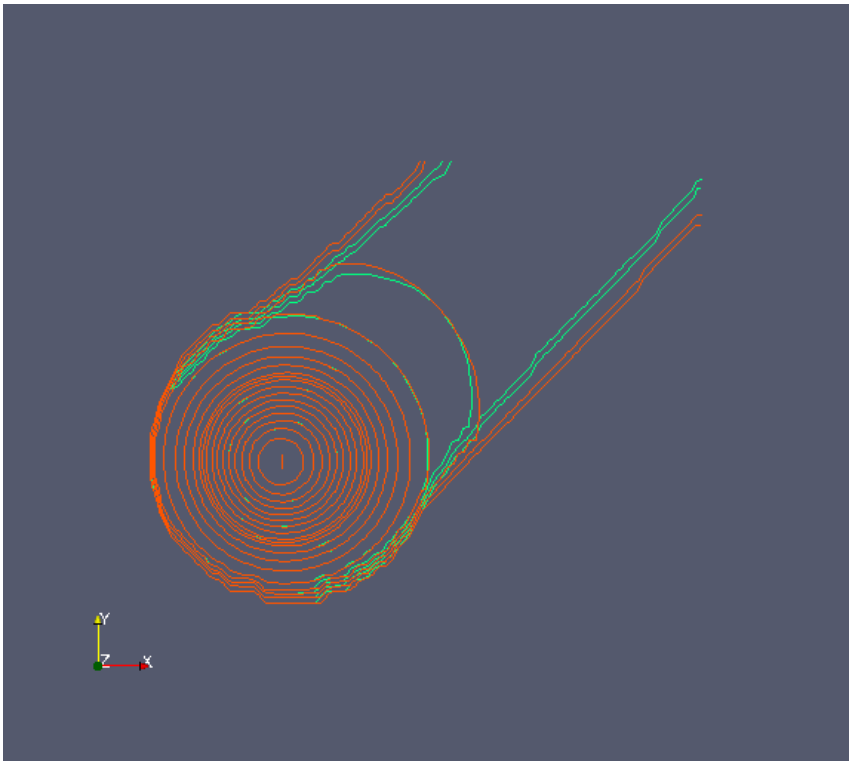

Figure 5.18: Ice contours at 12 sec, upwind (red) and high resolution (green)

The difference in ice prediction by the two solvers is a direct consequence of the difference of resolution in the water film. The diffusive upwind scheme results in more spreading of the water, thus a larger area of the domain is covered by ice. The fact that the equilibrium (water film) height is also slightly higher in the high resolution method results in less ice accretion.

Below we show the results obtained on two classical ice accretion tests with more physically realistic conditions, first on a NACA0012 then a cylinder.

5.3 Water and Ice Growth on an Airfoil

The test case presented in this section is standard in the icing community. Due to its simple geometry, the NACA0012 which is a symmetric airfoil, has been used widely in

the icing community to study icing in real conditions. Here we only consider and discuss results obtained from MAGNUM the ice growth and water flow module of ICECREMO2. The catch, shear stress and heat transfer coefficient have already been computed in the two other modules, Cornetto and Ripple. This test is referred in the NATO/RTO validation exercise [28] as the c17 test case. This corresponds to a glaze ice accretion scenario with a temperature of $T = 266K$ at an angle of attack $\alpha = 3\,\mathrm{deg}$.

All following pictures present a comparison between upwind and high resolution methods for the water film and ice growth simulation. For convenience we plot the results on an unfolded surface.

Figure 5.19 presents the water layer after one second of exposure time under these icing conditions.

The main difference between the two discretisations is at the stagnation region. As depicted in the previous chapter, this is a region of low velocity and flow separation. The upwind scheme does not perform well in this region. The advantage of the high resolution method, here is its central discretisation, due to the Lax-Wendroff scheme. The result is that slightly less water is predicted to flow in the lower part of the airfoil. It is also worth noticing that although the front part is sharper with the high resolution method no peak has formed on the advancing front.

Figure 5.20 represents the ice thickness after only one second of exposure time. Although the ice is very thin, it has already taken the double horn pattern typical of glaze ice accretion in these conditions. The main observation in this figure being that the high resolution method predicts less ice over the region around the stagnation line. The two methods agree well on the upper and lower part of the wing.

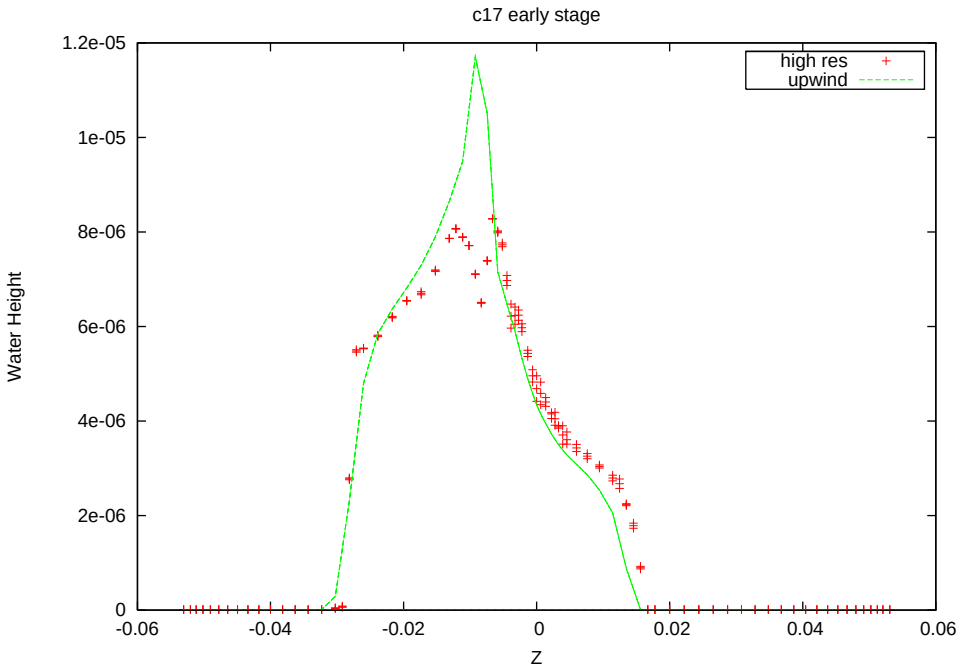

Figure 5.19: NACA0012, water film after 1 sec

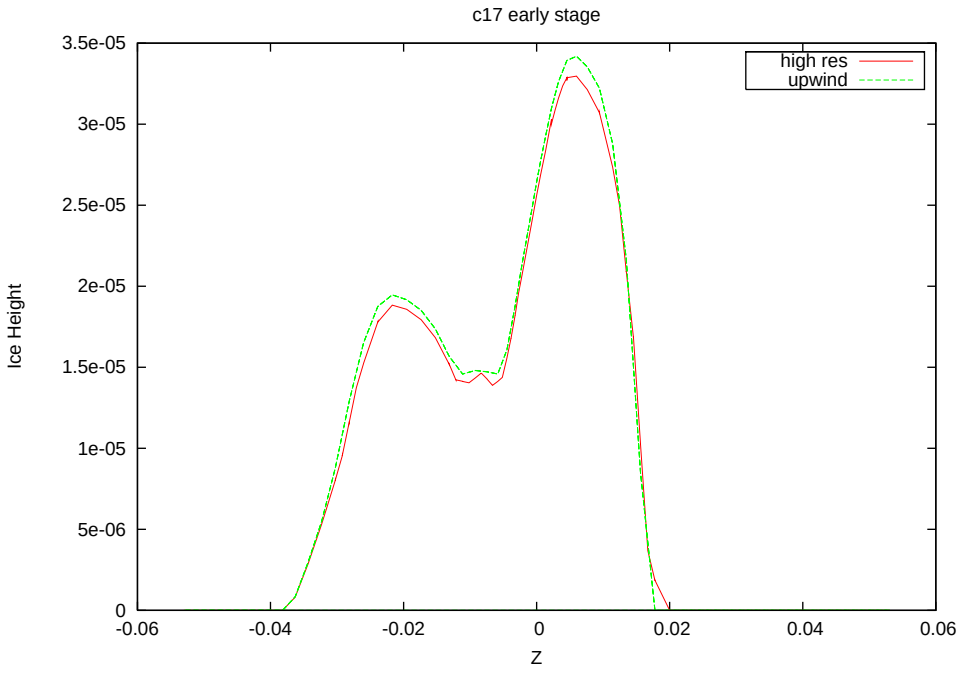

Figure 5.20: NACA0012, ice thickness after 1 sec

Figures 5.21 and 5.22 show respectively water and ice thickness after six seconds of

exposure time. In both case the water film has reached a steady state. We can see that even in the high resolution case no peak has formed at the advancing front, and compared to Figure 5.19, the water film has not progressed significantly towards the trailing edge. The freezing rate is high enough to prevent the water from spreading and piling up at the front.

The difference in ice thickness is now on the upper and lower parts of the airfoil. No difference is visible at the stagnation region. On the upper part, more ice is predicted with the high resolution method and the ice also reaches a higher part of the wing. However, the high resolution method predicts less ice than the first-order upwind solver on the lower part of the wing.

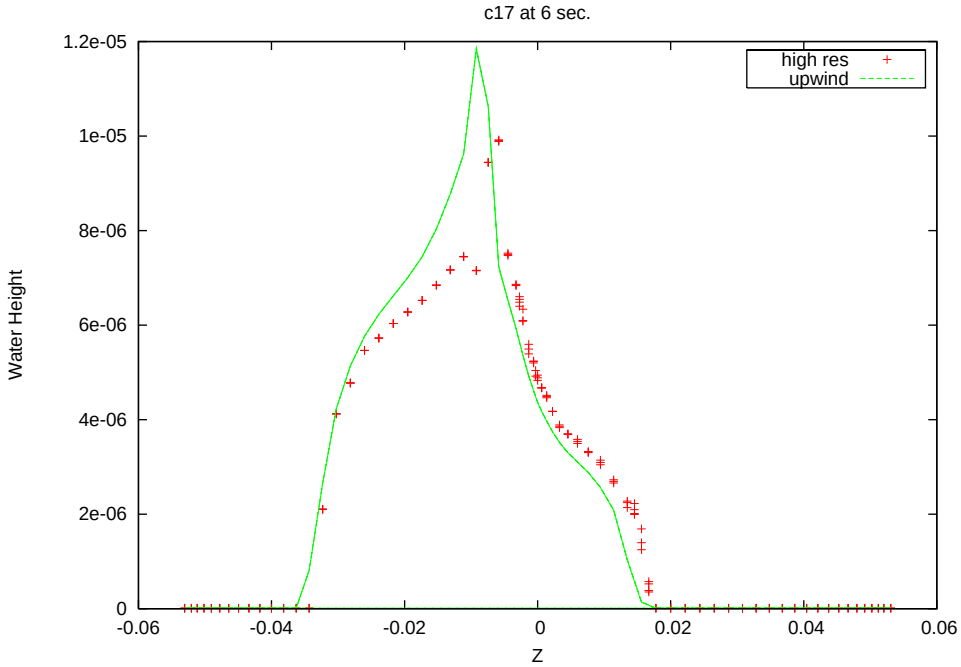

Figure 5.21: NACA0012, water film after 6 sec

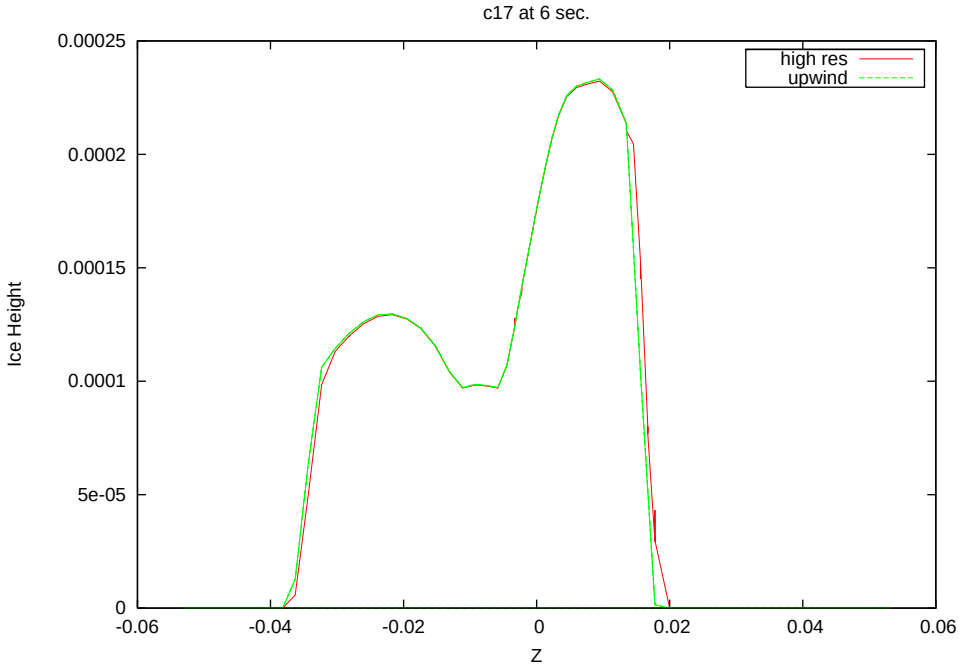

Figure 5.22: NACA0012, ice thickness after 6 sec

After fifty seconds, we can see in Figure 5.23 that the water film has not evolved much. The difference in ice prediction is a bit more clear in Figure 5.24. Still the same observations can be made: more ice on the upper part of the airfoil and less on the lower part with a high resolution methods.

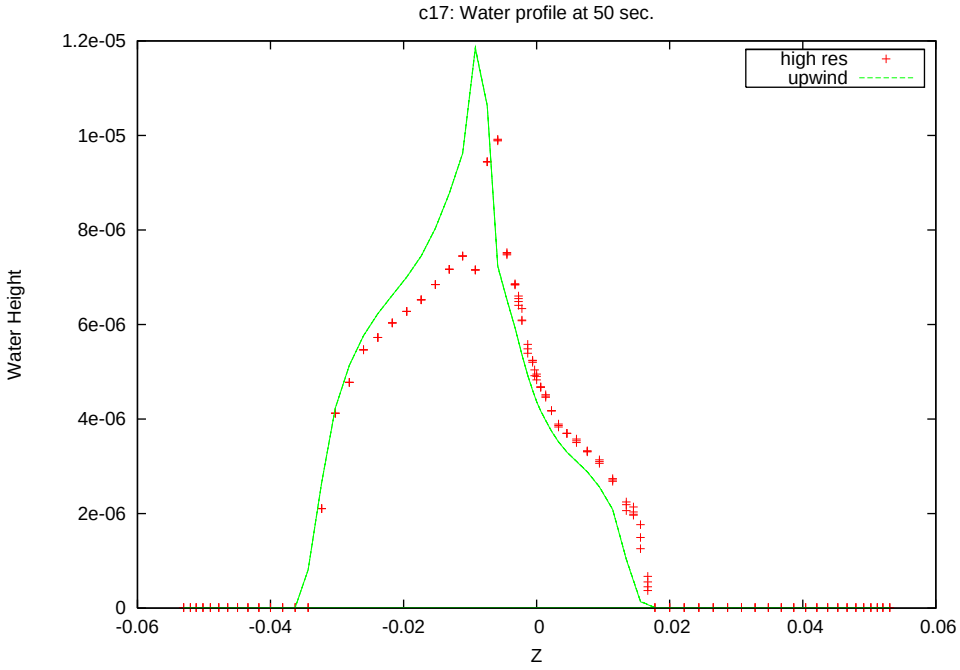

Figure 5.23: C17, water film after 50 sec

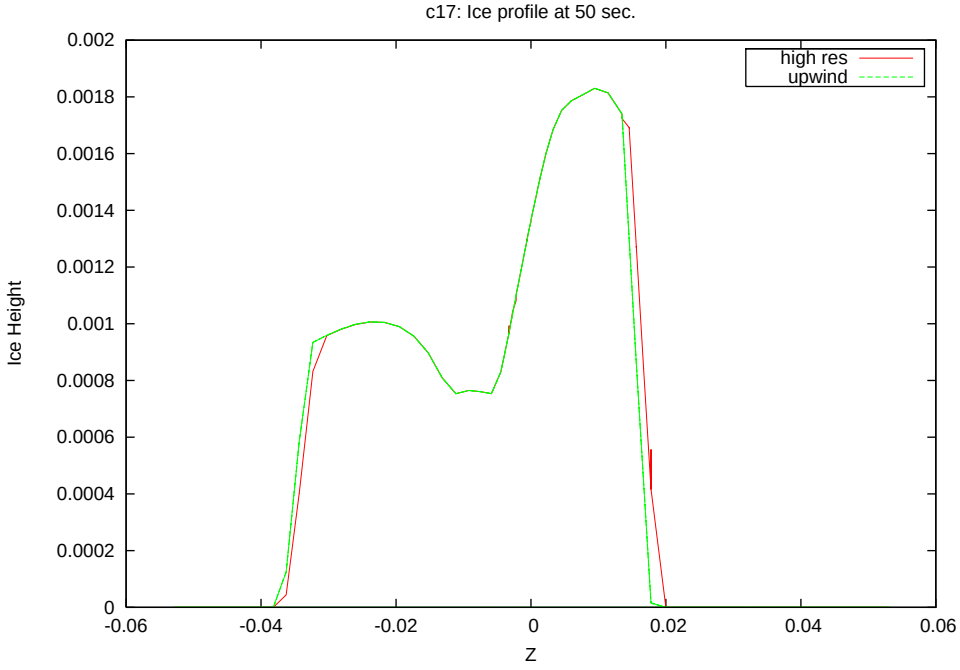

Figure 5.24: NACA0012, ice thickness after 50 sec

Figures 5.24 and 5.25 represent the same ice profile. On the second one, we show the

ice growth on the airfoil. The coordinates have been scaled by the chord $C = 0.914m$. Again after 50 seconds of exposure time only little differences can be observed between the two resolution methods. Only a small shift of the ice towards the upper part of the airfoil can be observed (Figures 5.26 and 5.27).

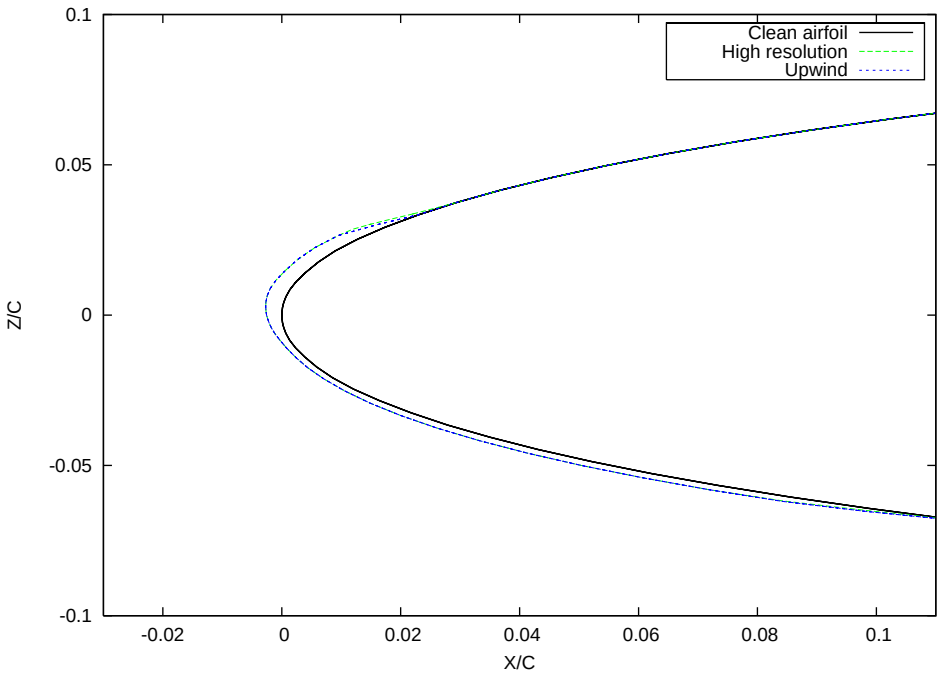

Figure 5.25: Ice profile on a NACA0012 airfoil after 50 seconds.

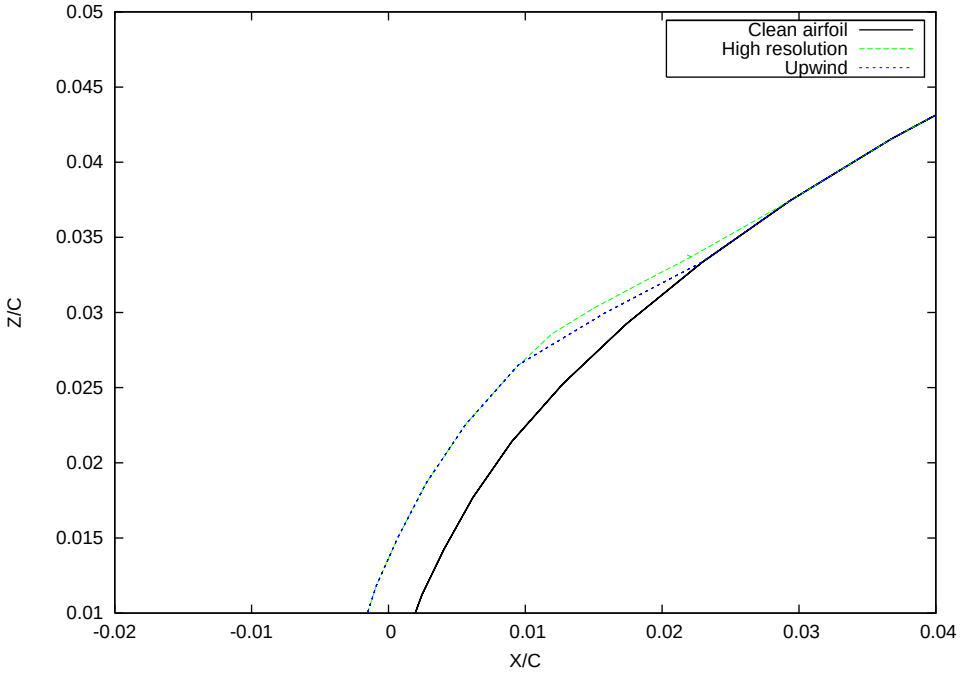

Figure 5.26: Difference of ice on the upper part of the airfoil

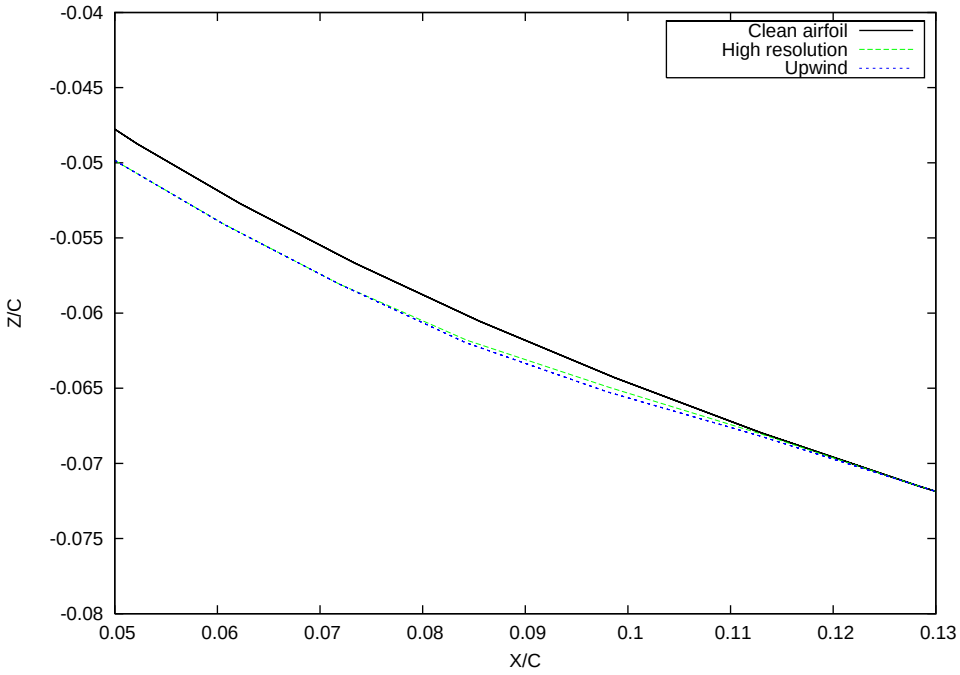

Figure 5.27: Difference of ice on the lower part of the airfoil

5.3.1 Different refinement criteria

A typical icing simulation last several minutes. We have seen in the two previous simulations that the time for the water film to reach a steady state was of the order of 10 seconds. In this view it seems rather inconsistent to carry on grid refinement with respect to the water film after it has reached its steady state.
First of all, the criterion defined in the previous chapter to follow the advancing front would continue to point the grid refinement to the same region where the gradient of water height is high, not bringing more resolution to it. Secondly as the water is in steady state it is not necessary to refine as often as when we were following the front. More importantly the necessity for derefining the grid is gone as the water film is not moving anymore.
For these reasons we have changed the algorithm for the grid refinement so it would be more suitable for ice accretion simulation.

After a given exposure time the error estimator switches to take into account the ice layer. Two criteria have currently been defined: one is based on the gradient of the ice height, the second one on the curvature. The curvature is basically the second derivative of the ice height and will point to a region where the change in the gradient of the ice height is high. The 'switch' time is at the moment set empirically in the code and is of the order of 10 seconds. This would depend basically on the speed of the run-back water, the temperature and the size of the domain. In Figure 5.28 we compare the ice profile obtained with different criteria. The line labelled 'high resolution method' uses the criterion by default in Icecremo2 which is gradient based. The 'second criterion' uses the curvature of the ice layer.

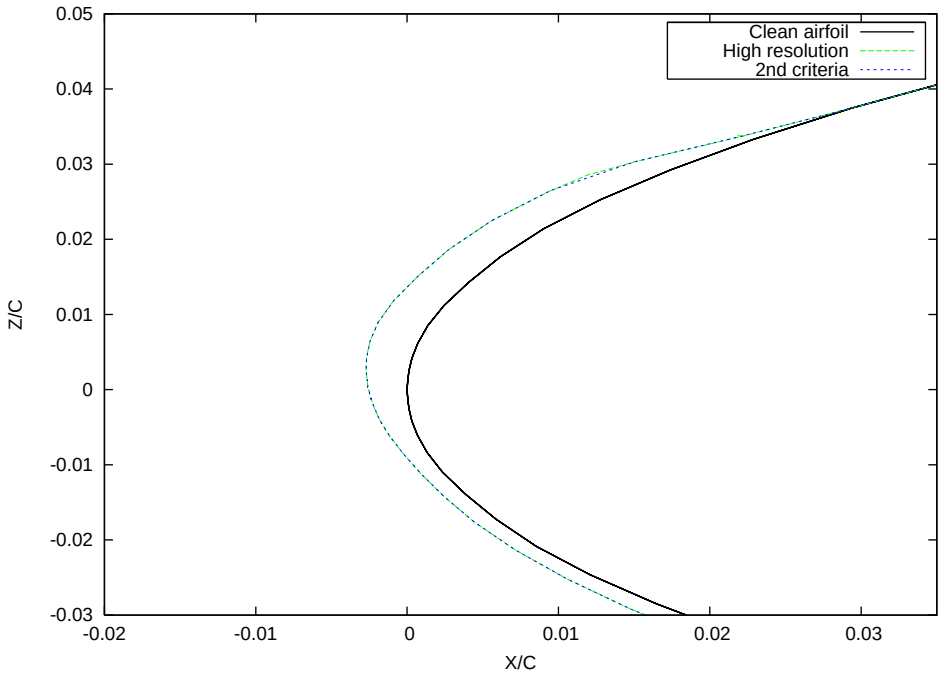

Figure 5.28: Different refinement criteria.

The difference in the two methods is very small. Most of all because the number of grid points added is not a large one, only 10% of the cells are refined in this simulation. Secondly, during refinement, the data are linearly interpolated, materials like water and ice are conserved but parameters like temperature, shear, etc. are kept constant. This means that the grid refinement with respect to the ice will not affect the ice growth directly. But instead, as we will see in the next section, refining the grid with respect to the ice can be useful in a multi-step procedure. Taking this last results into account we have also developped a 'reduced model' which significantly improves the computational performances with reasonable accuracy.

5.3.2 Alternative Time Stepping

During the different experiments and the investigation of the effect of mesh refinement on the ice accretion it can be noticed that once the steady state of the water film is reached,

no improvement could be achieved with refinement. Refinement with respect to the water film becomes unnecessary and refinement with respect to the ice has only a meaning in a multi-stepping calculations. Carrying the calculation with a time step restriction based on the CFL number makes little sense once the water film has reached its steady state. During a loop in the solver MAGNUM all external data such as heat transfer and shear stress are kept constant. The ice growth rate $\frac{\partial b}{\partial t}$ is mainly dependent of the water and ice height. If the water height reaches a steady state, $\frac{\partial b}{\partial t}$ will only vary in time as the ice height B is increasing. With these thoughts, an experiment has been performed in order to test a 'reduced model' once the steady state of the water film has been reached. The NACA0012 test case is used under glaze ice conditions. The first ten seconds of the simulation the normal model is run with high resolution method and refinement for the water film. After ten seconds of exposure time, the water height profile is explicitely stored and will remain constant for the rest of the simulation. A bigger time step can then be chosen. The only restriction to the time step is the maximum cell capacity, the maximum amount of ice that the cell can contain given a constant water height. The following condition is used:

$$h - \frac{\rho_i}{\rho_w}\frac{\partial B}{\partial t} * \Delta t \geq 0 \tag{5.3}$$

which gives:

$$\Delta t \leq \frac{h}{\frac{\partial B}{\partial t}}\frac{\rho_w}{\rho_i} \tag{5.4}$$

This condition is satisfied for each cell which is equivalent to take the minimum time step satisfying 5.4. In Figure 5.29 a comparison is made after 50 seconds of exposure time between the results obtained with the normal and reduced model.

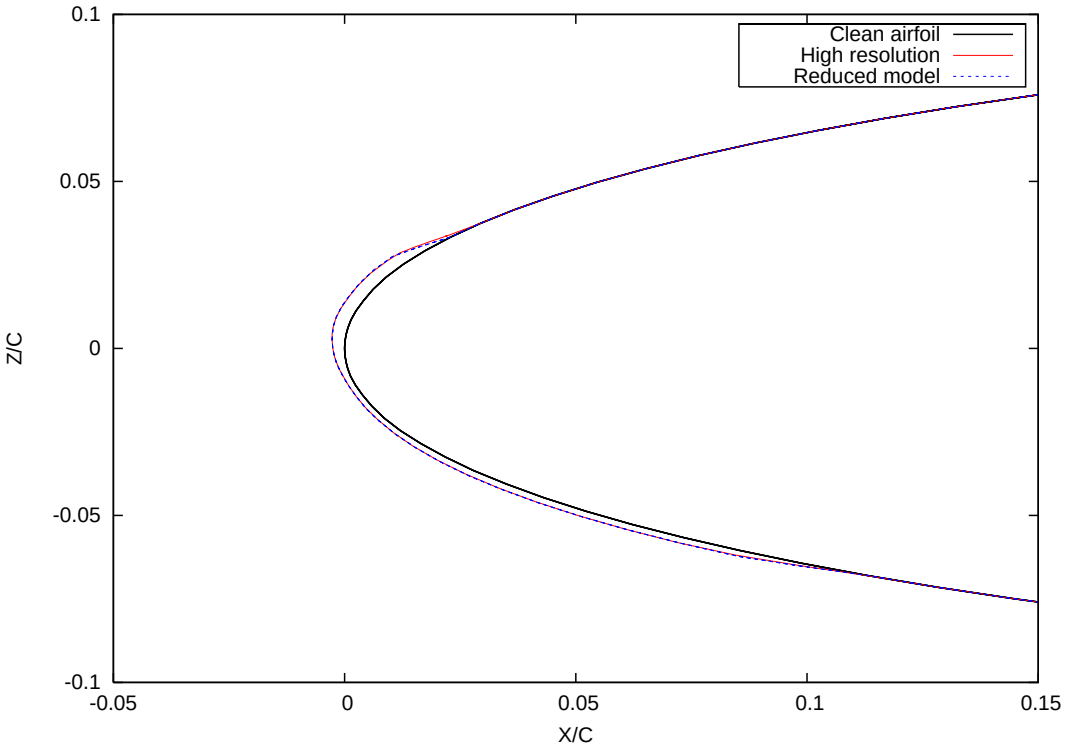

Figure 5.29: NACA0012: Comparison with a reduced model

It can be seen that the difference is small. Again the only area where a difference is visible is at the interface between ice and substrate. This is mainly because of the assumption that the steady state is reached; the water film varies nevertheless a bit over time.

If the difference in accuracy in small, the gain in computing time is huge. For this simple simulation, the reduced model was approximately 20 times faster. With a more complex test case where the number of cell is increased and the size of cells smaller the improvement would be even more considerable.

5.4 Icing on a cylinder

5.4.1 Impact of the droplets size

The two test cases presented in this section have also been part of the NATO/RTO validation exercise [28]. They correspond to a glaze ice accretion scenario on a small cylinder of diameter $C = 63.5mm$ at a temperature $T = 270K$.

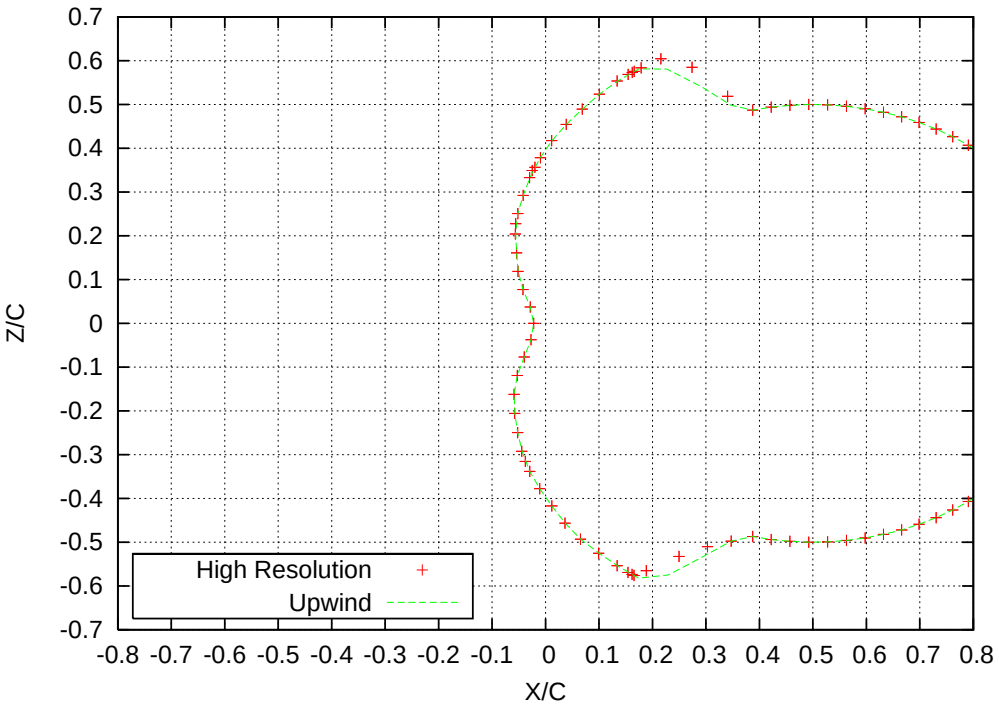

Figure 5.30: Glaze ice accretion on a cylinder with Super-cooled Large Droplets at $T = 270K$.

The incoming water reaches the cylinder with no angle and a free stream velocity $V = 77.2m/s$. Two scenari are considered. The first one is referred to as case O5 and corresponds to a small droplet simulation. The droplets diameter is $d = 18\mu m$ and the liquid water content is $LWC = 0.44g/m^3$. The second test is the case O6 and corresponds to a Super-cooled Large Droplet (SLD) simulation. The diameter of the droplets is $d = 100\mu m$ and the liquid water content $0.37g/m^3$.

In Figure 5.30 we compare the results obtained in the large droplet scenario with low and high order discretisation after five minutes and thirty seconds.

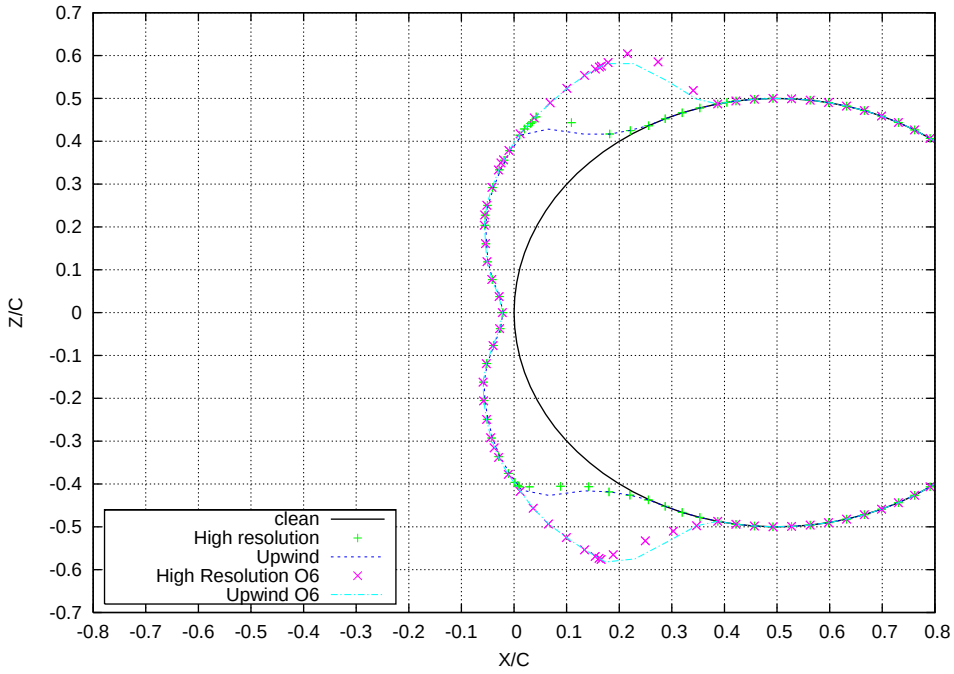

Figure 5.31: Glaze ice accretion on a cylinder: solutions of first-order and higher order method with two sizes of droplets.

We can see that the main difference in the two solutions is at the interface between the ice layer and the substrate, at the bottom and top part of the cylinder. In the upper part the high resolution method predicts more ice whereas in the lower part it does predict

slightly less ice than the upwind method. This can be explained as in the previous section by the shift of water around the impinging zone. More water reaches the upper part of the cylinder with the high resolution method. In Figure 5.31 we show results of both O5 and O6 test case obtained with the high resolution and first-order method. First of all in the Super-cooled Large Droplet scenario we can notice that the ice layer extends further. As more water is present on the substrate, at temperature close to zero, the water film progresses much further on the surface before freezing, exactly as shown in the first section of this chapter on a flat plate case. Secondly, with a close-up view in Figures 5.32 and 5.33, we can see that again the main difference between first-order and higher order method is only at the interface between ice and substrate. The interface is sharper with the high resolution method with a slightly larger difference in the large droplet scenario.

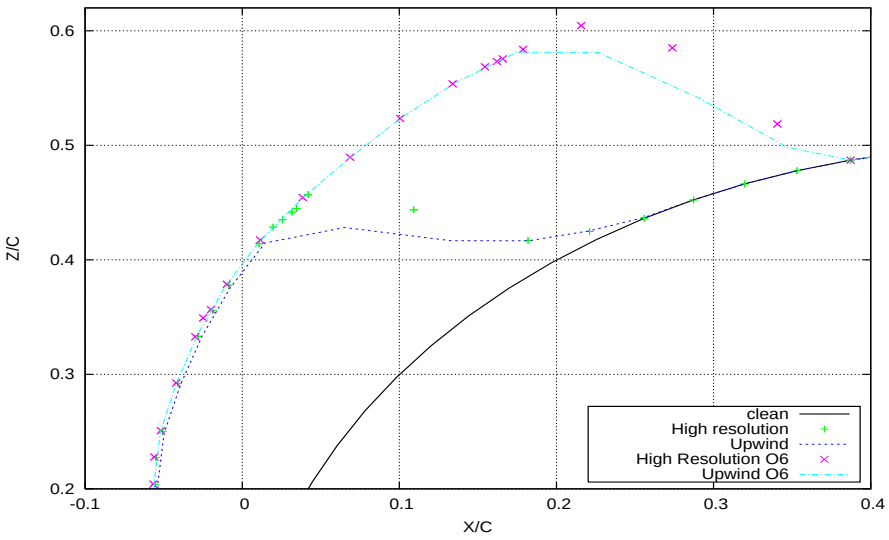

Figure 5.32: Difference in the upper part of the cylinder.

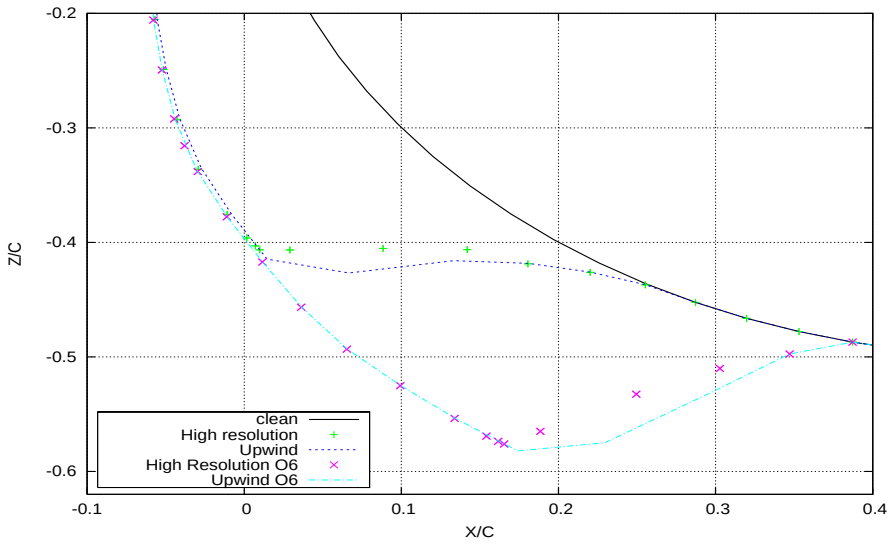

Figure 5.33: Difference in the lower part of the cylinder.

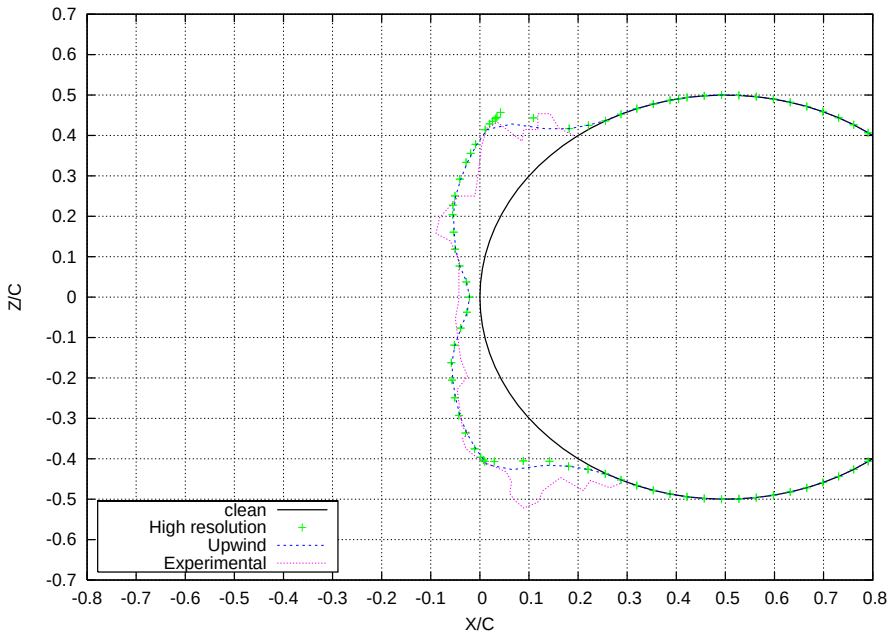

Figure 5.34: Case O5: Comparison with experimental study.

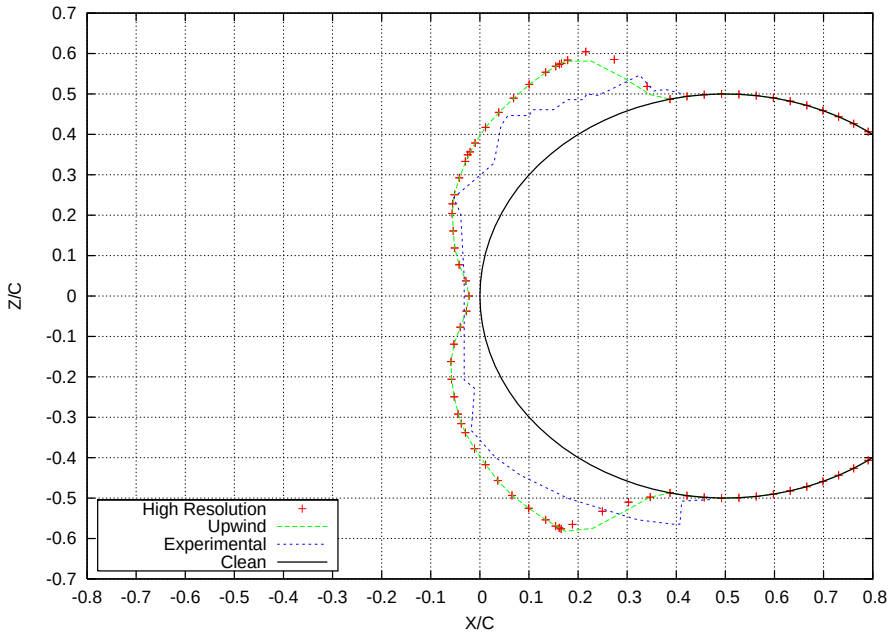

Figure 5.35: Case O6: Comparison with experimental study.

In Figures 5.34 and 5.35 we compare these results with experimental data. The simulated ice shapes are still far from the experimental data. This is especially true for the large droplet simulation test which shows the importance of the water film in the ice accretion calculation.

All the results performed so far have been performed in a single-step procedure where icing parameters remain constant during the whole calculation. The following section will describe simulations performed with a periodical update of the flow solution and associated parameters. This approach is called multi-stepping and has proven to be very useful in ice accretion modelling [20].

5.4.2 Results with multi-step

Multi-stepping is a calculation method which consists in updating the flow variables at every given 'step'. A full analysis of this procedure for ice accretion is done in [20]. A flow chart describing this procedure also taken from Verdin's PhD thesis is given in appendix B. Basically in a classic icing simulation, the flow variables like, air velocities, catch, shear stress and heat transfer coefficient are calculated outside the solver module for water and ice growth.

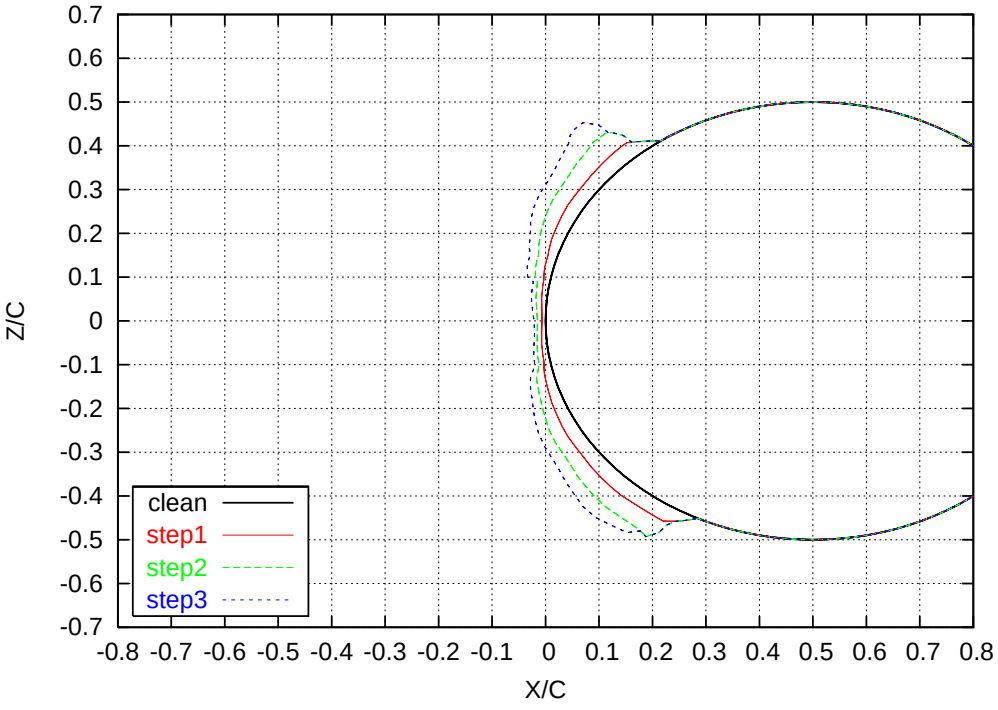

Figure 5.36: Case O5: Results of a 3-steps procedure, $t = 330s$.

These variables are then fixed in time during the rest of the calculation process. But the growth of the ice layer might significantly affect the airflow around the domain resulting in different velocity profile, catch, shear stress and heat transfer coefficient. The multi-step will consist in dividing the simulation time in several steps and after each step re-meshing the surface including the ice growth before performing a new flow calculation. New values of icing parameters may be calculated afterwards. These steps are not necessary fixed in time and will depend on a defined criterion, see [20]. One of these criteria could be based on the water film.

In Figure 5.36 we show the evolution of the ice height after three steps of 110 seconds. During these computations, the high resolution method developed in this thesis has been used and grid refinement has been performed. The mesh adaptivity has been done with the error estimator developed in Chapter IV during the first ten seconds of each step. Then refinement with respect to the gradient of the ice height has been performed until the end of the step.

In Figure 5.37 we show the evolution of the catch during these three steps. Because of the multi-step, the profile from step 2 and 3 are actually plotted on the ice layer which results in a less smooth profile for the last two steps. From the second step we can see the appearance of two peaks on both side of $Z = 0$.

More on the third step we can notice that some droplets hit the domain at the extremities of the ice layer, around $Z = +-0.03$.

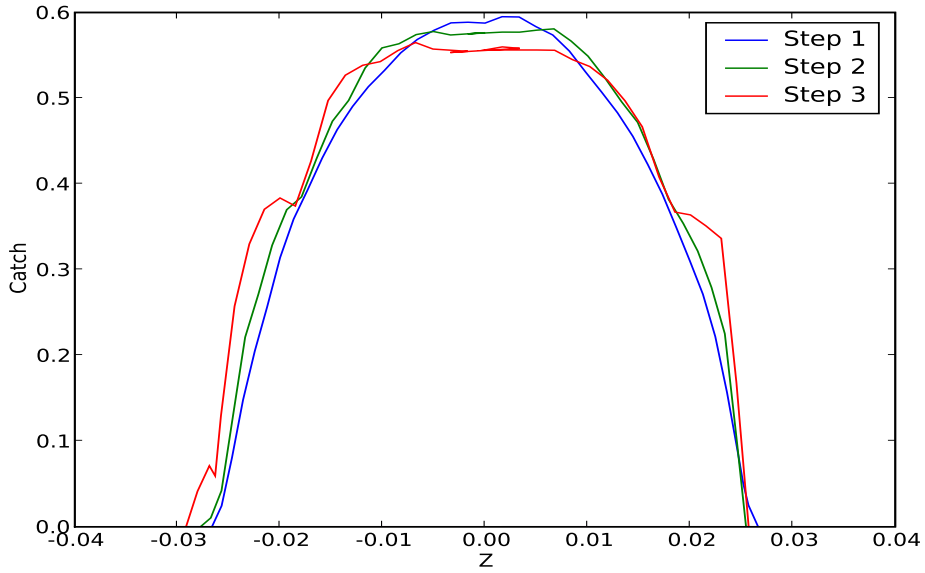

Figure 5.37: Case O5: Catch profile at different step.

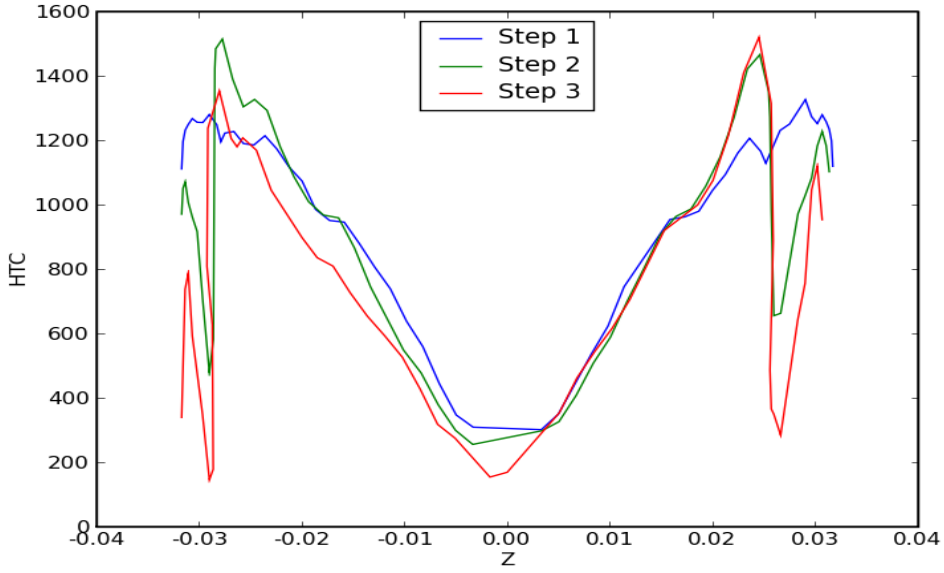

Figure 5.38: Case O5: HTC profile at different step.

In Figure 5.38 we show the evolution of the heat transfer coefficient over the three steps. For conveniency we only show the heat transfer on the front part of the cylinder for $X < 0.03175m$. We can see that the HTC decreases over time on the lower part of the cylinder $Z < O$ whereas it increases slightly on the upper part of the cylinder for $Z > 0$. In Figures 5.41 and 5.42 we show respectively the water and ice height at each step on an unfolded surface. In the water layer profile we can see that the main difference between the first and second step is around $Z = 0$. This is mainly due to the restart and the change in catch and ice height. The water profile after the third step is different from the two other steps mainly in the lower part of the cylinder. More water is present in this region in the last step of the simulation. The reason for this is that the water film is on the top of the ice layer. As shown in Figure 5.42, the the ice height presents a peak in the lower region of the cylinder. More water is then catched by the iced surface in this region and this water will flow down further in the lower region. The water flowing back in the lower region is due to the shear stress and also to gravity effects.

We can have a better understanding of what is happenning to the outside flow by observing the shear stress. In Figure 5.39 we can see the shear stress applied in Step 3 of the multi-step procedure. This shear is applied throughout the last step so as effectively been calculated on the ice surface of step 2. We can see that the only place where the shear stress has been disrupted is at the limit of the ice surface, the interface between ice and substrate. By taking a closer look in this region, Figure 5.40, we can actually see a change in the direction of the shear stress. The ice layer disrupts the flow and provoques a detachment just behind the interface ice-substrate. The flow reattaches soon after leaving only a small region affected by this change. The peaks at the extremities in the HTC (Figures 5.38) as well as in the water layer (Figure 5.41) can be explain by the behaviour of the airflow in this regions.

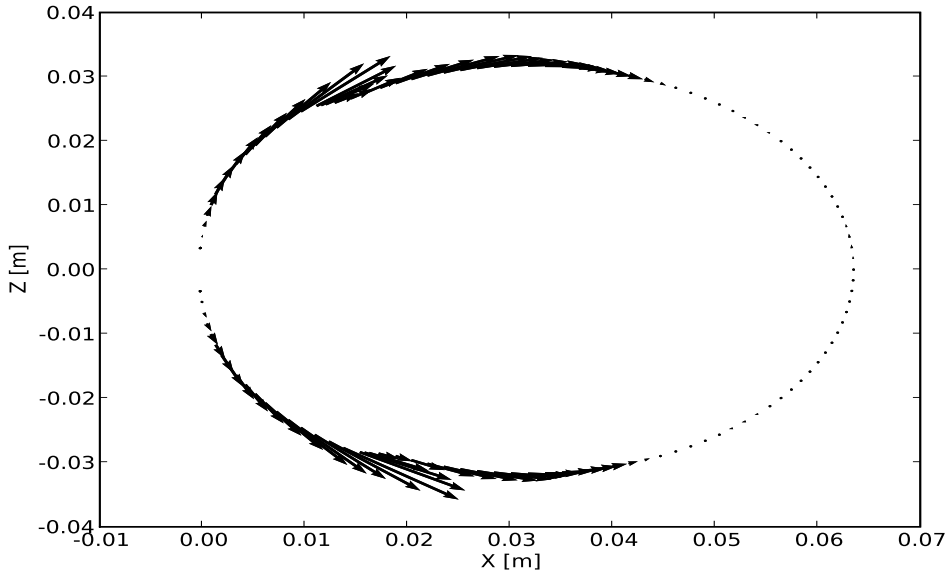

Figure 5.39: Case O5: Shear Stress profile for step 3.

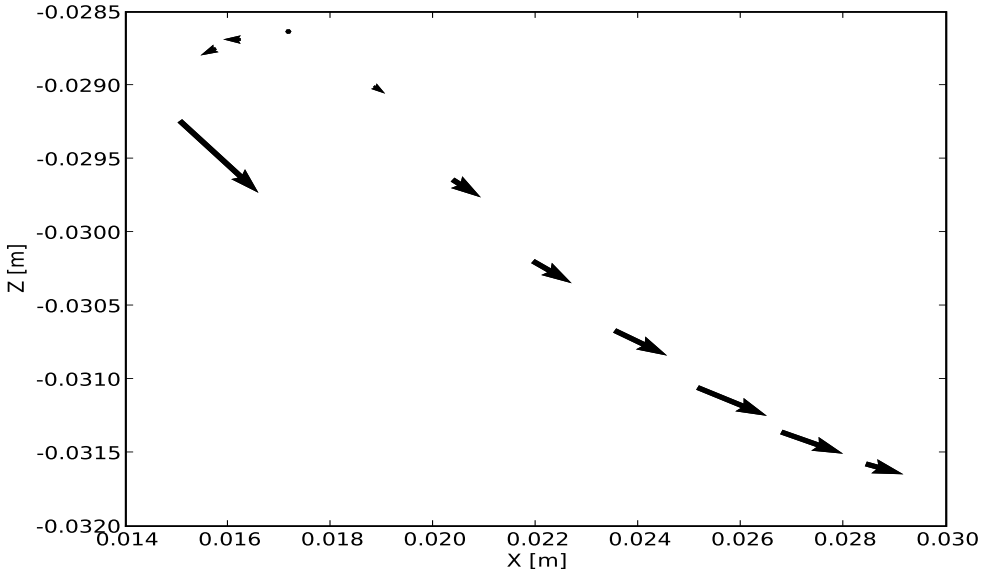

Figure 5.40: Case O5: Shear Stress profile for step 3:close-up view of the upper part of the cylinder at the interface ice/substrate. we clearly observe a change in the shear stress direction in this region.

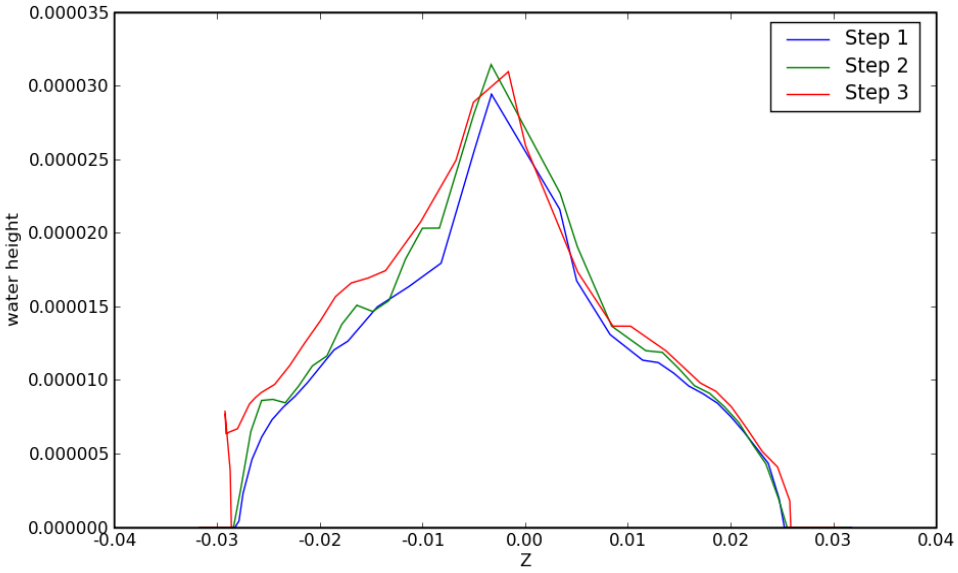

Figure 5.41: Case O5: Water height at different step.

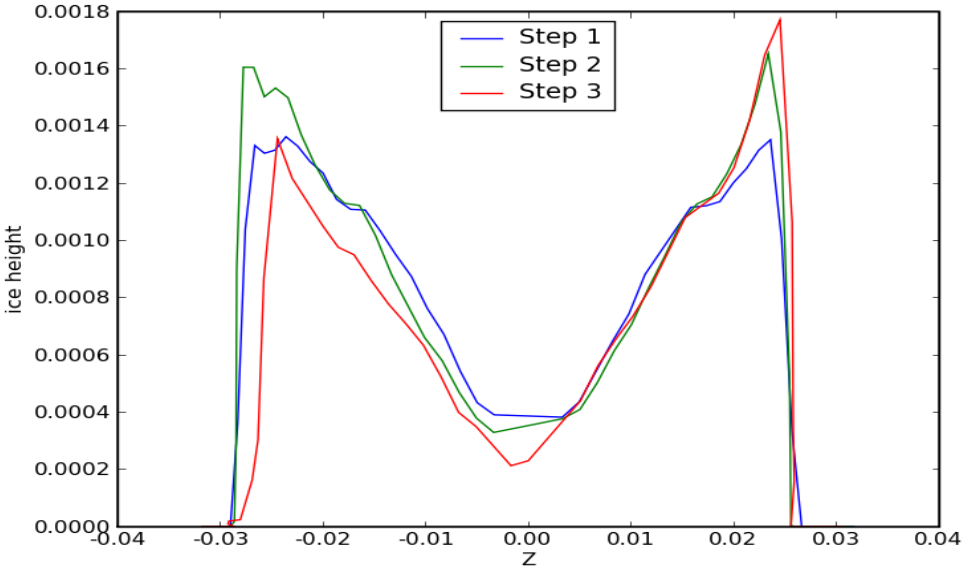

Figure 5.42: Case O5: Ice height at different step.

This change in the water profile is reflected in the ice profile. On Figure 5.42, we can notice a difference again in the lower part of the cylinder, for $Z < 0$, the ice growth has reduced during the last step of the simulation. As the water film height as increased. More, we can also notice that the ice continues to reach further down the surface, even after 220 seconds.

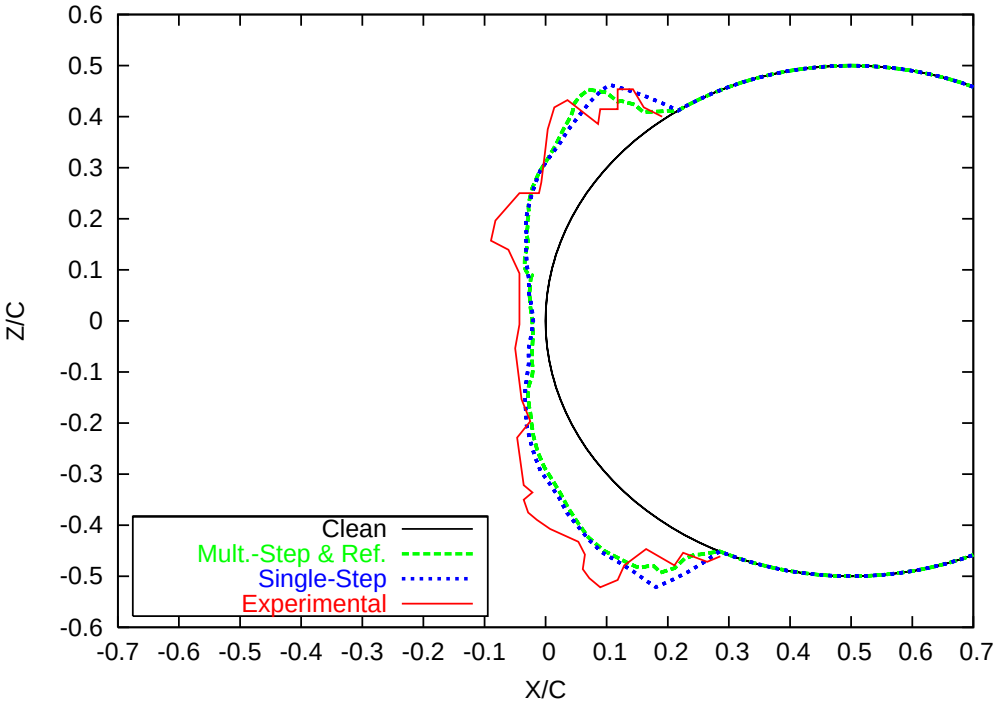

Figure 5.43: Case O5:Comparison with experimental data.

Finally in Figure 5.43 we compare the results with and without multi-step against experimental data. The main difference is again at the interface of the ice layer with the

substrate. A multi-stepping approach combined with a high resolution method seems to predict better the extent of the ice layer. Over the rest of the domain, a close view can tell that the high resolution/multi-step combination gives slightly less ice in the lower part of the cylinder and also a less smooth surface on the upper part.

5.5 conclusion

In this chapter we have studied the interaction between ice growth and the run-back water film in the particular case of glaze ice accretion. We have tried to assess whether the resolution of the water film could have a significant impact on the final ice shape. The high resolution method and the grid refinement strategy derived in the previous chapter allowed us to make such study.

Indeed we have shown on a simple flat test case that the resolution of the water film height did have an impact on the ice growth. We showed that the advantage of the high resolution method would be reduced as the temperature lowered. The milder temperature, the longer the water film would take to reach a steady state and the larger the impact on the ice accretion. We showed that the total water volume would become constant after a certain time and that this constant would be lower as the temperature is reduced. In three dimensions, we showed that the impact of the high resolution method was increased as a first-order method would diffuse in several directions; thus reducing the sharpness of the front and the equilibrium height and also spreading the water over a larger surface. A high resolution method for the water film will then predict less ice both in term of height and of coverage.

However the water and ice growth evolve at different time scales. We have seen that for more realistic and longer icing simulations the two discretisation methods would give similar results in most of the part of the domain. The main difference being at the

interface between the ice layer and the substrate. We asserted that the resolution of the water front would result in a local high in the water, reducing the rate at which the water front freezes. This, combined with a better resolution of the stagnation region in the NACA0012 test case would produce a shift of the ice layer towards the upper part of the airfoil. More ice on the top of the airfoil and less on the bottom compared to the results obtained with a first-order method. Because of this difference of time scale between water and ice we also proposed different refinement criteria taking into account the ice profile. Finally on a cylinder we showed the effect of the droplet size on the water film and ice growth. We combined the high resolution method and the grid refinement strategy with a multi-stepping approach allowing us to update the outside flow and icing parameters during the icing simulation. Only a three steps approach has been performed here but multi-stepping combined with grid refinement is the way forward as this would lead us to better accuracy.

Chapter 6

Conclusion

In the development of this thesis we have investigated the effect of the resolution of the water film on the ice accretion. The water film is governed by a complex non-linear,degenerate, partial differential equation. This represents a scalar conservation law with source term and this type of equations are notoriously difficult to solve. Their solutions are likely to develop singularities like discontinuities or shocks. The presence of these discontinuities makes it very challenging to solve numerically.

Solving the water and ice growth equation on unstructured grid is new. We present a finite volume formulation of the shock capturing scheme developed by Roe and Sweby. This scheme is second-order in space, free of oscillations and has been shown to be the most accurate for this equation on structured grid. The scheme is a linear combination of first-order upwind and second-order Lax-Wendroff scheme. The weighting of each scheme is defined by the Superbee limiter. For unstructured grids, the implementation of such a scheme is very difficult. Because of the data structure within which we were working, we only have access to two neighboring values at each cell interface or edge. The computation of the Superbee limiter requires information on a larger stencil. For the purpose of simplicity, efficiency and robustness, the missing information is evaluated using a gradient

interpolation to obtain data on what we called 'the virtual cell'.

The first results have been presented in two dimensions to highlight the effect of the different forces on the water film. A shear driven flow spreads over a dry surface with a shock at the interface between liquid and substrate. The liquid spreads as the wave front advances on the surface. Away from the front, the water reaches an equilibrium height. When gravity acts in the same direction as the shear stress, the speed of the wave front is higher and the liquids spreads faster. The equilibrium height is lower. If gravity is in the opposite direction to the shear stress, the water film is slowed down. When the angle of inclination is high, the global shape of the film is completely changed. The wave front becomes larger and forms a plateau. The rest of the liquid is separated from the plateau by an undercompressive shock which will slowly disappear as the water height increases. Generally surface tension only reduces the extent of the flow. These results are in accordance with those obtained on structured grid by Charpin and the global shape obtained for the water film is the same that those observed for Marangoni-driven flow.

Similar results have been obtained in three dimensions where the full structure of the water film can be observed. A simple rotating case has been considered showing the liquid spreading in the right direction with good feature at the front. Qualitatively the results agree with those found in the literature (see for example [76]). Such simple rotating case where not achievable within the original framework of ICECREMO2. The implementation of a stable higher order numerical scheme developed in this work made it possible and is a major step forward.

All these preliminary results show the accuracy of the method chosen to solve the water film equation and its robustness making it available for a considerable number of applications.

In the second part of this thesis we established a refinement strategy for adaptive

computations. Again adaptive mesh refinement in icing is new and the study done in this thesis is the first of its kind. Higher-order shock capturing scheme are, at most, first-order accurate near discontinuities. To avoid the oscillations of the higher order scheme caused by the dispersion around the discontinuity, a diffusive term is added through a first-order scheme via the flux limiter. Near a discontinuity the numerical scheme is then first-order while we achieve second-order accuracy elsewhere. The error of approximation is reduced directly by refining the computational mesh in the region of a sharp gradient. To detect the appropriate region to refine, an error estimator has been constructed using a double discretization. No significant additional computation is required for the error estimator as we used the difference between first-order and second-order schemes which are already computed at the cell interface (or edge). When possible, refinement is made in the direction perpendicular to the flux to make it more efficient. All grid to grid interpolation is mass conserving which keeps the entire method globally conservative which is of primary importance for this type of equation.

As the water spreads on the surface it is important to coarsen the grid when higher resolution is not needed anymore. This is done using a dual grid. The initial coarse grid is stored and when necessary, data are interpolated to this grid which can then be refined. The interpolation again conserves mass, the amount of water/ice on the child cells is added to the parent cell. Although a loss in the speed can be detected, the accuracy at the shock is quickly recovered. The final result is an adaptive calculation with a finer grid moving automatically as the water front advances. By comparison between coarse and fine grid calculations we observed that the adaptive computations save about 30% on CPU time and storage.

ICECREMO2 can simulate two types of ice accretion, rime and glaze ice. The first one happens under very cold conditions when the incoming droplets freeze 'instantaneously'

on contact with the solid surface. The second appears at milder temperatures, just below zero, when only a fraction of the liquid freezes and the rest forms a run-back film. Only glaze ice is considered in the third part of this thesis. We investigated the effect that a more accurate water film simulation has on the final ice shape prediction. This investigation has been performed through three basic test-cases: a flat plate, a cylinder and a NACA0012 wing. The last two are part of the software validation plan and results have been compared with experimental data. The three initial meshes are Cartesian grids, although some triangles can be present after refinement due to the way hanging nodes are treated. The main result coming out of these three tests, is that a better approximation of the wave front can reduce the size of the computed ice layer that appears during the first 15 seconds of the simulation. When the front is accurately modeled, the amount of water in a cell at the front is greater. The freezing factor on the very same cell is much lower and only a small part of the liquid is transformed to ice while a greater part of the liquid remains in the run-back film. Although this result appears to be significant, the impact on the final ice shape is small. The height of the ice layer after few seconds in these tests is less than a tenth of a millimeter whereas after a full exposure time the ice layer can be several millimeters thick. Water and ice evolve on different time scales, ice usually forms slowly while the water front moves quickly and either flows away from the substrate or freezes and disappears. However, the effect of the water front on the icing is accentuated when using multi-stepping calculations. This process which consists in restarting the calculation several time with an update of the flow conditions, mainly air speed, catch and heat transfer, benefits of the refinement; and after each step we observed another wave front on the water film which in its turn affects the ice formation.

We also developed a second refinement criterion taking into account the change in ice height, to reinforce the benefits of multi-stepping. This criteria has been combined with the first one. During the first seconds of the calculation the refinement is performed with

respect to the water film, i.e. at the front, then with respect to the ice on much larger time intervals, all of these through a multi-step calculations.

The numerical method presented in this thesis to solve the equation governing the water film and ice growth, is robust and gives good results on the different cases tested here. The numerical scheme has performed well in all test cases as long as the stability condition is respected. The refinement is simple and fully automatic. Several things can however be improved and remain to be investigated:

- The data structure for handling the computational grid and the corresponding data could be improved to support several levels of refinement and de-refinement. A tree structure would offer several advantages. The coarse grid would not have to be stored for coarsening, and more importantly data from the fine grid would be interpolated to the coarse grid only when the fine resolution is no longer required. The grid could be refined several times until a fixed level of error is reached.

- The implementation of the adaptivity only deals at the moment with quadrilaterals and triangles. Additional features are needed to adapt it on general grids.

- The impact of the accuracy of the water film on icing would certainly be accentuated with more complex flow conditions when the water film does not reach a pseudo-steady state. If the different forces are acting in different directions several wave fronts can be present, influencing the icing on more than one place. The same when rivulets formation is considered. If de-icing is performed, additional amounts of water coming from the melted ice would affect locally the shape of the liquid film.

- The surface of the ice in this investigation has always been considered perfectly smooth. Rime ice however can produce very rough surfaces. When glaze ice forms

over rime ice, the water film may be significantly affected by the roughness of the surface as would the ice layer.

- Finally, the refinement of the grid has more interest than reducing the truncation error itself. When combined with a multi-stepping approach refinement can be concentrated where accurate external flow conditions are required. Different refinement criteria could be implemented to improve different part of the icing calculation like catch or heat transfer. Further investigation need to be carried out in this direction.

Appendix A

The main algorithm

On the next page, the algorithm for the icing solver module MAGNUM is presented like in the ICECREMO2 Software Specification [31]. The main part of this work is implemented inside the CalcRHS routine which solves for the water film equation.

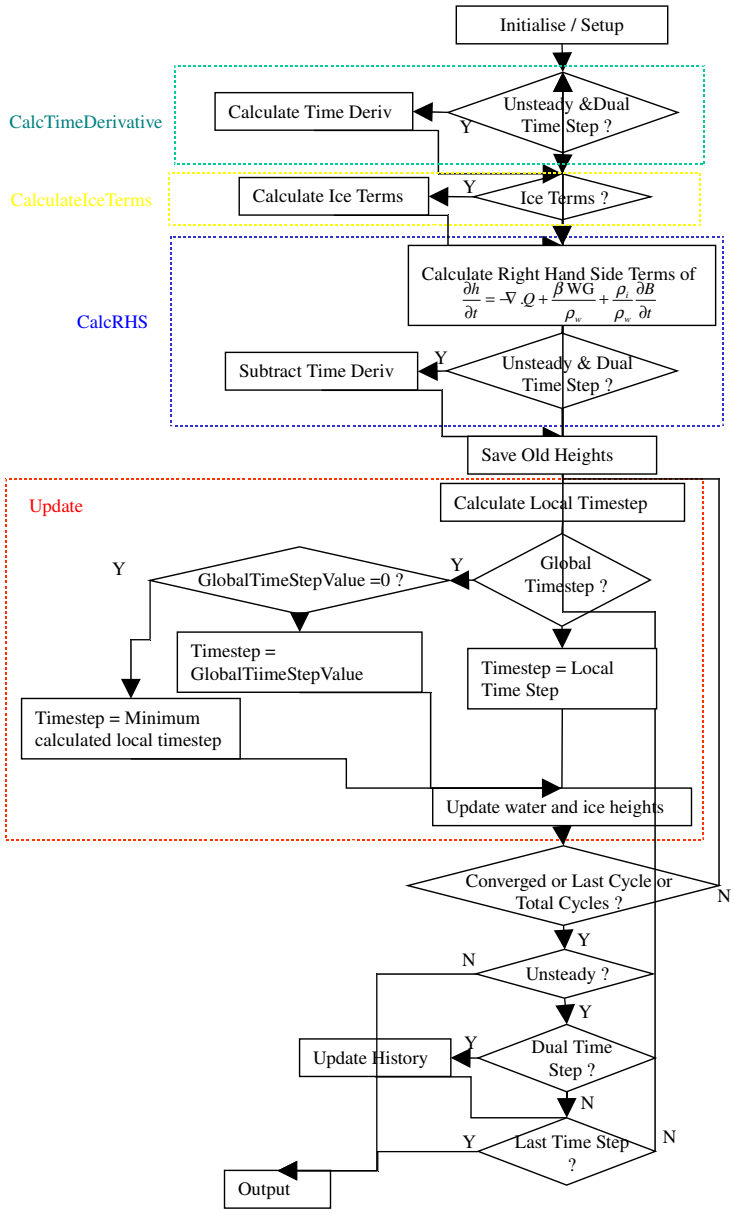

Figure A.1: MAGNUM, flowchart

Appendix B

The Multi-Step Algorithm

The multi-step is a complex procedure and all the details can be found in [20], but an overview of the main algorithm is shown in Figure B.1. The geometry is first define and meshed in a grid generation software (GAMBIT in this case). Then a flow solver (Fluent) is used to compute the external flow,i.e.: the air speed. Only then it can enter ICECREMO2 for the ice prediction.

The multi-step consists in dividing the exposure time in several step. After each step a restart file is created contening all the data necessary for the calculations. Then the geometry is updated so the new mesh will include the ice layer. The external flow in the following step will be updated.

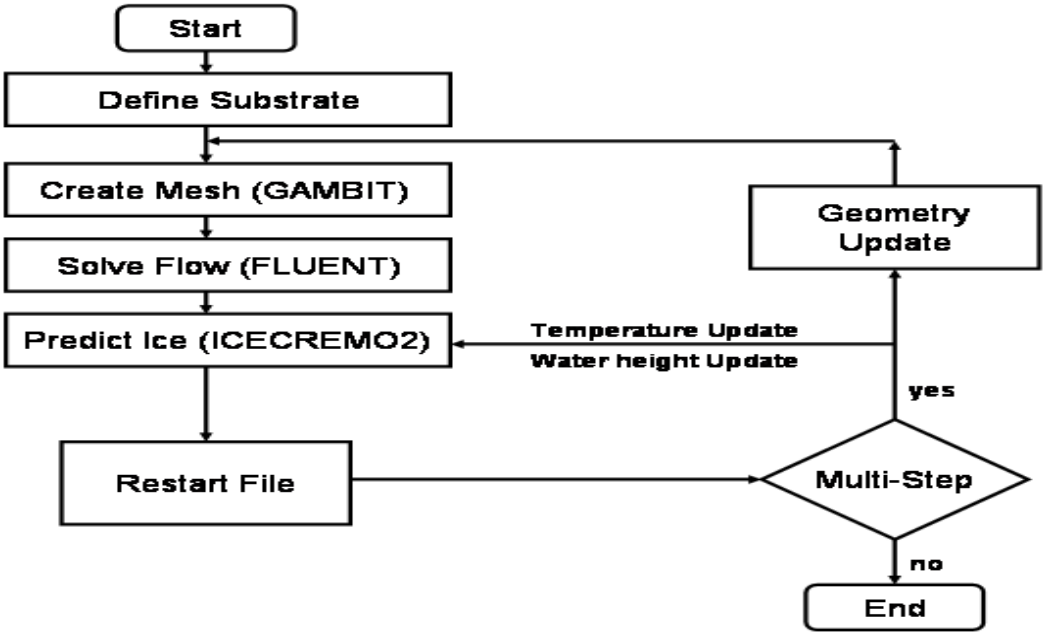

Figure B.1: The Multi-Step Algorithm

Appendix C

Note On TVD schemes

C.1 TVD scheme with source terms

The high resolution method used in this thesis and developped in Chapter 3 has been shown to be TVD for burger's equation. If surface tension is neglected, pressure and gravity, the equation governing the water flow is of this type. However for the full equation proving that the scheme is TVD is non-trivial. Generally for hyperbolic conservation law, in the homogenous case, i.e.: in absence of source (or right hand side), this is the case. However the presence of source terms in our equation like the impinging water $\frac{\beta WG}{\rho_w}$ and the ice growth rate $\frac{\partial b}{\partial t}$ demands to be very carefull. For the sake of clarity let's recall Equation 1.8:

$$\frac{\partial h}{\partial t} = -\nabla.Q + \frac{\beta WG}{\rho_w} - \frac{\rho_i}{\rho_w}\frac{\partial b}{\partial t} \tag{C.1}$$

The term representing the incoming water is constant with time and does not intervene in the monotonicity of the numerical scheme. However the ice growth is not and can be positive (ice growth) or negative (melting). In all the test cases taken in this thesis it represents a 'sink' term, i.e.: always positive the water mass is taken out and transfomed

into ice. But if De-icing is considered, the ice growth term becomes negative and thus a 'source' term. Depending of how fast the ice is melting and the water released in the system would be crucial for the stability of the numerical scheme. In practice when two phenomena are represented in an equation, it is common to take time steps which resolve the fastest scale. In a normal ice accretion case, this time step is based on the water film under CFL condition.

In the case of ice melting it is not clear how one should treat the additional water. In the litterature a 'general rule of thumb' suggest that the time step must be restricted so that the total energy released by the source term does not change by more than $10 - 20\%$ in any cell. In [49] Leveque identifies incorrect propagation speed when the relaxation time scale for the source term is not small enough. Still in [49] a splitting method is proposed to separate the different phenomena (in the case of reactive flow) and seems to perform well.

Such investigation is beyond the work of this thesis but it is very important to take this into account if one wanted to simulate de-icing. Currently in ICECREMO2 the de-icing capability is incomplete and the water coming from the melting is not released into the system, so there is no additional difficulties.

Bibliography

[1] J. Charpin. *Water Flow on Accreting Ice surfaces*. PhD thesis, AMAC, Cranfield University, 2002.

[2] T.G. Myers, J.P.F. Charpin, and C.P. Thompson. *Slowly accreting ice due to supercooled water impacting on a cold surface. Physics of fluids*, 14(1), January 2002.

[3] T.G. Myers and J.P.F. Charpin. *A Mathematical model for Atmospheric ice accretion and water flow on a cold surface. International Journal of Heat and Mass Transfer*, 47:5483–5500, 2004.

[4] T.G. Myers. *An extension of the Messinger model for aircraft icing*. AIAA, 39(2):211–218, 2001.

[5] Environment Canada's world Wide Web site. *Ice Storm 1998*. http://www.msc-smc.ec.gc.ca/media/icestorm98/index_e.cfm (Last access: 02/01/2009).

[6] NASA Glenn Research Center. *Icing branch at NASA Glenn Research Center*. http://icebox-esn.grc.nasa.gov (Last access: 02/01/2009).

[7] FENSAP-ICE. *Newmerical Technologies Int.* http://www.newmerical.com/public/eng/index.ph
(Last access: 01/01/2009).

[8] Bruce Landsberg. *Ice folklore*. From AOPA Pilot January 1995: www.aopa.org/asf/asfarticles/sp9501.html (Last access: 02/01/2009).

[9] Aircraft icing. *AOPA Air Safety Foundation*. report SA11-11/02.

[10] Kevin R. Petty and Carol D.J. Floyd. *A statistical review of aviation airframe icing accidents in the U.S.* . Technical report, National Transportation Safety Board, Last accessed:31/05/2007. http://ams.confex.com/ams/pdfpapers/81425.pdf.

[11] Steve Owen. *A Survey of Unstructured Mesh Generation Technology*. Technical report, Meshing Research Corner, Last accessed:06/04/2007. http://www.andrew.cmu.edu/user/sowen/survey/index.html.

[12] D.J. Mavriplis. *Unstructured Grid Techniques*. Annual Reviews of Fluid Mechanic, 29:473–514, 1997.

[13] Culbert B. Laney. *Computational Gas Dynamics*. Cambridge University Press, 1998

[14] W.B. Bendel and D.Paton. *A review on the effects of ice storm in the power industry*. Journal of Applied Meteorology. Volume 20, Issue 12 (December 1981).

[15] A.J. Press and N.P. Dart. *ICECREMO User Guide*. Technical report, 1982.

[16] K.M.Al-Khalil, Jr T.G.Keith, and K.J.De Witt. *Developement of an Anti-icing Run-back model* . AIAA 90-0759, 1990.

[17] T.P. Ratvasky and R.J. Ranaudo. *Icing Effects on Aircraft Stability and Control Determined from Flight Data* . AIAA 93-0398, 1993.

[18] P. Perkins and W. Rieke. *Aircraft Icing Problems -after 50 years*. AIAA 93-0392, 1993.

[19] Steve Ritter. *Aircraft Deicers*. Chemical and engineering news, January 2001, Volume 79, number 1.

[20] P. Verdin. An Automatic Multi-Stepping Approach for Aircraft Ice Prediction. PhD thesis, Cranfield University, sme, AMAC, 2008.

[21] H. Anderson. *Stability Effect of Heat and Mass Transfer on Thin Liquid Films*. PhD thesis, AMAC, Cranfield University, 2002.

[22] Jen-Ching Tsao. *A theoretical and numerical study of thin film and ice accretion dynamics on aircraft wing surfaces*. PhD thesis, Iowa State University, 1998.

[23] Federal aviation administration. *Electronic Aircraft Icing Hanbook (EAIHB).* http://www.fire.tc.faa.gov/aar421/eaihbpg.html.

[24] T. Hedde and D. Guffond. *Improvement of the ONERA 3D icong code, comparison with 3D experimental shapes.* AIAA, (93-0169), 1993.

[25] H. Beaugendre, F. Morency, and W.G. Habashi. *FENSAP-ICE 's three dimensional in flight ice accretion module: ICE3D.* Journal of Aircraft, 128(2):378–387, 2006.

[26] H. Beaugendre, F. Morency, and W.G. Habashi. *Development of a second generation in-flight icing simulation code.* Journal of Fluid Engineering, 40(2), March-april 2003.

[27] W.B.Wright, R.W.Gent, and D.Guffond. *Prediction of Airfoil Accretion.* Technical report, DRA/ONERA/NASA collaboration on icing research, part II, 1993.

[28] RTO-TR-038. *Ice Accretion Simulation Evaluation Test.* Technical report, Report of the Applied Vehicle Technology Panel, 2001.

[29] P.H. Gaskell, P.K. Jimack, M. Sellier, and H.M. Thompson. *Efficient and Accurate Time Adaptive Multigrid Simulations of Droplet Spreading.* School of Mechanical Engineering , University of Leeds, 2002.

[30] Volker Elling. *Numerical simulation of gas flow in moving domain.* Master's thesis, Fakultat fur Mathematik der Reinisch-westfalischen Technischen Hochschule Aachen, november 2000.

[31] A.J. Press and L. Pearson. *ICECREMO 2 Software Specification.* BAE SYSTEMS JS15296, August 2004.

[32] B.D. Matheis and A.P. Rothmayer. *Numerical simulation of thin air driven films.* AIAA, (2002-0525), 2002. 40th Aerospace Sciences Meeting and Exhibit, 14-17 January 2002, Reno Nevada.

[33] A.P. Rothmayer and J.A. Krakos. *Residual droplet impacts and thin film dynamics.* AIAA, (2004-0057), 2004. 42nd Aerospace Sciences Meeting and Exhibit, 14-17 January 2002, Reno Nevada.

[34] C.P. Thompson. *Modelling methodology: Discretisation, Solution algorithms, error control and adaptivity.* Deliverable report 3.4.1, draft version 1.0, May 2004.

[35] Euletario F. Toro. *Shock-Capturing methods for Free-Surface Shallow Flows.* John Willey & Sons ltd., 2001.

[36] Euletario F. Toro. *Riemann Solver and Numerical Methods for Fluids Dynamics, A practical introduction.* Springer-Verlag. First Edition, January 15, 1997.

[37] P.K. Sweby. *High resolution schemes using flux limiters for hyperbolic conservation laws. SIAM, J.Numer.Anal.*, 21(5), October 1984.

[38] A. Jameson. *Time dependent calculations using multigrid, with applications to unsteady flows past airfoils and wings. AIAA 91-1596*, 1596, 1991.

[39] John M.Hsu and Antony Jameson. *An implicit-explicit hybrid scheme for calculating complex unsteady flows. AIAA*, 0714, 2002.

[40] S.Osher and S.Chakravarthy. High resolution schemes and the entropy condition. *SIAM, Journal On Numerical Analysis*, 21:955–984, 1984.

[41] Y. Soufflet and C.P. Thompson. Stability and convergence on the stagnation line. Technical Report, May 2003.

[42] P.tran, M.T.Brahimi, F.Tezok, and I.Paraschivoiu. *Numerical Simulation of Ice Accretion on Multiple Element Configuration.* AIAA 96-0869, 1996.

[43] M. Fregeau, F. Saeed, and I.Paraschivoiu. *Surface heat transfer study for ice accretion and anti-icing prediction in three dimension.* AIAA 2004-63, 2004.

[44] AMAC. *Finite Difference Analysis.* AMAC Lecture notes, 2001.

[45] E. Sousa. *The controversial stability analysis.* Applied Mathematics and Computations, 145:777–794, 2003.

[46] A. Kurganov and E. Tadmor. *New High-Resolution Central schemes for non-linear conservation laws and convection-diffusion equations.* Journal of computational Physics, 160:241–282, 2000.

[47] H.Q. Yang and A.J. Przekwas. *A comparative study of advanced shock-capturing schemes applied to Burger's equation.* Journal of Computational Physics, 102((1)):139–159, 1992.

[48] R.J. Leveque. *Numerical Methods for Conservation Laws.* BirkHauser, 1992.

[49] R.J. Leveque and H.C. Yee *A study of numerical methods for hyperbolic conservation laws with stiff source terms*. Journal of Computational Physics, Volume 86 (187-210), 1990

[50] R.J. Leveque. *Finite Volume Methods for hyperbolic Problems*. Cambridge University Press, 2002.

[51] A. Harten. *On a class of high resolution total variation stable finite difference schemes*. SIAM J. Numer. Anal., 21:1–23, 1984.

[52] A. Harten. *The artificial compression method for computation of shocks and contact discontinuities. III. Self-adjusting hybrid schemes.* Math. Comp., 32(142:363–389, 1978.

[53] Ami Harten and Stanley Osher. Uniformly high-order accurate nonoscillatory schemes. SIAM J. Numer. Anal., 24(2):279–309, 1987.

[54] Ami Harten, Bjorn Engquist, Stanley Osher, and Sukumar R. Chakravarthy. Uniformly high order accurate essentially non-oscillatory schemes, 111. J. Comput. Phys., 71(2):231–303, 1987.

[55] Ami Harten. High resolution schemes for hyperbolic conservation laws. J. Comput. Phys., 135(2):260–278, 1997.

[56] Bram van Leer. *Towards the ultimate conservative difference scheme. II. Monotonicity and conservation combined in a second order scheme.* J. Comput. Phys., 14:361–374, 1974.

[57] Bram van Leer. *Towards the ultimate conservative difference scheme. V. A second-order sequel to Godunov's method*. J. Comput. Phys., 32:101–136, 1979.

[58] J. P. Boris and D. L. Book. *Flux-Corrected Transport, I. SHASTA, A Fluid Transport Code that Works*. J. Comp. Phys., 11, 1973.

[59] P.R. Woodward P. Collela. *The piecewise parabolic method (PPM) for gas-dynamical simulations*. J. Comput. Phys., 54:174–201, 1984.

[60] P.R. Woodward and P. Collela. *The Numerical Simulation of Two–Dimensional Flow with Strong Shocks.* J. Comput. Phys., 54:115–173, 1984.

[61] P.L. Roe. *Some contribution to the modelling of discontinuous flows.* Lectures in Applied Mathematics 22 (1985) 163-193.

[62] Phil Roe. *A survey of upwind differencing techniques.* International Conference on Numerical Methods in Fluid Dynamics, 11th, Williamsburg, VA, June 27 July 1, 1988, Proceedings ($A89 - 4535119 - 34$). Berlin and New York, Springer-Verlag, 1989, p. $69 - 78$.

[63] Stephen F. Davis. *A simplified TVD finite difference scheme via artificial viscosity.* SIAM J. Sci. Stat. Comput., 8(1), 1987.

[64] F. Davis. *TVD finite difference schemes and artificial viscosity.* Technical Report 84-20, Icase report, 1984.

[65] T.G. Myers. *Thin films with high surface tension.* SIAM Review, 40, 1998.

[66] E. Momoniat, T.G. Myers, and S. Abelman. *New solution for surface tension driven spreading of a thin films* . International Journal of Non-Linear Mechanics, 40:523–529, 2005.

[67] N. Silvi and E.B. Dussan V. *On the rewetting of an inclined solid surface by a liquid.* The Physics of Fluids, Letters, 28, 1985.

[68] E.B. Dussan V. *On the spreading of liquids on solid surfaces: Static and dynamic contact line.* Annual Review of Fluid Mechanics, 11, 1979.

[69] H.E. Huppert. *Flow and instability of a viscous current down a slope.* Nature (London), 300, 1982.

[70] Jens Eggers. *Nonlinear dynamics and breakup of free surface flow.* Review of Modern Physics, 69, 1997.

[71] B.A. Wagner and A. Munsch. *Numerical and asymptotic results on the linear stability of a thin film flows down a slope of small inclinination.* Technical report, Fakultat fur Mathematik der Technischen Universitat Munchen. Report TUM M9705 (97).

[72] Po jen Cheng, Cha'o-Kuang Chen, and Hsin-Yi Lai. *Nonlinear stability analysis of thin viscoelastic film flow traveling down along a vertical cylinder.* Nonlinear Dynamics, 24:305–332, 2001.

[73] P.G. De Gennes. *Wetting: Statistics and Dynamics.* Review of Modern Physics, 57:828–861, 1985.

[74] A. Oron, S. H. Davis, and S.G. Bankoff. *Long-scale evolution of thin liquid films.* Review of Modern Physics, 69:931–980, 1997.

[75] B.D. Edmonstone, O.K. Matar, and R.V. Craster. *Coating of an inclined plane in the presence of insoluble surfactant.* Journal of Colloid and Interface Science, 287:261–272, 2005.

[76] L.W. Schwartz and R. Valery Roy. *Theoretical and numerical results for spin coating of viscous liquids.* Physics of Fluids, 16:569–584, 2004.

[77] L.W. Schwartz. *Viscous flow down an inclined plate: Instability and finger formation.* Physics of Fluids A, 1, 1989.

[78] M. Villegas-Diaz, H. Power, and D.S. Riley. *Analytical and numerical studies of stability of thin film rimming flow subject to surface shear.* Journal of Fluid Mechanics, 541:317–344, 2005.

[79] P.G. Lopez, S.G. Bankoff, and M.J. Miksis. *Non-isothermal spreading of a thin liquid film on an inclined plate.* Journal of Fluid Mechanics, 324:261–286, 1996.

[80] J.R. King. *Two Generalisations of the Thin film Equation.* Mathematical and Computer modelling, 34:737–756, 2001.

[81] J.A. Diez and L. Kondic. *Contact lines instabilities of thin liquid films.* Physical Review Letter, 86:632–635, 2001.

[82] J.A. Diez, L. Kondic, and A.L. Bertozzi. *Global models for moving contact lines.* Physical Review E, 63, 2001.

[83] J.A. Diez and L. Kondic. *Computing Thee-dimensional thin film flows including contact lines.* Journal of Computational Physics, 183:274–306, 2002.

[84] A.L. Bertozzi, A. Munsch, and M. Shearer. *Undercompressive shocks in thin film flows.* Physica D, 134:431–464, 1999.

[85] L. Kondic and J.A. Diez. *On nontrivial traveling waves in thin film flows including contact lines.* Physica D, 209:135–144, 2005.

[86] M. Hayes and S.B.G. O'Brien. *A model for gravity driven flow of a thin liquid-solid solution with evaporation effect.* Zeitschrift fur Angewandte Mathematik und Physic, ZAMP, 56:852–873, 2005.

[87] Uwe Thiele and E. Knobloch. *Thin liquid film on a slightly inclined heated plate.* Physica D, 190:213–248, 2004.

[88] H.C. Yee. *Upwind and Symmetric Shock-Capturing Schemes.* Technical Memorandum TM-89464, NASA, 1987.

[89] H. C. Yee, R. F. Warming, and Ami Harten. *On a class of tvd schemes for gas dynamic calculations.* In *Proc. of the sixth int'l. symposium on Computing methods in applied sciences and engineering, VI*, pages 491–492, Amsterdam, The Netherlands, The Netherlands, 1985. North-Holland Publishing Co.

[90] J. Glimm, J. Grove, X. Li, and N. Zhao. *Simple front tracking.* Contemporary Mathematics 1999.

[91] James Glimm, John W. Grove, Xiao Lin Li, Keh ming Shyue, Yanni Zeng, and Qiang Zhang. *Three-dimensional front tracking.* SIAM Journal on Scientific Computing, 19(3):703–727, 1998.

[92] J.J. Quirk. *A contribution to the great Riemann solver debate.* Int. J. Numer. Meth. Fluids, 18:555–574, 1994.

[93] Bram van Leer. *On the relation between the upwind-differencing schemes of Godunov, Engquist-Osher and Roe.* 5(1):1–20, March 1984.

[94] P.L. Roe. Generalized formulation of tvd lax–wendroff schemes. Technical report, Hampton, U.S.A., 1984.

[95] R. Courant, K. Friedrichs and H. Lewy Über die partiellen Differenzengleichungen der mathematischen Physik Mathematische Annalen, vol. 100, no. 1, pages 3274, 1928.

[96] R. Courant, K. Friedrichs and H. Lewy. "On the partial difference equations of mathematical physics", IBM Journal, March 1967, pp. 215-234, English translation of the 1928 German original

[97] R. Courant and K.O. Friedrichs *Supersonic Flow and Shock Waves.* Interscience Publishers, 1948.